2013-07-26

Properties of Holmium Implanted Gold Films and Yttrium Silicide to use as Absorbers in Microcalorimeters for a Holmium Neutrino Mass Experiment

Krishna P. Prasai
University of Miami, kprasai55@gmail.com

Recommended Citation

Prasai, Krishna P., "Properties of Holmium Implanted Gold Films and Yttrium Silicide to use as Absorbers in Microcalorimeters for a Holmium Neutrino Mass Experiment" (2013). *Open Access Dissertations*. 1060.
https://scholarlyrepository.miami.edu/oa_dissertations/1060

UNIVERSITY OF MIAMI

PROPERTIES OF HOLMIUM IMPLANTED GOLD FILMS AND YTTRIUM SILICIDE TO USE AS ABSORBERS IN MICROCALORIMETERS FOR A HOLMIUM NEUTRINO MASS EXPERIMENT

By

Krishna P. Prasai

A DISSERTATION

Submitted to the Faculty
of the University of Miami
in partial fulfillment of the requirements for
the degree of Doctor of Philosophy

Coral Gables, Florida

August 2013

UNIVERSITY OF MIAMI

A dissertation submitted in partial fulfillment of
the requirements for the degree of
Doctor of Philosophy

PROPERTIES OF HOLMIUM IMPLANTED GOLD FILMS AND YTTTRIUM SILICIDE TO USE AS ABSORBERS IN MICROCALORIMETERS FOR A HOLMIUM NEUTRINO MASS EXPERIMENT

Krishna P. Prasai

Approved:

Massimiliano Galeazzi, Ph.D. Professor of Physics	M. Brian Blake, Ph.D. Dean of the Graduate School
Joshua Cohn, Ph.D. Professor of Physics	Fulin Zuo, Ph.D. Professor of Physics
Maria Ribeiro Gomes, Ph.D. Professor of Physics University of Lisbon & CFNUL, Portugal	

PRASAI, KRISHNA P. (Ph.D., Physics)
Properties of Holmium Implanted Gold Films and Yttrium Silicide to Use as Absorbers in Microcalorimeters For a Holmium Neutrino Mass Experiment (August 2013)

Abstract of a dissertation at the University of Miami.

Dissertation supervised by Professor Massimiliano Galeazzi.
No. of pages in text. (132)

In recent years, there has been huge improvement in microcalorimetric technology and its applications. Today's cryogenic microcalorimeter technology can be used in a large scale experiment with excellent energy and time resolutions. Transition Edge Sensor (TES) microcalorimeters are being developed as imaging spectrometers for a wide range of applications including neutrino mass measurement. We are developing a source (^{163}Ho) embedded TES microcalorimeter for neutrino mass measurement. Energy resolution, rise time of events, decay time, and read-out electronics must be considered carefully in designing a microcalorimeter for the application of neutrino mass experiments. Our research is particularly focused on the investigation of the properties of the ^{163}Ho imbedded metallic absorber for the application of the Ho-neutrino mass experiment.

In a microcalorimetric neutrino mass experiment using the radioactive decay of ^{163}Ho, the radioactive material must be fully embedded in the microcalorimeter absorber. One option that is being investigated is to implant the radioactive isotope into a gold absorber, as gold is successfully used in other applications. However, knowing the thermal properties at the working temperature of microcalorimeters is critical for choosing the absorber material and for optimizing the detector performance. In particular, it is paramount to understand if implanting the radioactive material in gold changes its heat capacity. We used a bolometric technique to measure the heat capacity of gold films, implanted with various concentrations of holmium and erbium (a byproduct of the ^{163}Ho fabrication), in the temperature range 70 mK to 300 mK. Our results show that the specific heat capacity of the gold films is not affected by the implant, making this a viable option for a future microcalorimeter holmium experiment. Furthermore, most chemical processes to extract the Ho-163 isotope and insert it into a detector absorber involve yttrium based compounds. Rather than using yttrium as an intermediate step in the isotope extraction procedure, the metal yttrium silicide (Y_5Si_3) is a possible candidate to use directly as an absorber material. We measured the heat capacity of small Yttrium Silicide (Y5Si3) sample in the temperature range 90mK—300mK, to verify if it could be used as an absorber in the fabrication of microcalorimeters. We also measured its resistivity from room temperature to 90 mK. Our result indicated that the heat capacity of Y_5Si_3 is larger than gold (often used as absorber material) by more than a factor of five in the working temperature range of TES microcalorimeter.

To my friends and family

Acknowledgments

My long tenure as a graduate student at the University of Miami has been widely enriched by the help, advice, guidance, and cooperation of many wonderful people. Everything I learned in the last six years is entirely due to those around me. I feel honored and fortunate to have this opportunity. I would like to thank my friends, family members, and co-workers from the bottom of my heart.

I would like to express the deepest appreciation to my supervisor and committee chair, Professor Massimiliano Galeazzi. It would not have been possible to complete this doctoral thesis without his guidance and persistent help. I have profoundly benefitted from his enthusiasm, generosity, excitement, advice, and supervision. His expertise in low temperature physics, detector design, particle physics, superconductivity, and astrophysics improved my research skills and prepared me for future challenges. I deeply thank him for the unique freedom he offered to explore my intellectual curiosity in our experimental research.

I wish to express my sincere thanks to my committee members Professor J. Cohn and Professor F. Zuo for their support, suggestions, and training. I am very grateful to Professor Cohn for allowing me to use his research facilities. I am also extremely thankful for the valuable advice and support of my department chair, Professor K. Voss. I would like to acknowledge the academic, technical, and financial support of our Department.

I would like to thank the Portuguese group, Center for Nuclear Physics and Unit of Physics and Accelerators, University of Lisbon, Portugal, for providing us all the

implanted gold film samples. I am especially thankful to Dr. Maria Ribeiro Gomes, the Principal investigator for the work financed by Portuguese National funds via-Fundação para a Ciência e a Tecnologia in the framework of PTDC/FIS/116719/2010, for her support, suggestions and comments. I am proud to have Dr. Gomes as my external committee member. I am also thankful for the Genova group, University of Genova & INFN for providing us an yttrium silicide (Y_3SI_5) sample. I am grateful to Professor F. Gatti for his comments and suggestions.

TABLE OF CONTENTS

Page

List of Figures

List of Tables

Chapter 1

Introduction to Neutrinos and Their Mass Measurements

1.1 Massive Neutrino

Despite being very light and having no charge, neutrinos play a vital role in the past and future development of our universe. Experimental observations have exposed that neutrinos can oscillate from one flavor to another (for example an electron neutrino can convert into a muon neutrino and vice versa). These flavor oscillations have provided evidences that neutrinos have mass and that physics beyond the Standard Model (SM) of particle physics is possible. Neutrino oscillation experiments are sensitive to the differences in squared mass, but they remain blind to the absolute mass scale and the possible Majorana phases which distinguish whether a neutrino is Dirac or Majorana particle. A Dirac neutrino has a distinct antineutrino, while a Majorana neutrino is the antineutrino of its own. Non-oscillation experiments— particularly cosmological observations, searches for neutrinoless double beta decay, and high precision measurements of single beta decay — are the current strategy for the experimental determination of neutrino mass. Cosmological research is sensitive to the sum of the neutrino masses, while neutrinoless double beta decay has been the only known technique to determine whether neutrinos are Dirac or Majorana particles. To date the most sensitive upper limit of electron neutrino mass has been obtained by direct observation of decay kinematics in single β-decay process. Currently two independent methods, spectrometric and calorimetric measurement of β-spectrum, have been adopted for the electron neutrino mass measurement from the end point study of β-decay.

A brief overview of the history of neutrino physics, discussion of neutrino oscillations, and short discussions of each of the three types of the non-oscillation neutrino mass experiments will be presented in this chapter.

1.2 Neutrino Physics: Past and Present

In 1930, Wolfgang Pauli postulated the existence of a new particle to account for the apparent mass non-conservation in β-decay. This particle, emitted in β-decay along with the electron, causes the latter to have a continuous energy spectrum. Enrico Fermi, in 1934, called it a neutrino (little neutral one) within the formulation of his theory for beta decay [1]. Due to their extremely elusive properties (close to zero mass and no charge), it was a challenging task for scientists to design experiments to detect them. In the mid-1950s, the existence of an electron neutrino was experimentally confirmed for the first time by Fred Reines and Clyde Cowan [2, 3]. The Cowan-Reines neutrino experiment was based on the observation of the inverse beta decay reaction produced by antineutrino interactions. In particular, when a proton interacts with an antineutrino producing a neutron and a positron $,\bar{\nu} + p^{+} \rightarrow n + e^{+}$, the outgoing positron quickly reacts with an electron releasing two detectable gamma rays. The next advancement occurred in 1962, when muon neutrinos were discovered at Brookhaven National Lab via observations of muonic decay [4]. The existence of the tau neutrino, the last lepton predicted by the Standard Model, was confirmed in 2000 by the DONUT (Directed Observation of the NU Tau) experiment at Fermi lab [5]. Each of these three experimentally verified neutrinos coupled with a charged lepton. More recently certain anomalies observed in neutrino experiments, such as those revealed by LSND results [6], imply that the existence of additional neutrino flavors that are not associated with charged leptons is possible. They are called sterile neutrinos.

Solar neutrinos are the most abundant of neutrino fluxes passing through the earth and were first measured in 1960's by the Homestake solar neutrino experiment. This experiment used the radiochemical technique based on the inverse beta decay reaction, $\nu_e + {}^{37}Cl \rightarrow {}^{37}Ar + e^-$, where a neutrino interacts with a ${}^{37}Cl$ atom and transforms it into a radioactive ${}^{37}Ar$ atom that can be detected due to its radioactivity. Data from the Homestake detector showed that the measured solar neutrino flux was about one-third the number predicted by the standard solar model, giving rise to the `Solar Neutrino Problem'. Many other experiments, such as GALLEX [7], SAGE [8], SNO [9], and Super-Kamiokande [10], also consistently measured similar number of neutrinos. The solution of the problem came from the discovery of neutrino flavor oscillations. The Homestake experiment was counting about one third of the actual number of solar neutrinos because it was only sensitive to electron neutrinos but not muon and tau neutrinos. Apart from the solar neutrinos, we now know about the neutrinos from the cosmic ray collisions with the atmosphere, supernovas, and lab based nuclear reactions. All of these sources are currently being studied in the effort to learn more about the nature of neutrinos. In the last few decades, observations from solar experiments [11, 12], atmospheric experiments [13, 14], reactors [15, 16], and accelerators [17, 18] showed that a neutrino emitted as one flavor can be detected as another, i.e. neutrino flavors do oscillate.

According to the Standard Model (SM) of electroweak interaction, neutrinos are the left-handed massless partners of charged leptons. However, recent discoveries have proven that neutrinos are massive particles, implying that the SM is incomplete and the existence of new physics beyond the SM is mandatory. Many theories have been developed to investigate the basis of neutrino mass and mixing. Grand Unified Theories (GUTs), an effort to unify the strong and electroweak interactions, have provided a theoretical framework for neutrino mass. The seesaw mechanism that elucidates the smallness of neutrino mass is often included in GUTs. The possible Majorana nature of neutrinos and their absolute mass scale are still open questions which are puzzling many scientists around the world. Based on our current understanding of Big-Bang Nucleosynthesis and the cosmic microwave background (CMB), neutrinos must have had a significant role in the history of the early universe.

Precise knowledge of mass scale, pattern, and nature of neutrinos is crucial for improving our understanding of the basic physics behind the theory of fundamental interactions as well as for testing the validity of the existing theory. Many scientists and institutions are involved in neutrino research today. Determination of neutrino mass and the establishment of a sound theoretical framework to incorporate flavors, oscillations, and mixing are necessary to understand the current state of the universe and to answer many other unanswered questions. Neutrinos seem to answer many questions.

1.3 Neutrino Oscillations

Neutrino flavor eigenstates $\left(|\nu_e\rangle, |\nu_\mu\rangle, |\nu_\tau\rangle\right)$ and mass eigenstates $(|\nu_1\rangle, |\nu_2\rangle, |\nu_3\rangle)$ are not necessarily identical. This leads to a phenomenon of neutrino oscillations. Neutrino oscillation is a purely kinematical phenomenon and it occurs in matter and in vacuum. The theory of neutrino oscillation is essentially the quantum mechanics of mixed states. Details of the neutrino oscillation theory can be found in references [19] & [27]. Here I summarize their results. The flavor eigenstates of the weak interaction are described by superposition of the mass eigenstates as

$$|\nu_\alpha\rangle = \sum_{i=1,2,3} U_{\alpha i}^{*}|\nu_i\rangle, \qquad 1.1$$

Similar expression for the mass eigenstates is

$$|\nu_i\rangle = \sum_{\alpha=e,\tau,\mu} U_{i\alpha}^{+}|\nu_i\rangle \;=\; \sum_{\alpha} U_{\alpha i}^{*}|\nu_i\rangle. \qquad 1.2$$

where U is the unitary mixing matrix, known as Pontecorvo-Miki-Nakagava-Sakata (PMNS) matrix, in the following form

$$\begin{pmatrix} c_{12} & s_{12} & 0 \\ -s_{12} & c_{12} & 0 \\ 0 & 0 & 1 \end{pmatrix}\begin{pmatrix} 1 & 0 & 0 \\ 0 & c_{23} & s_{23} \\ 0 & -s_{23} & c_{23} \end{pmatrix}\begin{pmatrix} c_{13} & 0 & s_{13}e^{-\delta} \\ 0 & 1 & 0 \\ -s_{13}e^{-\delta} & 0 & c_{13} \end{pmatrix}\begin{pmatrix} e^{\frac{i\alpha_1}{2}} & 0 & 0 \\ 0 & e^{\frac{i\alpha_2}{2}} & 0 \\ 0 & 0 & 1 \end{pmatrix},$$

where $c_{ij} = \cos\theta_{ij}, s_{ij} = \sin\theta_{ij}, \theta_{ij}$ are mixing angles, δ is the complex charge parity (CP) violating phase, and α_1, α_2 are the additional phases, if a neutrino is the Majorana particle (an antiparticle of its own). Majorana phases (α_1, α_2), even if present, appear only on the neutrinoless double beta decay and neutrino oscillations are independent of these phases. Therefore, the standard parameterization of the mixing matrix is

$$U_{\alpha i} = \begin{pmatrix} c_{12}c_{13} & s_{12}c_{13} & s_{13}e^{-i\delta} \\ -s_{12}c_{23} - c_{12}s_{23}s_{13}e^{i\delta} & c_{12}c_{23} - s_{12}s_{23}s_{13}e^{i\delta} & s_{23}c_{13} \\ s_{12}s_{23} - c_{12}c_{23}s_{13}e^{i\delta} & -c_{12}s_{23} - s_{12}c_{23}s_{13}e^{i\delta} & c_{23}c_{13} \end{pmatrix}. \qquad 1.3$$

The mixing angles together represent a three dimensional rotation of the mass basis to the flavor basis and the complex phase δ acts as a distinction between the neutrino mixing and antineutrino mixing. In total, there are nine unknown quantities, which include three masses, three mixing angles and three phases.

Applying Schrodinger equation with $\hbar = c = 1$, the time evolution of a mass eigenstates can be expressed as

$$|\, \nu_i(t)\rangle \;=\; e^{-iE_it}\, |\nu_i\rangle. \qquad 1.4$$

Using relativistic energy momentum relation we have

$$E_i = \sqrt{m_i^2 + p_i^2} \approx E + \frac{m_i^2}{2E}\; for\, p \ll m_i \; and\; E{\sim}p. \qquad 1.5$$

Assuming $m_i \neq m_j$ for $i \neq j$, the different eigenstates are propagating with different phase factors. The neutrino oscillation is the result of the relative phase difference of the propagation of these mass eigenstates. After time *t*, a neutrino of definite flavor state becomes

$$|\nu(t)\rangle = \sum_{i,\beta} U_{\alpha i}\, e^{-iE_it}\, |\nu_i\rangle = \sum_i U_{\alpha i}\, U_{\beta i}^* e^{-iE_it}\, |\nu_\beta\rangle. \qquad 1.6$$

Clearly, the flavor contents in the initial and final state are different. If a neutrino is detected after travelling time *t*, the probability that a particular neutrino converts to another flavor is

$$P\left(\nu_\alpha \to \nu_\beta\right) = \left|\langle \nu_\beta | \mathrm{v(t)}\rangle\right|^2 = \left|\sum_i U_{\alpha i}\, U_{\beta i}^* e^{-iE_it}\right|^2$$

$$= \sum_i \left|U_{\alpha i} U_{\beta i}^*\right|^2 + 2\Re \sum_{i>j} U_{\alpha i}\, U_{\alpha j}^* U_{\beta i}^* U_{\beta j} e^{-i(E_i - E_j)t}. \qquad 1.7$$

For ultra-relativistic neutrinos, the distance between the source and detector is $L = ct = t$ for c=1 and phase difference term is given by

$$(E_i - E_j)t \approx \frac{m_i^2 - m_j^2}{2}\frac{L}{E} = \frac{\Delta m_{ij}^2}{2}\frac{L}{E}.$$

The first term in the right hand side of the Equation (1.7) is an average transition probability, while the second term gives the time or spatial dependence of neutrino mass oscillation. For neutrino oscillation, at least one of the neutrino mass eigenstates must be nonzero and non-diagonal terms in U must exist.

If $\Delta m_{ij}^2 = m_i^2 - m_j^2$ is in eV^2, L is in km, and E is in GeV, then Equation (1.7) can be expressed as [20]

$$P\left(\nu_\alpha \to \nu_\beta\right) = \delta_{\alpha\beta} - 4\sum_{i>j} Real\left(U_{\alpha i}^* U_{\beta i} U_{\alpha j} U_{\beta j}^*\right) sin^2\left[1.27\Delta m_{ij}^2\left(\frac{L}{E}\right)\right]$$

$$+2\sum_{i>j} Im\left(U_{\alpha i}^* U_{\beta i} U_{\alpha j} U_{\beta j}^*\right) sin\left[2.54\Delta m_{ij}^2\left(\frac{L}{E}\right)\right] \qquad 1.8$$

The transition probability $P\left(\nu_\alpha \to \nu_\alpha\right)$ is determined by four mixing parameters $\theta_{12}, \theta_{23}, \theta_{13}\ and\ \delta$, and two independent mass squared differences $\Delta m_{21}^2$and Δm_{32}^2.

If oscillation takes place between only two flavor states, then the mixing matrix is simplified as

$$U = \begin{pmatrix} cos\theta & \sin\theta \\ -sin\theta & cos\theta \end{pmatrix}. \qquad 1.9$$

which yields

$$P\left(\nu_\alpha \to \nu_\alpha\right) = sin^2 2\theta\ sin^2\left[1.27\Delta m^2\left(\frac{L}{E}\right)\right]. \qquad 1.10$$

The probability of finding the particle in its initial flavor is

$$P\left(\nu_\alpha \to \nu_\alpha\right) = 1 - \sum_{\alpha\neq\beta} P\left(\nu_\alpha \to \nu_\beta\right). \qquad 1.11$$

Since the neutrino oscillations are only sensitive to differences in mass squared Δm_{ij}^2, the absolute neutrino mass scale is not assessable in oscillation experiments.

(Table 1.1) *Summary of current neutrino masses and mixing parameters* [21]

$$\Delta m_{21}^2 = (7.50 \pm 0.20) \times 10^{-5} eV^2$$

$$\left|\Delta m_{32}^2\right| = (2.32 \pm_{0.08}^{0.20}) \times 10^{-3}\ eV^2$$

$$Sin^2(2\theta_{12}) = 0.857 \pm 0.024$$

$$Sin^2(2\theta_{23}) > 0.95$$

$$Sin^2(2\theta_{13}) = 0.098 \pm 0.013$$

Since the solar neutrino oscillation experiments have allowed the measurement of θ_{12} and Δm_{21}^2, these parameters are referred to as solar parameters and are often denoted as $\theta_{12} = \theta_S$ and $\Delta m_{21}^2 = \Delta m_S^2$. For similar reasons, θ_{23} and Δm_{32}^2 are called atmospheric parameters and are denoted as $\theta_{23} = \theta_A$ and $\Delta m_{32}^2 = \Delta m_A^2$. Many different groups have performed global fits including all the available data and provided the values of these parameters. Recently published results from global fits to solar (SuperKamiokande, SNO and GALLEX /GNO), atmospheric (SuperKamiokande and MACRO), reactors (KamLAND, and CHOOZ0), and accelerators (K2K and MINOS) experiments is presented in the Table (1.1).

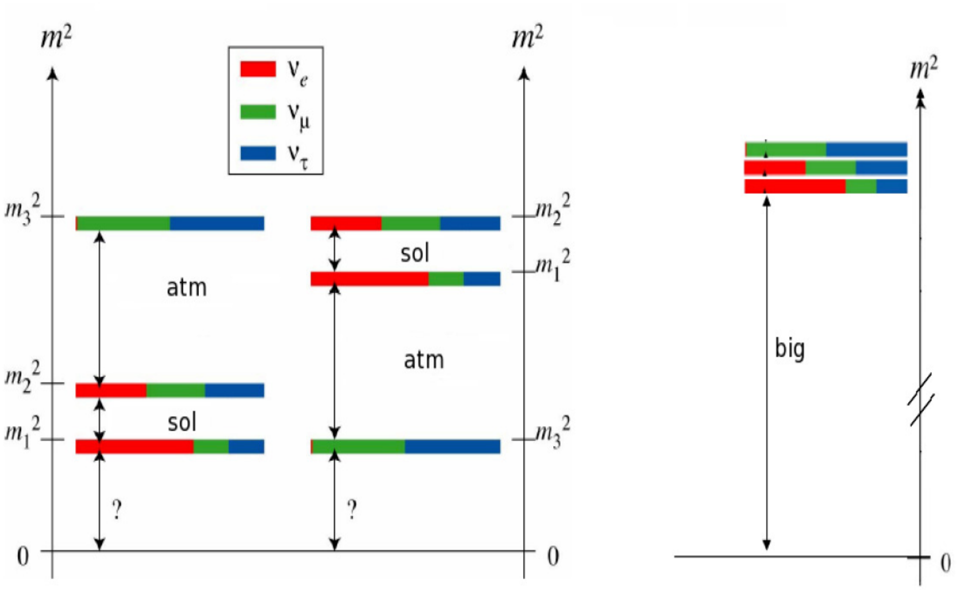

(FIG.1.1) *Possible scenarios for normal, inverted, and degenerate neutrino mass patterns [19]*

The sign of Δm_{32}^2 is yet to be determined. Therefore, two types of neutrino mass patterns are possible depending on the actual signs of Δm_{32}^2. Assuming that $\Delta m_{21}^2 \ll \Delta m_{32}^2$, if $\Delta m_{32}^2 > 0$, the corresponding mass pattern, $m_1 < m_2 \ll m_3$, is known as a normal hierarchy, while if $\Delta m_{32}^2 < 0$, the corresponding mass spectrum, $m_3 \ll m_2 < m_1$, is called inverted hierarchy. A third possibility, where $m_1 \sim m_2 \sim m_3$, is called degenerate neutrinos. Figure (1.1) shows the three possible configurations of neutrino mass patterns, where colors represent flavor densities in mass patterns.

Oscillation experiments are not only insensitive to the absolute mass scale but also to the two possible Majorana phases (α_1, α_2). Therefore, many other non-oscillation experiments have been considered as powerful tools to assess the neutrino mass pattern and possible Majorana nature. Non-oscillation experiments can be categorized into three groups: Cosmological observations, double beta decay and single beta decay.

1.4 Cosmological Searches for Neutrino Mass

Massive neutrinos constitute an (unknown) fraction of dark matter and hence contribute to the total energy density of the Universe. Neutrinos can play a significant role in the evolution of the Universe, leaving a distinctive imprint on various cosmological observables. In particular, light neutrinos do not cluster on small scale and the effect on the cosmology is to suppress the gravitational growth of density fluctuations [23]. There are many different cosmological surveys of matter distributions which include cosmic microwave background data sets, galaxy surveys, and observing gravitational leasing. Each of these surveys has the possibility to detect the signature suppression caused by neutrino masses, although extracting the relevant information is extremely challenging. In fact, the lightness of neutrinos makes them distinct from the rest of the matter in the Universe. Many cosmological and astrophysical probes are sensitive to the neutrino density. Therefore, it is not surprising that the comparisons of astrophysical and cosmological probes with theoretical predictions are prone to contribute to some of the most critical problems in particle physics, particularly, pinning down the neutrino masses and understanding their properties and perhaps their origin.

The distribution of matter in the Universe depends on the sensitivity of f_v, the fraction of neutrino density with respect to the total mater density, given by [22]

$$f_v = \frac{\Omega_v}{\Omega_m}, \qquad 1.12$$

where Ω_v is the neutrino energy density and $\Omega_m$is the matter density in units of critical density. The neutrino energy density is related to total neutrino masses as

$$\Omega_v h^2 = \frac{\sum_i m_i}{93.14}, \qquad 1.13$$

where $h \equiv H_0/(100\ kms^{-1}Mpc^{-1})$ is the Hubble constant normalized to current value of Hubble parameter H_0 and $\sum_i m_i$ represents total mass of the neutrino states that are currently non-relativistic, i.e. $\sum_i m_i = m_1 + m_2 + m_3$.

The cosmological method is only sensitive to the total neutrino mass but it is completely blind to neutrino mixing angles and possible CP-violating phases. This method, therefore, can only place the limits on the sum of the neutrino masses but remains insensitive to neutrino flavors and possible Majorana phases. Oscillation experiments have already determined that the difference of two neutrino masses is greater than 0.05eV (i.e. $\sqrt{|\Delta m_{32}^2|} \cong 0.05\ eV$), which provides the lower limit on the sum of the neutrino masses.

Since the results obtained from cosmological researches are sensitive to the model assumptions and the included data sets, there is no single cosmological limit on total neutrino mass. The upper bound obtained from the seven year release of WMAP data and Planck data are considered the most conventional and reliable cosmological limits on neutrino masses. Within the standard cosmological model, the Wilkinson Microwave Anisotropy Probe (WMAP) dataset alone is able to set a limit of $\sum_i m_i < 1.3\ eV$ at 95% CL and only Plank dataset has constrained $\sum_i m_i$ to be less than 0.6eV at 95% CL [23]. It is possible to obtain a significantly stronger upper limit on neutrino masses by combining CMB observations with measurements of Hubble constant H_0 and cosmic distances. For example, the upper bound obtained from WMAP dataset combined with Baryon Acoustic Oscillations (BAO) scale size and a direct determination of H_0 by the Hubble Space Telescope gives $\sum_i m_i < .58\ eV$[23]. Tighter bounds ($\sum_i m_i < .3\ eV$)have been obtained from combining CMB data, homogenous cosmological data, galaxy power spectrum data, and cluster abundance data [22]. However, none of these results are sensitive enough to distinguish individual neutrino mass.

In conclusion, cosmological observations can provide important information on the absolute mass scale of neutrino masses. The cosmological probes of neutrino masses are complementary to other lab based experiments, such as double beta decay and single beta decay.

Cosmological limits are also very model dependent.

1.5 Double Beta Decay Neutrino Mass Experiments

Double beta decay is a rare spontaneous nuclear transition originally proposed by Goeppert- Mayer in 1935 [24]. It takes places between two nuclei in which an even-even nucleus (Z, A) transforms into another even-even nucleus $(Z+2, A)$ with the emission of two electrons along with two antineutrinos. The lepton number is conserved in two-neutrino double beta decay $(2\nu\beta\beta)$ process and it is considered as a second order effect of beta decay, which occurs within the framework of the Standard Model. The $2\nu\beta\beta$ was first detected in 1987 [25] and is now observed in at least 11 nuclei with lifetimes longer than 10^{18} years. An interesting alternative to standard double beta decay is neutrinoless double beta decay $(0\nu\beta\beta)$, proposed by Furry in 1939 [26].The $0\nu\beta\beta$ violates the lepton number conservations and hence its existence demands physics beyond the SM of electroweak interactions. The 2νββ and the 0νββ nuclear reactions can be respectively represented as

$$2\nu\beta\beta \text{ decay}: (\mathrm{Z}, \mathrm{A}) \rightarrow (\mathrm{Z}+2, \mathrm{A}) + 2\mathrm{e}^{-} + 2\bar{\nu}_{\mathrm{e}}. \qquad 1.14$$

$$0\nu\beta\beta \text{ decay}: (\mathrm{Z}, \mathrm{A}) \rightarrow (\mathrm{Z}+2, \mathrm{A}) + 2\mathrm{e}^{-}. \qquad 1.15$$

The neutrinoless double beta decay process is particularly attractive in particle physics because it occurs only if the neutrino is a massive Majorana particle (i.e. an antiparticle of its own). This is the only known technique to determine whether neutrinos are Majorana or Dirac particles. That's why a huge amount of theoretical and experimental work has been pursued in order to predict and observe this process.

In double beta decay experiments, the available information such as sum of the electron energies, single electron energy, angular distributions, and number of daughter nuclei are usually collected. The $2\nu\beta\beta$ and the $0\nu\beta\beta$ processes can be distinguished from each other by the nature of distribution of total kinetic energy of the emitted electrons. In the case of $0\nu\beta\beta$ the energy of the recoiling nucleus is negligible and the total energy of the emitted electrons is approximately equal to the transition energy or Q-value. Therefore, a sharp peak at the transition energy is the signature of the $0\nu\beta\beta$ decay but a continuous bell distribution is expected for the $2\nu\beta\beta$ decay. The expected energy distribution of the $2\nu\beta\beta$ and the $0\nu\beta\beta$ are shown in Figure (1.2).

The half-life of the 0νββ is related to neutrino masses and it can be expressed as

$$[T_{0\nu}^{\frac{1}{2}}]^{-1} = G_{0\nu} \mid M_{0\nu} \mid^2 \langle m_{\beta\beta} \rangle^2 \qquad 1.16$$

where $G_{0\nu}$ is the phase space factor which can be precisely calculated, $M_{0\nu}$ is the nuclear matrix element and $\langle m_{\beta\beta} \rangle$ is the effective Majorana neutrino mass. If the $0\nu\beta\beta$ is detected, $M_{0\nu}$ can be calculated, but the calculation is model dependent. The nuclear matrix elements determined by different groups using different models are not consistent, which is one of the most critical issues in the $0\nu\beta\beta$ community.

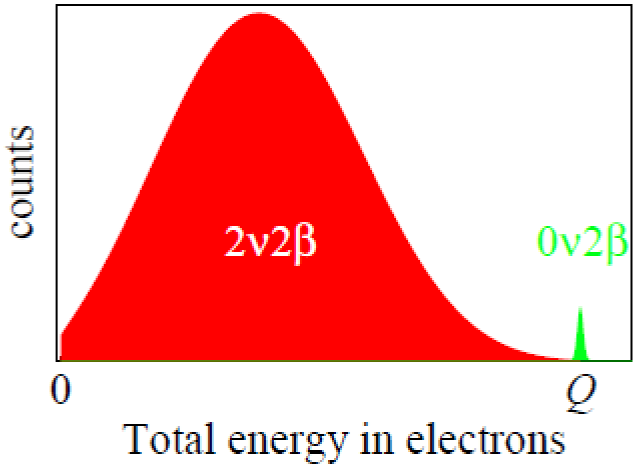

(FIG.1.2) *Expected energy spectrum of* $2\nu\beta\beta$ *(left) and* $0\nu\beta\beta$ *(right) processes* [27]

The effective mass can be expressed explicitly as a linear combination of the neutrino mass eigenstates:

$$\langle m_{\beta\beta} \rangle = \sum_{l}^{3} | U_{el} |^2 m_l e^{i\alpha_l}$$

$$= | U_{e1} |^2 m_1 + | U_{e2} |^2 m_2 e^{i\alpha_1} + | U_{e3} |^2 m_3 e^{i\alpha_2}, \qquad 1.17$$

where U_{e1}, U_{e2} *and* U_{e3} are the elements of the first row of neutrino mixing or PMNS matrix U_{el}. The elements of U_{el} and two squared mass differences have already been determined from the neutrino oscillation experiments (Table 1.1). The only unknown parameters in Equation (1.17) are $\langle m_{\beta\beta} \rangle$, the mass of the lightest neutrino, and the two Majorana phases.

$$\langle m_{\beta\beta} \rangle = cos_{12}^2 cos_{13}^2 m_1 + sin_{12}^2 cos_{13}^2 e^{i\alpha_1} m_2 + sin_{13}^2 e^{i\alpha_2} m_3 \,. \qquad 1.18$$

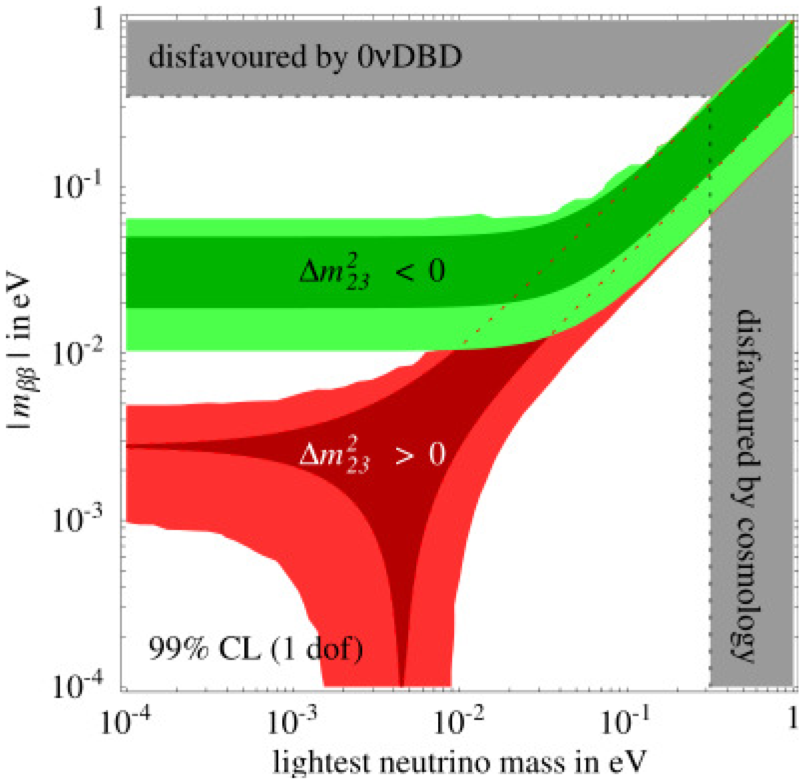

(FIG.1.3) *Expected ranges of effective Majorana mass as a function of the lightest neutrino mass in the normal and inverted hierarchy* [27].

The presence of the unknown Majorana phases (α_1, α_2) in the $\langle m_{\beta\beta} \rangle$ indicates the possibility of cancellation of terms in Equation (1.18). Figure (1.3) shows the allowed values for effective mass as a function of the lightest neutrino mass. In Figure (1.3), $m^2_{23} > 0$ represents the normal hierarchy with $m_{min} = m_1$, while $m^2_{23} < 0$ represents the inverted hierarchy with $m_{min} = m_3$. The darker regions correspond to the best-fit value of oscillation parameters with negligible errors.

Many experiments have been searching for 0νββ but none of them have found unquestionable positive evidence. Current experimental limits (90% C.L) for several interesting isotopes for 0νββ are reported on Table (1.2).

(Table 1.2) *Summery of current experimental limits on the half life* $T^{0\nu}_{1/2}$ *(yrs) and the effective mass* $m_{\beta\beta}$*(eV).The maximal and minimal limits on* $m_{\beta\beta}$ *is determined by nuclear matrix elements* [28].

Experiments	isotopes	$T^{0\nu}_{1/2}$(yrs)	$m_{\beta\beta}$(eV)
Heidelberg-Moscow	^{76}Ge	1.9×10^{25}	< 0.21 - 0.53
IGEX	^{76}Ge	1.6×10^{25}	< 0.25 - 0.63
NEMO-3	^{82}Se	3.2×10^{23}	< 0.85 - 2.08
NEMO-3	^{100}Mo	1.0×10^{24}	< 0.31 - 0.79
SOLOTVINO	^{116}Cd	1.7×10^{23}	< 1.22 - 2.30
CURRICINO	^{130}Te	2.8×10^{24}	< 0.27-0.57
DAMA	^{136}Xe	5.0×10^{23}	< 0.83 - 2.04

1.6 Single Beta Decay Experiments: Direct Measurement of Neutrino Mass

Direct measurements of neutrino mass are carried out by analyzing the kinematics of charged particles emitted together with flavor state neutrinos in suitable weak decays. To date the most sensitive electron neutrino mass measurement is based on studying the shape of the β spectrum. Relying only on the energy momentum conservation in the beta decay, the single beta decay experiments are the only model independent method to determine the electron neutrino mass with a sub-eV sensitivity. In these experiments a tiny deformation of the beta spectrum close to the end-point energy is studied. In β-decay, a radioactive nucleus (Z, A) is transformed into a slightly lighter nucleus (Z+1, A), with the emission of an electron and an antineutrino.

$$(Z,A) \rightarrow (Z+1,A) + e^- + \overline{\nu}_e \qquad 1.19$$

The single beta decay reaction, represented by equation (1.19) can be classified according to the selection rules presented on Table (1.3).

(Table 1.3) *Selection rules and classification of single β-decay transitions,* $L = \Delta J = |J_i - J_f|$*, where* J_i *and* π_i *are respectively the spin and parity of initial nuclides whereas* J_f *and* π_f *are spin and parity of final nuclides* [29].

L = 0,1	$\pi_f \pi_i = +1$	Allowed transitions
L = 0,1	$\pi_f \pi_i = -1$	Non unique first forbidden transitions
L > 1	$\pi_f \pi_i = (-1)^L$	Non unique L-th forbidden transitions
	$\pi_f \pi_i = (-1)^{L-1}$	Unique (L-1)-th forbidden transitions

The CPT theorem —which states that every relativistic quantum field theory has a symmetry that simultaneously reverses the charge C, the parity P, and the direction of time T— assures that the particle and antiparticle have the same rest mass. It is therefore common practice to call their mass simply "neutrino mass" for both of ν_e and $\overline{\nu}_e$. Assuming the neutrino mass to be negligible, the energy release in this process is given by

$$E_0 = M(A, Z-1)c^2 - M(A, Z)c^2 \qquad 1.20$$

where M is the atomic mass of the mother and daughter atoms. Neglecting the nucleus recoil energy, the most general form of the energy spectrum of the emitted electrons can be expressed as [29]

$$N_\beta(Z, E_\beta, m_{\nu_e}) = p_\beta E_\beta (E_0 - E_\beta)\sqrt{(E_0 - E_\beta)^2 - m_{\nu_e}^2 c^4}$$

$$\times F(Z, E_\beta) S(E_\beta)[1 + \delta_R(Z, E_\beta)] \qquad 1.20$$

where p_β and E_β are the energy and momentum of the emitted electron respectively.

The terms $F(Z, E_\beta)$, $S(E_\beta)$, $p_\beta E_\beta (E_0 - E_\beta)\sqrt{(E_0 - E_\beta)^2 - m_{\nu_e}^2 c^4}$, and $\delta_R(Z, E_\beta)$ are the Fermi function, the form factor, the phase factor, and the radiative electromagnetic correction respectively. The magnitude of beta spectra (the relative decay amplitude) can be expressed as

$$K\left(E_\beta\right) = \sqrt{\frac{N_\beta\left(Z, E_\beta, m_{\nu_e}\right)}{p_\beta E_\beta F\left(Z, E_\beta\right) S\left(E_\beta\right)\left[1 + \delta_R\left(Z, E_\beta\right)\right]}}$$

$$= \left(E_0 - E_\beta\right)\left(1 - \frac{m_{\nu_e}^2 c^4}{(E_0 - E_\beta)^2}\right) \qquad 1.21$$

The graph of the relative decay amplitude $K(E_\beta)$ with the energy of the emitted electron, which is generally linear, is known as a Kurie plot. For a massless neutrino ($m_{\nu_e} = 0$) and with a very high energy resolution, the Kurie plot is a straight line and it intersects the energy axis at E_0 . On the other hand, if the neutrino mass is nonzero ($m_{\nu_e} > 0$), the Kurie plot is distorted close to the end-point and intersects the energy axis at $E_0 - m_{\nu_e}$. Figure (1.4) shows the distortion of the spectrum for $m_{\nu_e} = 10eV$ (red color), in comparison to the undistorted β-spectrum (blue color) of the massless neutrino. The observation of distortion is therefore the great signature of an electron neutrino mass. Since the influence of neutrino mass is prominent near the end point region, most of the information of the neutrino mass is restricted to the region close to the end point or the final part of the Kurie plot. Below the end point region, the spectral distortion is statistically insignificant due to the rapidly rising count rate.

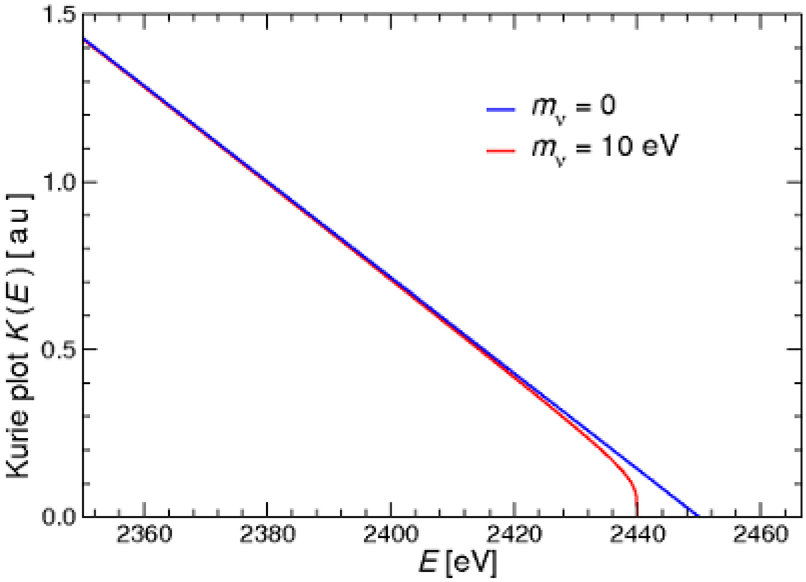

(FIG.1.4) *Expected ^{187}Re Kurie plot near the end point region, calculated for* $m_{\nu_e} = 0$ *(blue color) and* $m_{\nu_e} = 10eV$ *(red color)* [19]

In fact many factors affect the extraction of the neutrino mass from the end point study of the Kurie plot. The approximate fraction of events occurring in the region of interest is [29]

$$F(\Delta E) \approx 2\left(\frac{\Delta E}{E_0}\right)^3 \qquad 1.22$$

where ΔE is the size of the relevant energy interval of the region near the end point which is approximately $3m_{\nu_e}$ but is limited by detector energy resolution. From Equation (1.22), it is clear that a high sensitivity neutrino mass experiment requires β-emitting isotopes with low transition energy E_0. So far only three isotopes, namely tritium (^{3}H), rhenium (^{187}Re), and holmium (^{163}Ho) are able to fulfill this requirement. The details of the ^{163}Ho electron capture (EC) decay will be discussed in chapter 3. If we assume $m_{\nu_e} = 5eV$ then the useful event fraction is 4.5×10^{-7} for the case of rhenium beta decay (E_0 = 2.47 keV), while it is only 1.5×10^{-9} for tritium beta decay (E_0 = 18.6 keV). The evaluation of the detector response function is therefore crucial for the measurement of neutrino mass. In practice, no detector in the real world can have infinite energy resolution. Due to a finite energy resolution the shape of the β-spectrum near the end point is distorted in an opposite way with respect to the neutrino mass effect. The Kurie plot is seriously affected at the end point if the atom or molecule containing the decaying nucleus is left in an excited state. Because of the low count rate at the end point region, the analysis of the Kurie plot is complicated by the background due to cosmic rays and environmental radioactivity. The very low count rate in the region of interest demands a very low background, high luminosity, and a detector with very high energy resolution. The statistical fitting of the measured and calculated shape of the spectra gives us $m_{\nu_e}^2$.

1.6.1 The Spectrometric Measurements of the β-decay

Over the past half a century, various tritium β-decay neutrino mass experiments have been conducted using magnetic or electrostatic spectrometers. Magnetic spectrometers use the bending effect of an applied magnetic field to choose electrons with specified energy and achieved the most sensitive results until the 1990's. In the past few decades, electrostatic spectrometers with adiabatic magnetic collimation have replaced the magnetic spectrometers. In electrostatic spectrometers, the electrons are first collimated using specific magnetic field and then selected by means of an electrostatic potential barrier.

To date, the most sensitive limits for electron neutrino mass have been achieved using spectroscopic measurement of tritium beta decay. Tritium beta decay is an allowed transition given by

$$^{3}H \rightarrow {}^{3}He + e^{-} + \overline{\nu}_e \qquad 1.23$$

This transition has low end-point energy $E_0 = 18.6\,keV$ and a short half-life of $T_{\frac{1}{2}} = 12.3$ years. Because of the very high intrinsic decay rate of ^3H, it is possible to use thin sources. In practice ^{3}H is the only beta source that allows a large enough specific activity for an external source with high resolution electrostatic spectrometer. Furthermore, tritium has a simple configuration of the electron shell and hence the final state effects can be calculated accurately.

A summary of the four most sensitive experiments using spectrometers is presented in Table (1.4). So far, the most precise experimental results are obtained independently from the Mainz and Troitzk groups [33, 34]. The Mainz group used a frozen molecular tritium source whereas the Troitzk group utilized a gaseous molecular tritium source. Both groups used similar magnetic solenoidal retarding electrostatic spectrometers to measure the beta spectrum. Despite the quite different sources and the corresponding experimental problems associated with them, the results are remarkably close.

(Table 1.4) *Summary of the four most sensitive results obtained from spectrometric measurements (M stands for magnetic spectrometer and E stands for the electrostatic spectrometers)*

Experiments	Type	Source	m_ν(eV)
LANL [30]	M	T_2 (gas)	< 9.3
LNLN [31]	M	T_2 (gas)	< 7
Troitsk [32]	E	T_2 (gas)	< 2.05
Mainz [33]	E	T_2 (solid)	< 2.3

There are two main advantages that have made spectrometers the most sensitive devices. First, only electrons with energies very close to the end-point energy can be chosen. Therefore, the required statistics in the region of interest can be obtained in a reasonable amount of time. Second, it is possible to achieve very high energy resolution. For instance the next generation experiment, the Karlsruhe Tritium Neutrino (KATRIN) experiment, is expected to obtain energy resolution of less than 1eV. The major disadvantages of the spectrometer come from the fact that the radioactive source is external to the detector. In particular, the experimental data are affected by the energy loss due to excitation of atoms or molecules in the source, back scattering from the detector, reflection from the source substrate, etc. In other words, the detector response function is the convolution of the exact transmission function of the spectrometer with correction functions. Each of these correction functions carries its own systematic uncertainty; however, the correction function for energy loss has the dominant effect. Deconvolution of the response function is therefore mandatory to obtain a pure shape of an electron energy spectrum. In practice a precise evaluation of the response function is enormously complicated and subject to the systematical uncertainties.

1.6.1.1 The KATRIN EXPERIMENT

The Karlsruhe Tritium Neutrino (KATRIN) experiment is designed to measure the mass of the electron neutrino with a sensitivity of 0.2eV (90% CL) using an end point study of tritium beta spectrum [36]. In other words, the KATRIN experiment is the next generation tritium beta-decay experiment, scaling up the size and precision of previous experiments by one order of magnitude. The KATRIN experiment is currently being set-up on the site of the Tritium Laboratory at the Karlsruhe Institute of Technology (KIT) by an international collaboration. Figure (1.5) shows the KATRIN set up with main parts.

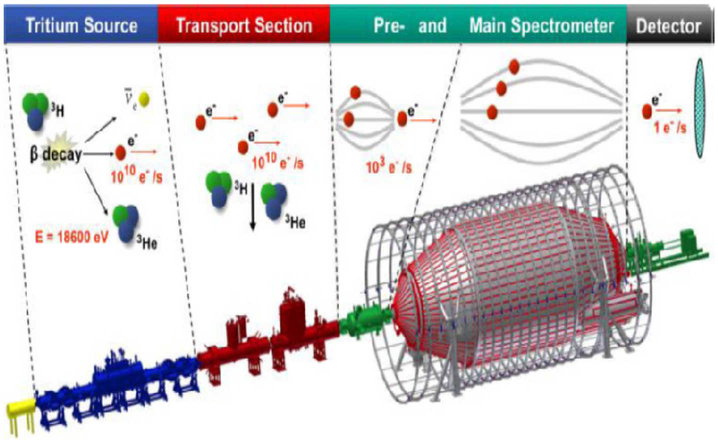

(FIG.1.5) *KATRIN experimental set up* [34]

The approximately 70 m long KATRIN set-up consists of five major sections as shown in Figure (1.5). The windowless gaseous tritium source (WGTS) consists of a 10m long tube which is surrounded by a superconducting magnet. An activity of 10^{11} Becquerel (Bq) is produced in the WGTS by injecting a flux of 10^{19} T_2-molecules per second, and the electrons from the decay are guided magnetically through the transport section towards the spectrometers. The transport section consists of the differential and cryogenic pumping sub-sections, and its main function is to reduce the T_2 flux entering in the spectrometer, and limit the flux to 10^5 T_2/ sec. A magnetic adiabatic collimation with electrostatic (MAC-E) filters serves as pre and main spectrometers for isolating the electrons with energies close to the end point energy. The background electrons are screened off electrostatistically using an inner grids system in the main spectrometer. The electrons which are able to overcome the potential barrier are then accelerated towards the detector. The energy resolution of the pre-spectrometer is 100eV, while the main spectrometer reaches a resolution of 0.93 eV. The KATRIN experiment will therefore improve the resolution by a factor of 20, as compared to the Mainz experiment, which had an energy resolution of 4.8 eV. In order to balance the Earth’s magnetic field, the main spectrometer is surrounded with air coils. The construction of the KATRIN experiment is expected to be finished by 2014.

1.6.2 The Calorimetric Measurements of Beta Decay for Neutrino Mass

An alternative to spectrometric measurement of the β-spectrum is the calorimetric approach, where the β-source is imbedded in the detector and all the decay energy is measured, except that taken away by the neutrino. Despite the fact that the most stringent results come from spectrometers, both the calorimetric and spectrometric methods have been considered two complementary techniques with the same goal.

Because of the internal source the calorimetric measurement are free from the systematic uncertainties of the external sources (i.e. the self-absorption problem, electron backscattering from the detector, and reflection of the source substrate). For example, part of the energy used to excite atomic or molecular levels is measured through the de-excitation of these states. However, a serious limitation of this approach comes from the fact that the complete beta spectrum is measured. It is necessary to keep the source activity low to avoid pulse pile-up effect, which otherwise would distort the shape of the energy spectrum. This leads to a serious limitation to the accumulation of the statistics. This limitation can be partially overcome by choosing a β-source with the lowest possible end point energy, and limited source activity. To date ^{187}Re and ^{163}Ho are the only possible β-sources for calorimetric measurement.

1.6.2.1 The Status of the ^{187}Re Isotope

^{187}Re has the lowest known transition energy (Q-value = 2.47 keV), a long life time ($T_{1/2}$= 243.2×10^9years), and large natural isotropic abundance (62.8 %). It is one of the best candidates for calorimetric measurements of neutrino mass. The first order uniquely forbidden transition of ^{187}Re β-decay is given by

$$^{187}\text{Re}\ (5/2^{+}) \rightarrow\ ^{187}\text{O}_{s}\ (1/2^{-}) + e^{-} + \overline{\nu}_{e}\ . \qquad 1.24$$

The activity of metallic ^{187}Re is approximately 1Bq/mg (one decay per second per milligram), which is suitable to calorimetric measurement. At temperatures below 1.6K, metallic rhenium becomes superconducting and therefore, possesses very low heat capacity at working the temperature of a microcalorimeter. So far, the MANU experiment at Genoa (Italy) [37] and the MIBETA experiment at Milano (Italy) [38] are the only two experiments based on calorimetric measurement of rhenium beta decay.

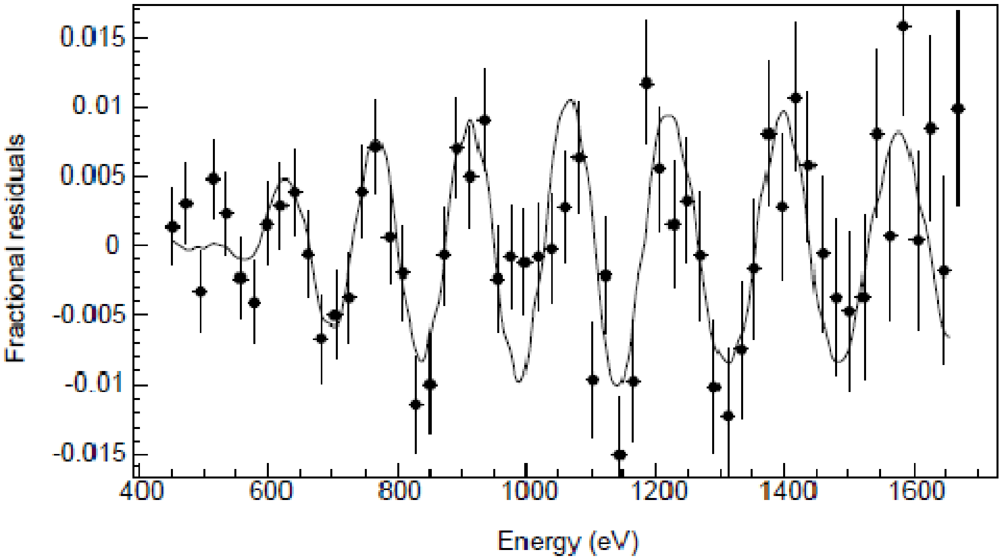

(FIG.1.6) *The BEFS effects for Re-β decay found from residuals of the best fit of the theoretical to the experimental data in MANU experiment* [37]

The MANU experiment used a 1.5 mg metallic Re single crystal attached with a neutron transmutation doped (NTD) thermistor and collected a statistic of about 10^{7} decays at a temperature of 60 mK. The particular oscillation superimposed onto a β-spectrum, which was an interference effect of the particle wave in the crystal lattice, was identified as a beta environmental fine structure (BEFS).The BEFS effect found in the MANU experiment is shown in Figure (1.6).The fit has yielded an endpoint energy of $E_0 = 2470eV$ and an neutrino mass upper limit of $m_{\nu_e} < 19$ eV at 90% C.L [29].

Because of the pile up problem it is almost impossible to obtain a competitive neutrino mass limit by using an existing microcalorimeter with a Re β- source of 1Bq. However, the MIBITA experiment, conducted by the collaboration of the Milano and the Como group, showed that the result obtained from a single detector system can be significantly improved by applying an array of micro-bolometers.

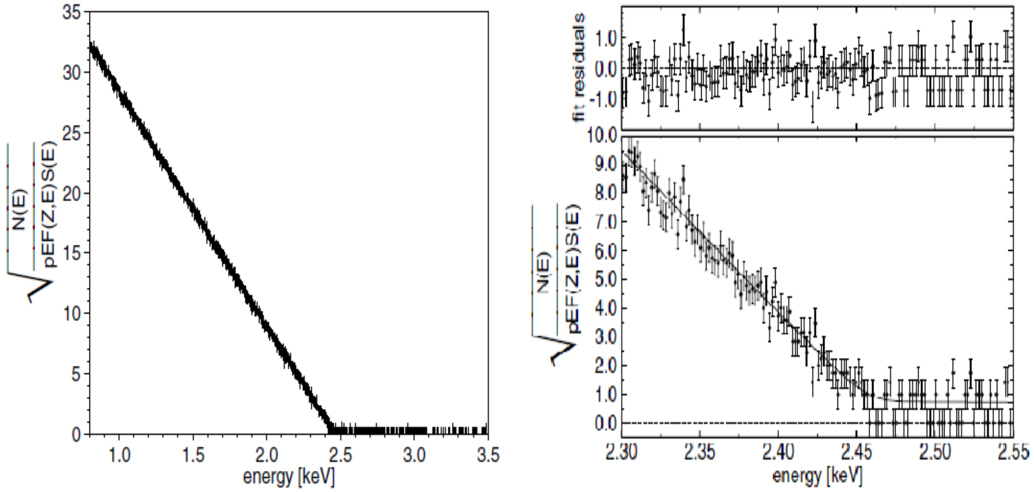

(FIG.1.7)*The Kurie plot for the rhenium β-spectrum obtained from eight detectors used in the MIBETA experiment (left). The fit residuals and fit function overlaid to the experimental data in the end point region (right)* [38].

The MEBITA experiment used an array of eight micro-bolometers. Each of the bolometer was equipped with an absorber containing silver perrhenate (AgReO4) mono-crystal of mass 300μg and a silicon implanted thermistor. Figure (1.7) shows the Kurie plot of Re-β-spectrum obtained from the high statistics calorimetric measurements, 6.2 x 10^6counts obtained from 5000hrs running. In Figure (1.7), p is the electron momentum, E is the electron kinetic energy, F (Z, E) is the Coulomb factor and S (E) is the shape factor.

The upper limit for electron neutrino mass obtained from the MIBETA experiment is $m_{\nu_e} \leq 15eV$ at 90% C.L [29].

1.6.2.2 The MARE Project

The "Microcalorimeter Arrays for a Rhenium Experiment" (MARE) is an international project, which aims to apply the calorimetric measurement technique to determine the electron neutrino mass [29]. The details of microcalorimeter or thermal detector are presented in Chapter 2. The MARE project has two staged approach. The first part of the MARE (MARE I) is going to check the present sensitivity limits of neutrino mass by improving the existing microcalorimeter technology. This includes the construction of the most sensitive microcalorimeters, such as transition edge sensor (TES) microcalorimeter or metallic magnetic calorimeter (MMC), using a source embedded absorbers. After operating an array of thousands of such detectors for more than five years, the future MARE project (MARE II) will be able to measure an electron neutrino mass with sub-electronvolt sensitivity ($m_{\nu_e} \sim 0.1eV/c^2$).The MARE II is therefore expected to play a crucial role to provide a competitive alternative and an independent check to the results from the KATRIN experiment.

Currently the MARE collaboration is considering both the ^{187}Re and the ^{163}Ho isotopes. The potential of a rhenium β-decay has been already demonstrated however the potential of a holmium electron capture (EC) decay is still being tested. The status of the MARE-Ho experiment is presented in Chapter 3.

Chapter 2
Microcalorimeters

2.1 Low Temperature Detectors: A Brief Overview

Low temperature detectors have several important applications in astrophysics, astronomy, particle physics, nuclear physics, and several other fields. In the last 5 decades, there has been an increasing interest in the development of cryogenic detectors and their use. Many different types of traditional detectors, such as solid state detectors, proportional counters, and position-sensitive detectors, coupled to either Bragg crystal or grazing-incidence diffraction grating, are being used in X-ray spectroscopy. However, these detectors cannot offer the performance necessary for many experiments. For example, energy resolution of solid state detectors is limited by statistical fluctuations in the number of electron-hole pairs.

Microcalorimeters and bolometers only differ in that a bolometer measures power, usually from a flux of incident photons, whereas a microcalorimeter records the energy due to a single event (e.g. photon, beta decay). A microcalorimeter is also known as a "quantum-calorimeter" because it is commonly used to measure the quanta of light (such as energy of an x-ray photon). Even though the concept of microcalorimeter is relatively new, the basic theory that describes the bolometer has been extended and widely applied to explain the operational principle of microcalorimeters. In 1982 John C. Mather [40] gave a complete non-equilibrium theory of a bolometer. Two years later, the microcalorimeter theory was described by Moseley, Mather, and McCammon [41]. Mather's formulation is also known as the ideal model, in which the microcalorimeter is treated as a single heat capacity device. A real microcalorimeter, however, consists of many different components connected via finite thermal conductance. As a consequence the actual performance is significantly more complicated. For example, there are additional sources of noise for the practical microcalorimeter and, in many cases, the bias current, applied magnetic field and many other parameters may affect the performance of the microcalorimeter.

This chapter will be focused on some of the important aspects of cryogenic microcalorimeter such as working principle, choice of thermometer and absorber, electro-thermal feedback, energy resolution, excess noise, and comprehensive model.

2.2 An Ideal Model: Working Principle

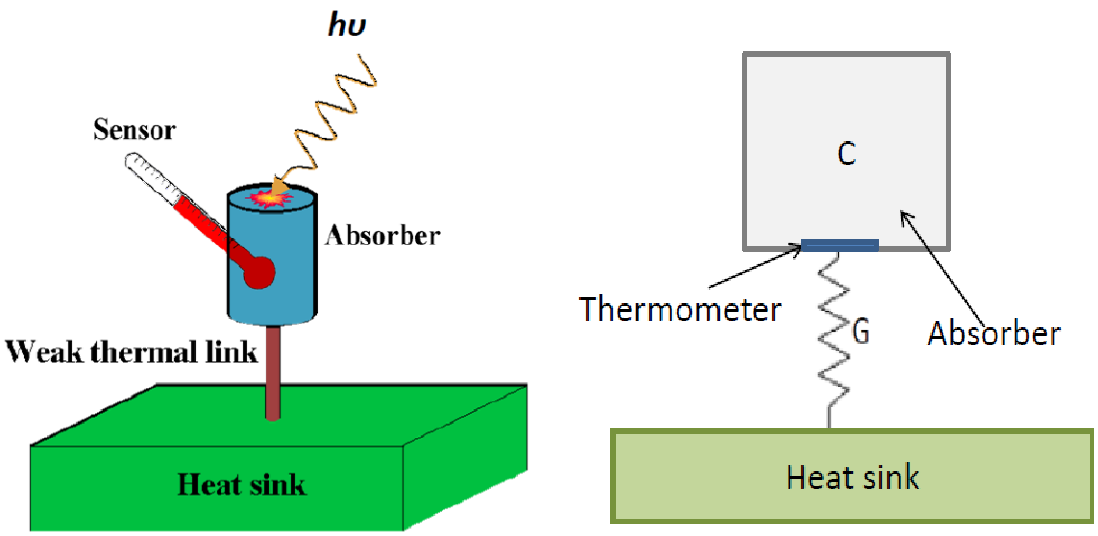

(FIG.2.1) *An ideal cryogenic microcalorimeter, schematic view (left) [42] and thermal sketch (right)*

A schematic view and thermal sketch of the ideal model of cryogenic microcalorimeter is shown in Figure (2.1). An absorber with the thermal capacity C is connected to a heat sink via a weak thermal link characterized by the thermal conductance G. A very sensitive thermometer or sensor is coupled to the absorber to measure the temperature variation of the detector. In the absence of input power or energy, other than Joule power, the temperature of the absorber T (t) is higher than the temperature of the heat sink T_S due to the Joule power dissipated into the thermometer. If an event occurs so that energy

E is deposited on the detector, then the absorber soaks up and thermalizes the energy. As a result the temperature of the detector increases. The detector temperature then decays back to the original temperature due to the heat flow through the weak thermal link to the heat sink. The initial rise in temperature of the device is determined by the absorbed energy and the heat capacity C. If we assume that the absorber is 100% efficient (i.e. it converts all the deposited energy in to thermal energy), the initial rise in temperature is

$$(\Delta \mathrm{T})_0 = \frac{\mathrm{E}}{\mathrm{C}} \qquad 2.1$$

The configuration of a bolometer is exactly the same except that it measures the power P deposited on the detector. The bolometer is therefore at a temperature which is steadily above the equilibrium one by a factor

$$(\Delta \mathrm{T})_0 = \frac{\mathrm{P}}{\mathrm{C}} \qquad 2.2$$

The decay time is the time required by the detector to decay back to its original state after absorption of energy so that the detector is ready to accept another event, or, in the case of a bolometer, the time for the detector to reach equilibrium if the external power is removed. The intrinsic time constant of the detector is given by

$$\tau = \frac{C}{G} \qquad 2.3$$

The change in temperature of the detector must be recorded on a time scale much smaller than τ. Rise time or thermalization time is the time required to increase the temperature of the detector as a result of absorption of energy. Rise time is a characteristic of the absorber material and is generally much smaller than the decay time. Therefore the detector warms up much faster than it cools down. The effective time constant τ_{eff} of the detector is determined by C, G and the electrothermal feedback (see section 2.4 for details).If an event occurs at $t = 0$, the temperature variation of the detector can be expressed as

$$\Delta T = \frac{E}{C} e^{-t/\tau_{eff}} \qquad 2.4$$

Therefore, the energy as well as the timing of the incident photon can be determined by recording the temperature variation of the detector.

The basic principle of a microcalorimeter is simple but the design and construction of practical microcalorimeters that fulfill the requirements of future x-ray missions or neutrino mass experiments is very challenging. Although microcalorimeters have proven to be the most powerful photon detector combining high energy resolution and quantum efficiency, there is always room for improvement for wider applications. The absorber and the sensor are the most critical part of a detector and therefore considerable efforts have been made to improve their performance.

2.2.1 Choice of Thermometer

The sensor must be capable of measuring a small variation in the temperature. To this end both resistive and non-resistive thermometers have been used as sensors. Transition edge sensors (TES) and semiconductor thermistors have become very popular thermometers for low-temperature detectors. Neutron transmutation doped (NTD) germanium thermistors and ion implanted silicon thermistors are commonly used semiconductor thermistors. Non-resistive or non-dissipative thermometers include capacitive, inductive, paramagnetic, and electron tunneling thermometers. In this work I will focus on resistive thermometers. The temperature sensitivity of a resistive thermometer is determined by a dimensionless parameter α, which can be defined as [49]

$$\alpha = \frac{\mathrm{dlogR}}{\mathrm{dlogT}} = \frac{\mathrm{TdR}}{\mathrm{RdT}} \qquad 2.5$$

where we assume that the resistance of the thermometer R is a function of only temperature T. Since the resistance of a semiconductor thermistor decreases with increase in temperature, α is relatively small and negative for a semiconductor thermistor. Figure 2.2 shows the resistance vs temperature plot for a typical germanium NTD thermometer.

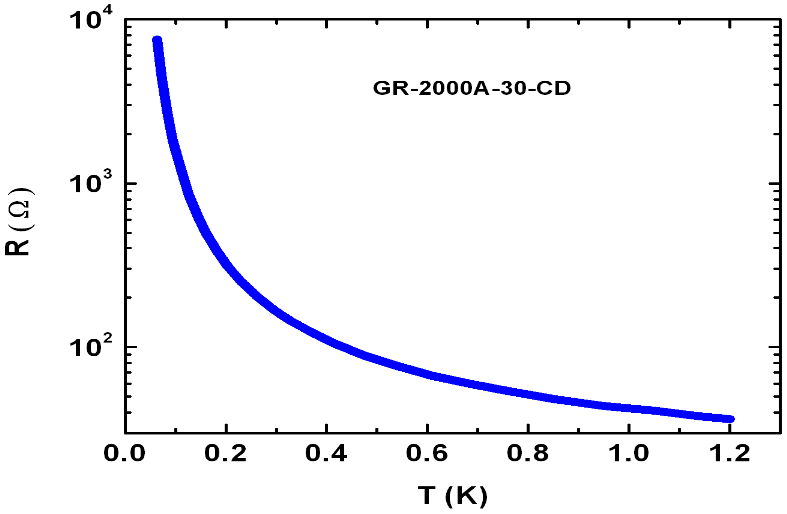

(FIG.2.2) *Resistance as a function of temperature for typical germanium NTD thermometer*

A transition edge sensor (TES) is a superconducting thin film that operates in the region between the superconducting and the normal state of the film. Since the superconducting transition occurs in a very narrow region, the operating temperature range of a TES microcalorimeter is very small and fixed by the manufacturing process. A tiny variation in temperature within the working range produces superconducting transitions leading to huge variation in resistance. However, the sensitivity decreases sharply as soon as a completely normal or completely superconducting state is reached. Figure (2.3) shows the resistance vs temperature plots that represent the superconducting transition of an Ir thin film at various bias currents. The measurement was done at the University of Miami. Because of its sharp transition the Ir thin film can be used as a TES sensor of a cryogenic microcalorimeter. TES detectors can have a faster response and better energy resolutions as compared to detectors using semiconductor thermistors. Despite having great potential in a variety of applications, TES thermometers have several different issues that must be considered carefully in the construction and operation of TES detectors. For example, a sharp transition can easily lead to instability and low saturation.

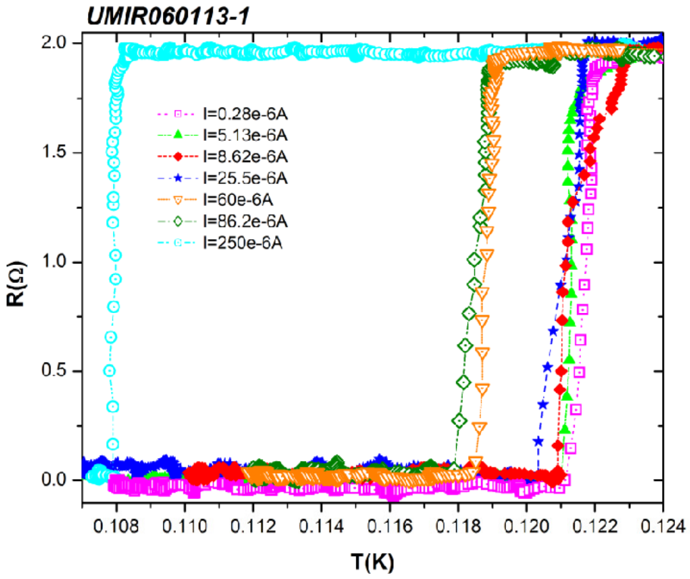

(FIG.2.3) *Resistance vs Temperature plots representing superconducting transition of an Ir thin film at different bias currents (measured at the University of Miami) [42]. The sharp phase transition implies that Ir thin film can be used as an ultra sensitive thermometer.*

The first TES bolometer was successfully demonstrated in the 1940s [43] but its practical application was very rare in the next several decades. The difficulties of matching the noise of TES detectors with the field-effect transistor (FET) amplifiers and stabilizing them within the extremely narrow superconducting transition region had become the major barriers to their adoption. The application of voltage biased operation with a superconducting quantum interface device (SQUID) has led to rapid growth in the development and application of TES detectors. SQUIDs can be easily impedance-matched to low- resistance (few Ohms) TES detectors, and it is also possible to multiplex the readout of TES detectors using SQUID amplifiers [44]. Arrays of large number of TES detectors are now being investigated and developed for a number of different applications. A voltage biased TES leads to negative electro thermal feedback (ETF), which counteracts excursions from the set point, and therefore the TES can be stably biased and self-regulated within the transition (details in section 2.5). In recent years, TES detectors are being developed and used in a variety of applications in astronomy, astrophysics, cosmology, particle physics, etc.

2.2.2 Choice of the Absorber

The design and construction of an absorber that works in a particular energy range of interest is one of the most challenging parts of the microcalorimeter fabrication. In order to achieve measurable temperature change for a small deposition of energy, an absorber should have high stopping power and low heat capacity. A low operating temperature is required so that the energy deposited is large relative to the random transfer of heat across the weak link. For negligibly small thermalization time, the thermal conductivity of the absorber must be very high at the working range of temperature.

Specific heat of a pure crystal at low temperature can be expressed as

$$c(T) = c_r(T) + c_{el}(T) \qquad 2.6$$

where c_r represents the lattice contribution (due to lattice vibrations) and c_{el} represents the electronic contribution (due to electronic excitation). At very low temperature $(T \ll \Theta_D)$, the lattice contribution is given by [46]

$$c_r(T) \cong \frac{12\pi^4}{5} k_B N_A \left(\frac{T}{\Theta_D}\right)^3 = aT^3 \qquad 2.7$$

where k_B is the Boltzmann constant, N_A is the Avogadro number and Θ_D is the Debye temperature, depending on the material characteristics.

The electronic contribution is determined by the metallic or superconducting nature of the material. In the case of a metal, the thermally excited conduction electrons can be treated as an ideal gas, which obeys the Fermi-Dirac distribution. The specific heat due to the electronic contribution can be expressed as [46]

$$c_{el}(T) = \frac{1}{2}\pi^2 k_B N_A \frac{T}{\theta_F} = \gamma T \quad for\ T \ll T_F \tag{2.8}$$

where Z is the number of electrons in the conduction band for each atom, R the molar gas constant, and Θ_F is the Fermi temperature. The higher the Fermi temperature of the metal, the lower the electronic heat capacity. The working temperature of a TES detector($\sim 0.1K$) is much below both the Debye and Fermi temperatures and the experimental specific heat capacity of metals can be expressed as

$$c = \gamma T + aT^3 \tag{2.9}$$

where γ and a are constants characteristic of the metal. At the temperature range of interest ($\sim 0.1K$), the electronic contribution dominates the phonon contribution. Therefore, with good approximation we assume that the specific heat capacity of metal in the working temperature range of a cryogenic microcalorimeter is given by

$$c = \gamma T \tag{1.10}$$

In case of superconductor, when the temperature falls below the transition temperature (T_c) the specific heat capacity abruptly increases to a higher value and then exponentially decreases with the argument proportional to -1/T [46]. If the temperature T is well below the transition temperature T_C of the superconductor, then the electronic contribution is negligibly small.

At low temperature, semiconductors usually have very low heat capacity due to the absence of electronic contributions. However, part of the energy absorbed by semiconducting absorber is used to form e-h pairs, which are trapped inside the absorber for long time. The statistical and positional variation of the e-h pairs degrades the thermalization efficiency of the absorber, which ultimately limits the energy resolution. Semiconductors with extremely low gap and excellent stopping efficiency, for example HgTe, have been used in x-ray astrophysics application [88]. In such case, the amount of energy converted into charge pairs is not significant and hence corresponding effect is negligible.

In order to achieve high quantum efficiency and uniform detector response we must choose suitable absorber material in which the most relevant parameters — heat capacity, thermal conductivity, diffusivity and stopping power — are optimized. A variety of metallic, superconducting, and semiconducting materials have been tested and used as an microcalorimeter absorber.

At the working temperature region of a microcalorimeter, semiconductors and superconductors have very low heat capacity due to absence of electronic contribution but most of the deposited energy goes into excitations of phonon spectrum (i.e. creation of e-h pair or quasi-particles), which relaxes to thermal distribution in a slow and complicated manner. On the other hand, the metallic absorbers have very fast detector response but relatively large heat capacity. Unlike semiconductors and superconductors, normal metals are free from metastable states and thus do not suffer from a degradation of energy resolution due to statistical variations in long-lived athermal excitations. In many cases the choice of absorber materials is also determined by the choice of thermometers. For example experiments using thermistor based detectors demand ultralow semiconducting or superconducting absorbers to meet the high energy resolution required by the experiments [37, 38]. However, it is possible to use metallic absorbers with TES based microcalorimeters [74].

2.3 Microcalorimeter Theory

The thermal conductance G is defined as [47]

$$G = \frac{dP}{dT} \qquad 2.11$$

where dP is the infinitesimal power through the heat link to the heat sink and dT is the temperature difference between the detector and the heat sink due to that power. The thermometer resistance of a microcalorimeter is read out by applying a small bias current as a consequence, a constant Joule power P_J is dissipated into the detector. In thermal equilibrium the power flowing out through the weak thermal link to the sink is equal to the power dissipated into the detector. If P_J is the only input power, the equilibrium state is reached when total power leaking through the heat link is equal the Joule power P_J. The Joule power dissipated on the detector can thus be obtained by integrating Equation (2.11), i.e.

$$P(T) = P_J(T) = \int_{T_S}^{T} G(T^{'})dT^{'} \qquad 2.12$$

The equilibrium temperature of the detector T is higher than the temperature of the sink T_s. The temperature dependence of the joule power is due to the temperature dependence of the thermometer resistance. Since the conductance G can typically be expressed as a power law of the detector temperature T, $G = G_0 T^{\beta}$, we can express Joule power as

$$P(T) = \int_{T_s}^{T} G_0 T'^{\beta} dT' = \frac{G_0}{\beta + 1}\left(T^{\beta+1} - T_s^{\beta+1}\right). \qquad 2.13$$

Dimensionally, G and G_0 are different but the numerical value of G_0 is equal to the value of G at 1K.The equilibrium temperature T can be determined numerically by solving Equation (2.13).If the detector is kept perfectly isolated from power sources other than the Joule power and an additional power W is deposited on the detector, then the detector temperature is raised. The total power input $(P + W)$ must be equal to the sum of the increase in internal energy of the detector and power flowing out through the thermal link. The response of the system can be investigated by solving a power flow equation given by

$$C\frac{dT_D}{dt} + \int_{T_s}^{T_D} G(T')dT' = W + P(T_D) \qquad 2.14$$

where C is the heat capacity of the detector (combined heat capacity of the thermometer and absorber), T_D is the temperature of the detector, T_S is the temperature of the heat sink. The first term in the left side represents the power stored into the heat capacity of the detector, while the second term represents the power leak from the detector (rate of flow of heat from to the heat sink via the thermal link).

If ΔT is the small increase in temperature of the detector above the equilibrium temperature T, then the detector temperature T_D can be expressed as $T + \Delta T$. Equation (2.14) can be written as

$$C\frac{d(T + \Delta T)}{dt} = W + P(T + \Delta T) - \int_{T_s}^{T} G(T')dT' - \int_{T}^{T+\Delta T} G(T')dT' \qquad 2.15$$

In the small signal limit $(\Delta T \ll T)$, we can expand second integral using the Taylor expansion formula

$$f(x) = f(a) + \frac{df(x)}{dx}\bigg|_a \Delta x + O(x^2) + \cdots \quad where \quad \Delta x = x - a$$

Considering only the first order of ΔT, the second integral Equation (2.15) becomes

$$\int_T^{T+\Delta T} G(T')dT' = \int_T^{T+\Delta T} \left[G(T) + \frac{dG(T')}{dT'}\bigg|_T \Delta T\right] dT' \approx G(T)\Delta T \qquad 2.16$$

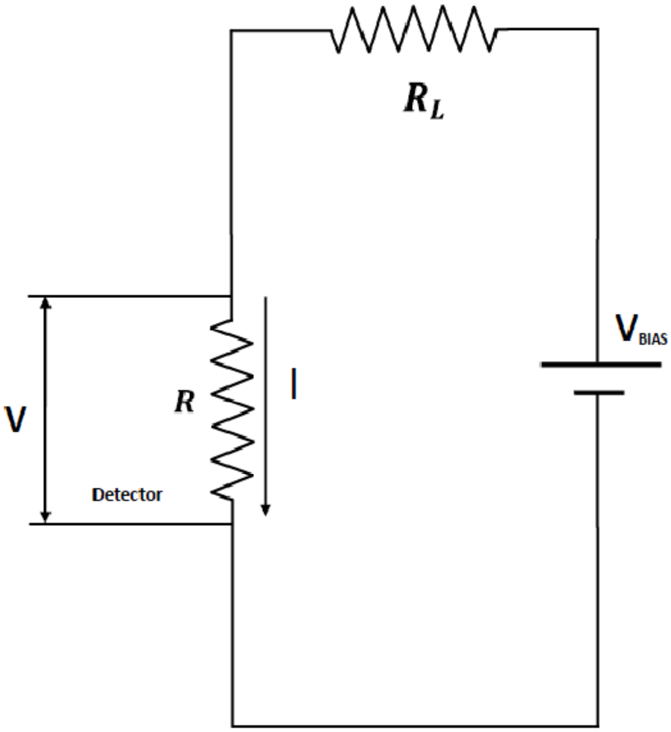

(FIG.2.4) *Typical thermometer bias circuit with the thermometer resistance R is and the load resistance R_L.*

The Equation (2.15) can, therefore, be expressed as

$$C\frac{d(\Delta T)}{dt} = W + P(T + \Delta T) - P(T) - G(T)\Delta T \qquad 2.17$$

If we define $P(T + \Delta T) - P(T) = \Delta P$ and use G (T) = G for simplicity, Equation (2.17) becomes

$$C\frac{d(\Delta T)}{dt} + G\Delta T - \Delta P = W \qquad 2.18$$

In a typical read out circuit shown in Figure (2.4) the thermometer resistance R is in series with the load resistance R_L. The detector is said to be constant voltage biased if we use a constant voltage source ($R_L \ll R$) and constant current biased if we use a constant current source ($R_L \gg R$).

Differentiating the Joule power $P\ (T)\ =\ IV$ with respect to T we get

$$\frac{dP(T)}{dT} = I\frac{dV}{dR}\frac{dR}{dT} + V\frac{dI}{dV}\frac{dV}{dR}\frac{dR}{dT} \qquad 2.19$$

We have

$$\frac{dV}{dI} = -R_L, \qquad \frac{dR}{dT} = \frac{\alpha\, R}{T}, and\ \ \frac{dV}{dR} = \frac{R_L}{R+R_L}I \qquad 2.20$$

where the first, second , and third expressions in Equation (2.20) are respectively obtained from the bias circuit shown in Figure (2.4), the definition of α (Equation 2.5), and differentiating $V\ =\ RT$.

Solving Equations (2.19) and (2.20) we get

$$\Delta P = -\frac{\alpha P}{T}\frac{R-R_L}{R+R_L}\Delta T \qquad 2.21$$

which represents the electrothermal feedback (ETF) term. The ETF is positive if bias power P increases with the increase in temperature T and vice versa. The sign of ETF is determined by the sign of α and the magnitude of R_L. A voltage biased thermistor produces positive ETF, while a voltage biased TES produces negative ETF. Similarly a current biased thermistor produces negative ETF and a current biased TES thermometer produces positive ETF. The term $\alpha P(R-R_L)/T(R+R_L)$ is called virtual thermal conductance and it is represented as G_{ETF}. The effective thermal conductance is then given by $G_{eff} = G +\ G_{ETF}$. Therefore, Equation (2.18) can be written as

$$C\frac{d(\Delta T)}{dt}+G_{eff}\Delta T=W \qquad 2.22$$

The response of the microcalorimeter or bolometer can be determined by solving Equation (2.22). If a single event with energy E is absorbed by the detector at time $t_0 = 0$, then W is a delta function of the form

$$W=E\delta(t-t_0)=E\,\delta(t) \qquad 2.23$$

Solving Equation (2.22) and (2.23) we get

$$\Delta T=\frac{E}{C}e^{-t/\tau_{eff}} \qquad 2.24$$

where $\tau_{eff}={}^{C}/_{G_{eff}}$ is the effective time constant. The Equation (2.24) is the time domain solution (detector response) after absorption of a single event with energy E assuming that the rise time is negligible as compare to τ_{eff} . After absorption of a single event, the temperature of the detector decays exponentially with the time constant τ_{eff}. After absorption of single event energy E, the voltage and current response of the detector can be obtained by using expressions in Galeazzi & McCammon (2003) [47].

$$\Delta V=\frac{V\alpha}{T}\frac{R_L}{R+R_L}\Delta T=\frac{V\alpha}{T}\frac{R_L}{R+R_L}\frac{E}{C}e^{-t/\tau_{eff}} \qquad 2.25$$

$$\Delta \mathrm{I}=-\frac{\alpha \mathrm{I}}{\mathrm{T}}\frac{\mathrm{R}}{\mathrm{R}+\mathrm{R_L}}\Delta \mathrm{T}=-\frac{\alpha \mathrm{I}}{\mathrm{T}}\frac{\mathrm{R}}{\mathrm{R}+\mathrm{R_L}}\frac{E}{C}e^{-t/\tau_{eff}} \qquad 2.26$$

Alternatively, the solutions of Equation (2.22) can be obtained in the frequency domain by using the Fourier transform. Fourier transform and its first derivative can be expressed as

$$\tilde{f}(\omega)=\frac{1}{\sqrt{2\pi}}\int_{-\infty}^{+\infty}f(t)e^{-i\omega t}\,dt \leftrightarrow f(t)=\frac{1}{\sqrt{2\pi}}\int_{-\infty}^{+\infty}\tilde{f}(\omega)e^{i\omega t}\,dt,$$

$$\frac{d}{dt}f(t)=i\omega\tilde{f}(\omega)\ \ with\ \ i=\sqrt{-1}$$

The Fourier transform of Equation (2.22) is

$$i\omega C\Delta T(\omega) + G_{eff}\Delta T(\omega) = W(\omega), \qquad 2.27$$

Therefore, the temperature variation of the detector in frequency domain can be expressed as

$$\Delta T(\omega) = \frac{1}{G_{eff}}\frac{1}{1 + i\omega\tau_{eff}}W(\omega). \qquad 2.28$$

If the detector absorbs a single event energy E, we can determine W (ω) as

$$W(\omega) = \frac{1}{\sqrt{2\pi}}\int_{-\infty}^{+\infty} E\,\delta(t - t_0)e^{-i\omega t}dt = \frac{1}{\sqrt{2\pi}}\,Ee^{-i\omega t_0} \qquad 2.29$$

Therefore in frequency domain, the temperature evolution of the detector after absorption of energy E can be expressed as

$$\Delta T(\omega) = \frac{1}{G_{eff}}\frac{1}{1 + i\omega\tau_{eff}}\frac{E}{\sqrt{2\pi}}e^{-i\omega t_0} \qquad 2.30$$

Equation (2.30) represents the temperature response of the detector in frequency domain. The voltage and current response can be determined by using Equations (2.25) and (2.26).Therefore we can investigate the temperature, voltage, and current response of the detector in both time and frequency domain.

2.4 Electrothermal Feedback and TES Detector

When a TES is biased with a current source ($R_L \gg R$), the Joule heating, $P\,(T) = I^2R(T)$, increases with increasing temperature and the electrothermal feedback (ETF) is positive. On the other hand if the TES is biased with a voltage source ($R_L \ll R$), the Joule heating, $P\,(T) = V^2/R(T)$, decreases with increasing temperature and the ETF is negative. The negative ETF stabilizes the close loop gain making circuit performance uniform and reproducible. It also reduces nonlinearity effects and increases the dynamic range. Therefore, TES microcalorimeters are commonly voltage biased.

Using the expression derived in section 2.3 (Equation 2.24), thermal response of the detector after absorption of single event energy E is

$$\Delta T(t) = \frac{E}{C} e^{-t/\tau_{eff}} \qquad 3.31$$

$$\text{with } \tau_{eff} = \frac{C}{G_{eff}} = \frac{C}{G + G_{ETF}} \text{ and } G_{ETF} = \frac{P\alpha}{T}\frac{R - R_L}{R + R_L} \qquad 2.32$$

In order to investigate the effect of the ETF on the performance of a TES microcalorimeter we consider both the current bias and the voltage bias conditions.

Under the current bias condition ($R_L \gg R$) or positive electrothermal feedback,

$$G_{ETF} = -\frac{P\alpha}{T} \;\; and \;\; \tau_{eff} = \frac{\tau}{1 - \frac{P\alpha}{GT}}. \qquad 2.33$$

Since α is positive, the quantity $P\alpha/GT$ is always positive for a TES detector. Thus, the positive ETF makes the effective time constants longer than the intrinsic time constant τ, making the detector slower. In other words a TES detector with positive ETF takes a longer time to decay back to the original temperature after accepting an event. On the other hand, for the constant voltage bias condition ($R_L \ll R$) we have

$$G_{ETF} = \frac{P\alpha}{T} \;\; and \;\; \tau_{eff} = \frac{\tau}{1 + \frac{P\alpha}{GT}}. \qquad 2.34$$

Thus, the negative ETF reduces the decay time (pulse duration), making the detector faster. For constant V (perfect voltage bias), and assuming that the resistance depends only on temperature, we have

$$\Delta I = -\frac{V}{R^2}\frac{\partial R}{\partial T}\Delta T. \qquad 2.35$$

Using the definition of α (Equation 2.5) we get

$$\Delta I = -\frac{\alpha V}{RT}\Delta T \qquad 2.36$$

From Equations (2.31) and (2.36) we obtain

$$\Delta I = -\frac{E\alpha V}{CRT}e^{-t/\tau_{eff}} = \Delta I_0 e^{-t/\tau_{eff}} \qquad 2.37$$

where $\Delta I_0 = -E\alpha V/CRT$ is the initial drop in current due to the absorption of energy E. The detector remains stable as long as

$$\frac{P\alpha}{GT} > -1\,. \qquad 2.38$$

Therefore a voltage biased TES is stable against the thermal runaway. A decrease in Joule power with an increase in the temperature acts as a restoring force. The power input to the TES is the Joule power V^2/R and the power output to the heat sink through the weak thermal link is given by Equation (2.13). In thermal equilibrium

$$P = \frac{V^2}{R} = \frac{G_0}{\beta+1}\left(T^{\beta+1} - T_s^{\beta+1}\right). \qquad 2.39$$

Substituting P from Equation (2.39) and $G = G_0 T^{\beta}$, we get

$$\frac{P\alpha}{GT} = \frac{\alpha}{\beta+1}\left[1 - \left(\frac{T_s}{T}\right)^{\beta+1}\right] \qquad 2.40$$

Solving Equation (2.34) and (2.40), we obtain

$$\tau_{eff} = \frac{\tau}{1 + \frac{\alpha}{\beta+1}\left[1 - \left(\frac{T_s}{T}\right)^{\beta+1}\right]} = \frac{\tau}{1 + \frac{\alpha \emptyset}{\beta+1}}. \qquad 2.41$$

where $\emptyset = \left[1 - \left(\frac{T_s}{T}\right)^{\beta+1}\right]$ and its value varies between 1 and 0 depending on the temperature of the superconducting film and the heat bath. In the extreme negative feedback regime ($T_s^{\beta+1} \ll T^{\beta+1}$ and $\beta + 1 \ll \alpha$) we obtained

$$\tau_{eff} = \frac{\tau}{1+\frac{\alpha}{\beta+1}} \approx \frac{\tau(\beta+1)}{\alpha}. \qquad 2.42$$

For $\alpha \leq 100$, the time constant of a TES detector is shortened by more than two orders of magnitude with negative ETF. Fast response does not improve the signal to noise ratio, however, it does increase the useful count rate and avoids the possible degradation in energy resolution due to the pulses piling up. The increase in useful bandwidth keeps the TES in its linear range even when multiple events arrive simultaneously.

In principle it is possible to decrease the time constant by increasing the value of G, but the input power must be increased proportionally to keep the thermometer in the working temperature range. Practical limitations come from the fact that input power cannot be increased above a certain boundary to avoid nonlinear effects. Therefore after a limit, the only way to decrease the time constant of the detector is by increasing α. Transition edge sensors have the highest known α and therefore are becoming the detector of choice. Furthermore, a negative ETF has several other benefits. The TES is self-biased and self-calibrated over a certain range of signal power and biased voltage [45]. This feature has been widely applied for an array of TES thermometers. If the heat sink is well below the transition temperature, the TES response is almost insensitive to the temperature fluctuation in the sink and hence the TES temperature is stabilized. It is also possible to apply an external electrical feedback to a cryogenic microcalorimeter [54].

2.5 The Generalized Responsivity and the Complex Dynamic Impedance

The responsivity of the detector can be defined as the output signal measured for a given input power. The voltage and current sensitivity can be expressed as [47, 49]

$$S_V(\omega) = \frac{\Delta V(\omega)}{W(\omega)}\ , \quad and\ \ S_I(\omega) = \frac{\Delta I(\omega)}{W(\omega)}. \qquad 2.43$$

Using Equation (2.25) and (2.26) , we can obtain

$$\frac{\Delta V}{V} = \alpha \frac{R}{V}\frac{dV}{dR}\frac{\Delta T}{T} \quad and \quad \frac{\Delta I}{I} = \alpha \frac{R}{I}\frac{dI}{dR}\frac{\Delta T}{T}. \qquad 2.44$$

The generalized response of the detector can be expressed as

$$\frac{\Delta X}{X} = \alpha\, A_{tr}\frac{\Delta T}{T}. \qquad 2.45$$

Where X is the generalized signal and A_{tr} is the transducer sensitivity defined as

$$A_{tr} = \frac{R}{X}\frac{dX}{dR}. \qquad 2.46$$

Solving Equations (2.28) and (2.45), we get

$$\frac{\Delta X}{X} = \frac{1}{G_{eff}}\frac{1}{1 + i\omega\tau_{eff}}\frac{\alpha\, A_{tr}}{T}W(\omega). \qquad 2.47$$

Therefore the generalized sensitivity of the detector can be expressed as

$$S(\omega) = \frac{\Delta X(\omega)}{W(\omega)} = \frac{1}{G_{eff}}\frac{1}{1 + i\omega\tau_{eff}}\frac{X\alpha\, A_{tr}}{T}. \qquad 2.48$$

At working temperature, the power dissipated on the detector is not only determined by the resistance $R\,(V/I)$ of the detector but also ETF. Therefore, performance and characteristics of the detector are often described by complex dynamic impedance Z (ω). It is an experimentally measurable quantity which can be defined as

$$Z(\omega) = \frac{dV(\omega)}{dI(\omega)}. \qquad 2.49$$

If we differentiate $V = IR$ and use the definition of α, we get

$$dV = IdR + RdI = \frac{IR\alpha}{T}\ dT + RdI. \qquad 2.50$$

The Fourier transform of Equation (2.18) with $W = 0$ gives

$$dT = \frac{dP}{G\left(1 + i\omega \frac{C}{G}\right)} = \frac{VdI + IdV}{G(1 + i\omega\tau)}, \qquad 2.51$$

where $dP = VdI + IdV$ is obtained by differentiating the joule power $(P = IR)$ dissipated into the thermometer. Substituting dT from the Equation (2.51) into Equation (2.50) we obtain

$$Z(\omega) = \frac{dV(\omega)}{dI(\omega)} = R\,\frac{1 + \mathcal{L}_0 + i\omega t}{1 - \mathcal{L}_0 + i\omega t} \qquad 2.52$$

$$with\ \ Z_0 = Z(\omega = 0) = \ R\,\frac{1 + \mathcal{L}_0}{1 - \mathcal{L}_0} \quad and\ Z_\infty = Z(\omega \to \infty) \to R \qquad 2.53$$

where we define $\mathcal{L}_0 = \alpha P/GT$. In the small signal limit, the voltage responsivity of an ideal microcalorimeter or bolometer can be expressed as [47]

$$S_V(\omega) = \frac{1}{2I}\frac{(Z_0/R) - 1}{(Z_0/R_L) + 1}\frac{1}{1 + i\omega\tau_{eff}}. \qquad 2.54$$

2.6 Major Noise Sources and Energy Resolution

In 1982, Mather identified four primary noise sources — Jonson noise, phonon or thermal fluctuations Noise (TFN), photon noise, and excess noise — in the simplest model (Ideal model) of cryogenic bolometer [40]. Thermometer Johnson noise and phonon noise are intrinsic to the detector. The only way to reduce these unavoidable fundamental sources of noise is the optimization of the device itself. Johnson noise is due to the thermal fluctuations on any resistive elements at a given temperature and it is associated with the thermometer resistance, shunt resistance and load resistance. Phonon noise is due to a random transfer of energy carriers via the thermal link and it is described as power noise on the detector. Read out electronics (amplifier), load resistor Johnson noise and photon background noises are the external noise sources. The maximum theoretical energy resolution of a microcalorimeter or bolometer is usually calculated from the noise equivalent power (NEP). The general expression for the full width at half maximum (FWHM) energy resolution is [49]

$$\Delta E_{FWHM} = 2.355\left(\int_0^{\infty} \frac{4df}{NEP^2}\right)^{-1/2} . \qquad 2.55$$

The NEP is the necessary power at the input of the detector so that it will produce an output signal equal to the noise signal at the output. In practice, the NEP can be calculated by taking the ratio of the noise signal at the output of the detector ΔY (ω) to the responsivity of the detector S (ω) or by taking the square root of the power spectral density of the power-referred noise.

$$NEP = \frac{\Delta Y}{S(\omega)} \qquad 2.56$$

The device can be optimized so that the contribution from external noise sources is negligible. Therefore the detection limit of the microcalorimeter or bolometer is generally determined by the Thermometer Johnson noise and phonon noise [41]. The thermometer Johnson noise (Nyquist noise), assuming equilibrium conditions, can be considered as a voltage source in series with the thermometer resistance R. The equilibrium expression of noise spectral density is

$$e_J = \sqrt{4k_B RT} \quad V/\sqrt{Hz}, \qquad 2.57$$

where k_B is Boltzmann's constant and T is the equilibrium temperature of the thermometer. It is currently well understood that the equilibrium condition for the

Johnson noise is insufficient to characterize the microcalorimeter performance. A discussion of the non-equilibrium Johnson noise is reported in section 2.7.

For a finite conductance G, phonon noise consists of a white noise spectrum with a power spectral density$\sqrt{4k_BGT^2}$. Details of the nature of the heat link are essential for the determination of the power spectral density or NEP associated with the TFN. Assuming that the length of the link is large compared to the mean free path of the energy carriers (diffusive conductivity), the power spectral density distribution due to the temperature fluctuation can be calculated as [40]

$$p_{TFN} = NEP_{phonon} = \sqrt{4k_BGT^2}\left(\frac{\frac{\int_{T_s}^{T}(T'k(T'))^2}{(Tk(T))^2}dT'}{\int_{T_s}^{T}\frac{k(T')}{k(T)}}\right)^{\frac{1}{2}}, \qquad 2.58$$

where $k(T')$ is the thermal conductivity of the heat link material. Since the noise sources are independent, the total NEP^2 can be obtained by simply adding the individual contributions.

Using optimum filtering, the theoretical energy resolution was calculated by McCammon [49]. If α is adequately large ($\alpha \gg 1$), the theoretical energy resolution can be expressed as

$$\Delta E_{FWHM} \propto \sqrt{k_BT_s^2C_s/\alpha}\,. \qquad 2.59$$

The details of theoretical derivation of the energy resolution of a TES microcalorimeter were presented by K. Irwin and G. Hilton [51]. In the limit of strong electrothermal feedback, energy resolution can be expressed as

$$\Delta E_{FWHM} = 2.355\sqrt{\frac{4k_B T_0^2 C}{\alpha}\sqrt{\frac{\beta+1}{2}}}. \qquad 2.60$$

Chapter 3

The Ho-Experiment

3.1 ^{163}Ho as an Alternative to ^{187}Re

The potential of ^{187}Re embedded absorbers has been demonstrated [29]. However, the long decay time (half -life ~43x10^9 years) of the ^{187}Re isotope puts serious restrictions on the extension of the experiment to achieve an electron neutrino mass with sub-electronvolt sensitivity, as a huge mass of radioactive material is needed to achieve the required statistics in a reasonable amount of time. This puts serious limitations on the design and fabrication of the experiment. Therefore, the possibility of using the ^{163}Ho electron capture (EC) decay is being considered as a viable alternative to the ^{187}Re β decay.

The ^{163}Ho EC decay has been used as an alternative to single beta decay for the direct determination of electron neutrino mass since the'80s [60, 61]. The ^{163}Ho EC decay occurs with record low transition energy (Q~ 2.6 keV) and a half-life (4500 yrs) much shorter than that of the ^{187}Re β decay.

The ^{163}Ho EC decay can be represented as [67]

$$^{163}Ho + \quad e^- \;\rightarrow\; ^{163}Dy'_j + \nu_e \;\rightarrow\; ^{163}Dy + E_j \; + \nu_e. \tag{3.1}$$

This is an allowed transition in which the spin and parity of the nuclei obey the selection rules $\Delta J = 1,\ \pi_f \pi_j = +1$ [64]. In this ground state to ground state nuclear transition, the nucleus of a ^{163}Ho isotope captures an electron from different shells (M or higher) and transforms into the excited state (^{163}Dy$'_j$) with emission of an electron neutrino. The de-excitation energy E_j (the dissipated binding energy of the electron hole in the final atom) is released via X-rays, Auger electrons, Coster-Kronig transitions, and photons emitted by inner Bremsstrahlung. The energy of a neutrino produced in the de-excitation of $^{163}\mathrm{Dy}_j'$ is given by Q- E_j where, Q is the end point energy or transition energy that can be determined from the mass difference of the mother and daughter atoms in their ground state (i.e. Q = M(^{163}Ho)-M(^{163}Dy)). Because of the very low measured Q-value (about 2.6 KeV), only electrons from M or higher shells (i.e. M_1, M_2, N_1, N_2, O_1, O_2, and P1) can be captured. A series of lines, each representing the electron capture from a specific shell, is expected. These lines have natural width of a few eV, and therefore the real energy spectrum of neutrinos in EC decay is a continuous curve with noticeable peaks (Figure 3.1).

At least three independent methods —absolute M capture rate or M/N capture rate [61], Inner Bremsstrahlung (IB) [60], and total calorimetric absorption spectrum end-point [65] — have been suggested to evaluate electron neutrino mass from the Holmium EC decay.

The calorimetric method has been considered by embedding the ^{163}Ho source into the absorber of a microcalorimeter. This experiment was first purposed by DeRujula and Lusignoli in 1982 [65] and it is currently being developed [66]. In the calorimetric experiment, all the decay energy other than the energy taken away by the escaped neutrinos is recorded and the neutrino mass determination is based on the kink search at the energy spectrum end point.

3.2 Calorimetric De-excitation Energy Spectrum of the ^{163}Ho EC Decay

The total capture rate from all shells can be obtained by summing over the possible levels of the captured electrons [64]

$$\lambda_{EC} = \frac{G_\beta^2}{4\pi} \sum_j n_j C_j \beta_j^2 B_j \left(Q - E_j\right) \left[(Q - E_j)^2 - m_\nu^2\right]^{1/2} \qquad 3.2$$

where $G_\beta = G_F \cos(\theta_c)$ is the beta decay coupling constant, n_j is the fraction of occupancy of the j-th shell, C_j is the nuclear shape factor of the decay, β_j is the Coulomb amplitude of the electron wave radial wave function (essentially the modulus of the wave function at the origin), and B_j is an atomic correction for electron exchange and overlap. Every single contribution in the sum of the Equation (3.2) depends on neutrino mass.

The expected spectrum of the calorimetric de-excitation energy E_C is [65]

$$\frac{d\lambda_{EC}}{dE_C} = \frac{G_F^2 cos^2\theta_C}{4\pi}(Q - E_C)\sqrt{(Q - E_C)^2 - m_\nu^2}$$

$$\times \sum_j n_j C_j \beta_j^2 B_j \frac{\Gamma_j}{2\pi(E_C - E_j)^2 + \Gamma_j^2/4} \qquad 3.3$$

The capture (calorimetric) energy E_C encloses the total de-excitation energy that is detached in the form of electrons and x-rays emitted during the process. Numerical calculation of Equation (3.3) can be performed using the ^{163}Dy atomic parameters, E_j, Γ_j and β_i^2, given in Table (3.1). The levels of electrons that can be potentially captured are fully occupied and therefore each n_j is chosen to be 1. The exchange and overlap corrections are neglected by choosing $B_j \sim 1$.

(Table 3.1) *^{163}Dy parameters: energy levels of the captured electrons E_j, their widths Γ_j, and electrons squared wave functions at the origin β_i^2 relative to $\beta_{M_1}^2$*[66, 67].

Level	E_j[eV]	Γ_j[eV]	$\beta_j^2/\beta_{M_1}^2$
M1	2047	13.2	1
M2	1842	6.0	0.0526
N1	414.2	5.4	0.2329
N2	333.5	5.3	0.0119
O1	49.9	3.0	0.0345
O2	26.3	3.0	0.0015

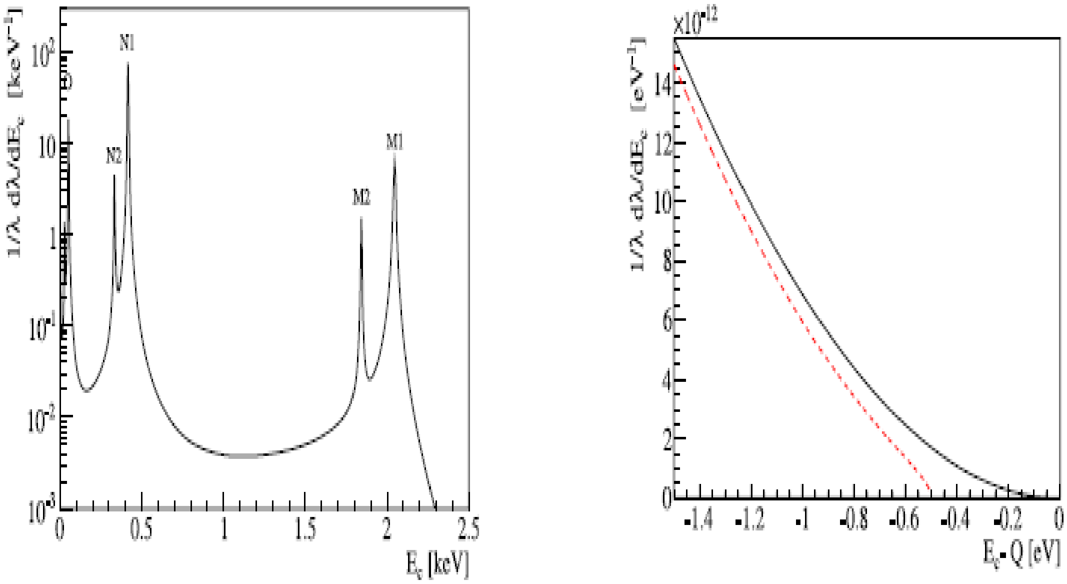

(FIG.3.1) *Calculated de-excitation energy spectrum of the ^{163}Ho EC decay with Q = 2.5 keV neglecting detector resolution effects (left). A zoom into the endpoint of the spectrum (right).The solid black line represents a zero mass neutrino and the dashed red line indicates a 0.5 eV neutrino mass* [67].

Figure (3.1) shows the expected calorimetric de-excitation energy spectrum. The heights of the peaks in the energy spectrum are weakly dependent on the neutrino mass. In general, an EC decay count rate is poor near the end point region but in the case of Holmium isotope, the count rate in that region is highly enhanced by the M peaks. So far, only four calorimetric absorption measurements are reported in the literature:

- A cryogenic microcalorimeter and sandwiched source were used by Genoa group [68].
- A Si(Li) detector and an implanted source were used by the ISOLDE collaboration [69],
- A proportional counter and organo-metallic gas were used by Hartman and Neumann [70],
- Ho implanted gold film and MMCs (Magnetic Metallic Calorimeters) were used by the ECHO project [96].

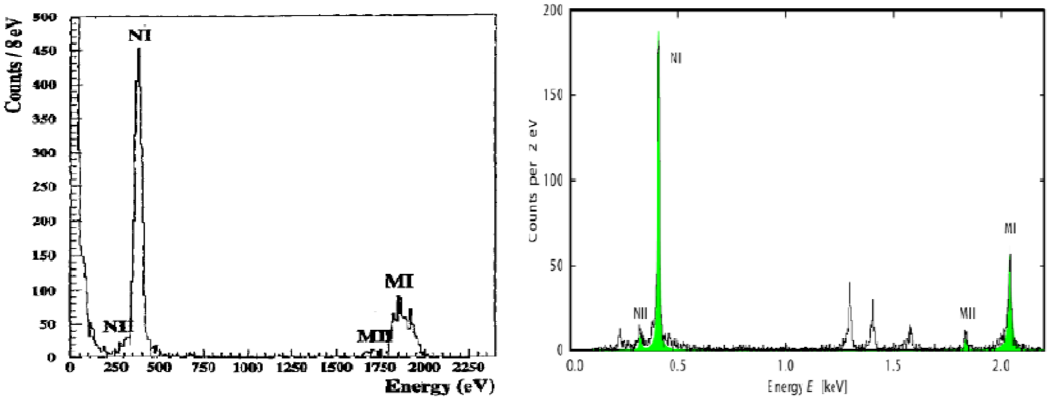

(FIG.3.2) Measured ^{163}*Ho calorimetric spectrum: from Genoa group (left) [68] and test results of ECHO project (right) [96]*

The results from the Genoa group, Figure (3.2) left, were able to resolve NI, NII, MI and MII lines that were not previously resolved by other solid state detectors. The right side of the figure represents the test results from the ECHO project, where the unlabeled peaks in the figure are due to an impurity ^{144}Pm. To date, none of the Ho-experiments have reached the sensitivity required for the end point measurement of an electron neutrino mass. The aforementioned calorimetric experiments were mainly limited by either the energy resolution of the detectors and/or the statistics.

3.3 Feasibility of a Ho Experiment

In recent years, there has been huge improvement in microcalorimetric technology and its applications. Today's cryogenic microcalorimeters technology can be used in a large scale experiment with excellent energy and time resolutions. Therefore, regardless of the limitations of the earlier calorimetric experiments and related uncertainties, cryogenic microcalorimeters are the detector of choice for a Ho experiment. Full implementation of the Ho experiment is challenging, and it may take enormous efforts and time. Members of the MARE collaboration have outlined a roadmap for the Ho-experiment with the following four key steps necessary to demonstrate the feasibility of a Ho-experiment [66]:

- Accurate determination of the Q-value of the decay
- ^{163}Ho production
- Detector Performance
- Theoretical Uncertainties

3.3.1 The Q-Value of the Decay

The sensitivity of the ^{163}Ho neutrino mass experiment strongly depends on the Q-value of the decay. The smaller Q-value means M peaks are in closer proximity to the end point energy, and better the statistical sensitivity. As the Q-value increases, the gap between the M peaks and the end point energy enlarges, resulting in deteriorated experimental sensitivity. Previously determined Q-values relay on the capture ratios, which are affected by large uncertainties due to errors in the theoretical atomic physics factor and the correlation with the neutrino mass. Therefore, the experimentally determined Q-values found in literature span from 2.2 to 2.8 keV [62, 63]. This alone alters the achievable neutrino mass sensitivity by more than a factor of three. An accurate measurement of Q-value is necessary for better estimated sensitivity of a calorimetric Ho-experiment. A calorimetric end point measurement is the most straightforward approach to determine an accurate Q-value of Ho EC decay. Any possible Q-value between 2.2 to 2.8 keV can be measured with accuracy better than 20eV by using a single microcalorimeter with about $5x10^5$ counts. The required energy resolution of the microcalorimeter used in Q-value measurement is about 10 eV, which is an easily achievable limit. If the count rate remains less than 100 counts per second, then the measured Q-value is almost unchanged by the detector pile-up, and thus the total statistics can be converted directly to total time. A most recent Q value obtained from a prototype microcalorimeter is 2.80 ± 0.08 KeV [96].

3.3.2 ^{163}Ho Production

^{163}Ho is not available directly from nature and large scale production of high purity Ho isotope is required for neutrino mass experiments. A reliable production of ^{163}Ho with negligible radioactive contaminants requires dedicated resources. There are at least three different methods that are the most appealing for the production of the ^{163}Ho isotope as required by the neutrino mass experiments [66]:

- Neutron activation in nuclear reactor of ^{162} Er
- Alpha –particle bombardment of ^{165} Ho target
- Gamma –particle bombardment of ^{165} Ho target

Identifying the best method of production of ^{163}Ho is one of the milestones for the Ho experiment. This requires a series of tests followed by a variety of purification processes so that the actual ^{163}Ho produced is free from any radioactive impurities. The production of ^{163}Ho using the neutron activation of 38 % ^{162}Er enriched sample of erbium oxide has been conformed [91]. The irradiated sample was preserved for one month to get rid of short-lived radioactivity. After verifying the absence of both short and long-lived radioactive contaminations, the sample was dissolved in a hydrochloric acid solution and then deposited onto the absorber of a TES microcalorimeter. Analysis of the observed spectrum verified the presence of ^{163}Ho. Figure 3.3 shows the measured calorimetric spectrum, showing the structures of the EC decay of ^{163}Ho with few atypical features [108].The presence of ^{163}Ho in the solution was also confirmed at the University of Milano-Bicocca using Inductively Coupled Plasma Mass Spectrometry [66].A large scale production, purification, and testing are being done at the 1 MW Portuguese Research Reactor (RPI). The reactor is at the nuclear and Technological Institute in Lisbon and it has estimated production capacity of about 3kBq/mg (^{162}Er) per week [91].

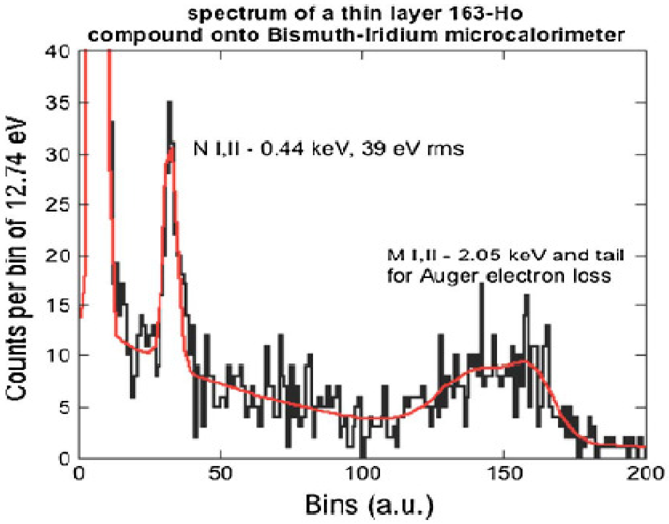

(FIG.3.3)*Observed calorimetric EC decay ^{163}Ho spectrum [91]*

3.3.3 Detector Performance

Working principle of cryogenic microcalorimeters is presented in Chapter two. Energy resolution, rise time of events, decay time, and read-out electronics must be considered carefully in designing a microcalorimeter for the application of neutrino mass experiments. The rise time is determined by the thermal conductivity of the absorber and the thermal connection between the thermometer and the absorber. In case of metallic and superconducting absorbers, the rise time is negligibly small as compared to the decay time of the detector but usually limited by the response time of the read out electronics.

High energy resolution of the detector is required for better accuracy of the neutrino mass experiments. The energy resolution of a microcalorimeter is determined by the heat capacitance C of the detector, working temperature T, and the sensitivity α of the thermometer used (refer equation 2.59). A sensitive thermometer, low working temperature, and an absorber with low heat capacitance at working temperature are basic requirements for the construction of a microcalorimeter. The construction and optimization of TES detector with Ho embedded absorber is under investigation.

The pulses pile-up is perhaps the most important issue in neutrino mass experiments and they can be resolved or minimized by suitable choice of absorber materials. Based on their nature, pile-up events can be divided into two categories, resolvable and irresolvable. If the time difference between two successive events is less than rise time of the first one, then both events appear as a single event with high energy. The resulting energy spectrum is known as unresolved pileup spectrum and acts as a strong background component. The sensitivity of the neutrino mass experiment is significantly affected by the background generated by the unresolved double pulses. Our group, the astrophysics group at the University of Miami, is also involved in research to develop analysis algorithms to identify and eliminate such events. Since event's rise time is directly related to the fraction of unresolved pile-up events, it is critical that the detector must be designed with the shortest possible rise time. On the other hand, resolved pileup events are associated with the decay time constant of the detector. If the time interval between any two consecutive events is shorter than the time constant of the detector, the second event occurs while the detector is still recording the energy of the first event (or during it's way back to the starting temperature after absorbing energy of the first event). In such case, the second pulse is riding on the tail of the first one and the pile-up can be easily determined. Since the starting temperature of the second pulse is higher than that of the previous one, there is a variation in the amplitude of any two pulses generated by identical events (or detector's non-linearity). Therefore, such events must be discarded, which increases the dead time (percentage of time during which the detector is not functioning) and degrades the energy resolution of the detector. Therefore a faster detector (with very short time constant) is highly desirable to process large count rates that can be handled without worsening the achievable energy resolution. The effective time constant of the TES microcalorimeter can be reduced by more than a factor of 100 using negative electrothermal feedback (Section 2.4). It is important to note that there are wide variations in time intervals between any two successive decay events. Therefore there is always a probability of pile-up even when a very fast detector is used.

Our research is particularly focused on the investigation of the properties of the ^{163}Ho imbedded metallic absorber for the application of the Ho-neutrino mass experiment. The most desirable properties of source embedded absorbers can be quantified as:

- Potential to embed holmium isotope
- Very high conductivity or diffusivity at working temperature
- Good stopping power to absorb the decay energy in the limited volume of the absorber
- Sufficiently low heat capacity at the working temperature after the ^{163}Ho source is embedded
- Efficiency and reproducibility in fabrication (as 10^3-10^4 detector are necessary)

In standard theoretical derivation of energy resolution of a microcalorimeter, it is assumed that the absorber and the thermometer are point elements at uniform temperature, and their combined heat capacity is C. In practice they cannot simultaneously achieve uniform temperature because of the finite size and internal diffusivity of the absorber. As a consequence there is variation in the observed pulse shapes depending on the position of the event's interaction. Resulting detector response is distorted, which ultimately leads to the degradation of energy resolution. This effect was investigated using numerical simulations of the coupled differential equations describing the thermal diffusion in the microcalorimeter [72]. The results showed that the higher the diffusivity the lower the degradation due to position dependence, and that a nonzero diffusion time in an absorber imposes an upper limit on the absorber size. Another diffusion simulation of a typical design, in which a small TES is placed at the center of the pixel with a large in-plane absorber around the TES, demonstrated that minimal degradation of the energy resolution can be achieved by choosing absorber material with diffusivity higher than $10^5 \mu m^2/\mu s$ $(RRR > 6)$[73]. This simulation analysis also showed that energy resolution of 2eV can be achieved with a high-quality gold films absorber $(RRR > 6)$. Thermal properties of gold films have already been investigated and energy resolution of about 2eV has been achieved using a gold film absorber in a TES microcalorimeter [74]. The measured RRR of a 2 micron electroplated Au film was(~ 56), whereas the bulk value of RRR for pure gold is 92. AT the working temperature of TES detector (0.1K), gold film possesses volumetric capacity $C = 7.14\, JK^{-1}m^{-3}$and thermal conductivity $\mathrm{G} = 5.72\,\mathrm{WK^{-1}m^{-1}}$. High conductivity and corresponding short rise time of a gold absorber is especially favorable for the Ho-experiment to minimize the pulse pileup effect.

Different techniques for embedding the source in the detector are currently being explored. The focus of this thesis work is the investigation of the thermal properties of Yttrium silicide sample (chapter 5) and Ho^{+} & Er^{+} implanted gold films (chapter 6) as potential candidates for source-embedded absorbers for a holmium experiment.

3.3.4 Theoretical Uncertainties

The final requirement for the Mare-Ho experiment is to investigate the theoretical uncertainties. One of the major limitations of Ho experiments comes from the large uncertainty on atomic physics factors. Despite the many experiments, the atomic and nuclear details of the ^{163}Ho EC decay are still not well understood and hence affected by unknowns. Those unknowns are ultimately reflected in uncertainties in the expected shape of the calorimetric spectrums. Furthermore, the theoretical energy spectra obtained from Equation (4.3) is still questionable and seems incomplete [75, 76]. Despite the fact that the expected shape of the total absorption spectrum is not well established, the neutrino mass is expected to be determined by the shape of the energy distribution near the end point. Therefore, additional effects that potentially alter the ^{163}Ho EC spectrum must be investigated and implemented to obtain an unambiguously complete expected spectrum. The position of peaks in the EC spectrum can be used for the precession measurement of many parameters. Therefore, as suggested by Rujula and Lusignoli [65], a high energy resolution and high statistics calorimetric measurement of the total absorption spectrum is an urgent necessity for neutrino mass measurement that use the end point of Ho EC decays.

3.4 Statistical Sensitivity a ^{163} Ho Experiment

The statistical sensitivity of a holmium experiment has been worked out in details by Galeazzi et al. [66]. Here I summarize their results. A frequentist Monte Carlo code has been developed to approximate the statistical sensitivity of neutrino mass experiments carried out with microcalorimeters [77]. In the Monte Carlo analysis, many Ho EC decay energy spectra, characterized by the same experimental set up, are simulated and then fitted with real ones. The distribution of the acquired m_v^2 parameters is then used to obtain statistical sensitivity. The total statistics N_{ev}, the detector energy resolution ΔE_{FWHM}, the fraction of unresolved pile-up events f_{pp}, and the background b are considered as the Monte Carlo parameters characterizing the experimental set up. These input parameters can be expressed in terms of the actual parameters describing a real experiment such as

$$N_{ev} = N_{det} A_\beta t_m = T A_\beta \text{ and } f_{pp} \approx A_\beta \tau_R, \qquad 3.4$$

where N_{det} is the number of detectors, A_β is the Ho EC decay activity of a single detector, t_m is the running time of experiment, $T = N_{det} A_\beta t_m$ is the exposure, and τ_R is the pile-up resolving time. The simulated energy spectrum $S(E)$, which is expected to be measured by virtual experiments, can be expressed as [66]

$$S(E) = \frac{N_{ev}}{\lambda_{EC}} \int_0^{2(Q-m_i)} dE_1 \, R(E-E_1) \times$$

$$\left[\frac{d\lambda_{EC}}{dE_C}(E_1) + \frac{f_{pp}}{\lambda_{EC}} \int_0^{E_1} d\,E_2 \frac{d\lambda_{EC}}{dE_C}(E_2) . \frac{d\lambda_{EC}}{dE_C}(E_1 - E_2)\right] \qquad 3.5$$

where $\frac{d\lambda_{EC}}{dE_C}$ is expressed in Equation (3.3), the background b(E) is assumed to be zero and the response function R(E) is assumed to be a Gaussian function of the following form

$$R(E) = \frac{1}{\sigma\sqrt{2\pi}} e^{-\frac{E^2}{2\sigma^2}} \qquad 3.6$$

The standard deviation of mean is given by $\sigma = \Delta E_{FWHM}/2.35$. The simulated spectra are fitted using Equation (3.5) and free parameters N_{ev}, f_{pp}, Q-value, and m_v^2. The results of the Monte Carlo simulation carried out for different Q-values (2200 eV, 2400 eV, 2600 eV, and 2800eV) are shortly discussed in the next few paragraphs.

Figure (3.4) shows the dependence of the neutrino mass sensitivity as a function of total statistics N_{ev}. The symbol represents the statistical sensitivity as estimated by a Monte Carlo approach, while the fine dash line corresponds to a $N^{-\frac{1}{4}}$ functional dependence of the sensitivity as determined by analytic formulation derived on Nucciotti et al. [77]. There is significant improvement of the sensitivity with the increase in statistics. For a typical set of parameters—an energy resolution $\Delta E_{FWHM} = 1\ eV$, pile of fraction $f_{pp} = 10^{-5}$, and Q-value 2.6 keV—the total statistics required to achieve a sub-electron volt sensitivity on neutrino mass (i.e. $m_v \approx 0.2\ eV$) is the order of 10^{14}.

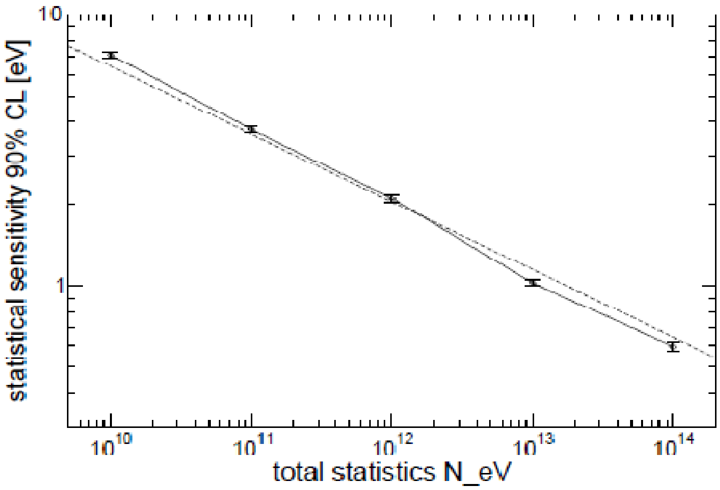

(FIG.3.4) *Neutrino mass statistical sensitivity as a function of total statistics* $\Delta E_{FWHM} = 1\ eV, f_{pp} = 10^{-5}$, Q *= 2.6 eV* [66]

The dependence of the neutrino mass statistical sensitivity on the energy resolution ΔE_{FWHM} and the fraction of pile-up events f_{pp} are individually shown in Figure (3.5). Clearly, the sensitivity degrades rapidly with an increase of f_{pp}, while the detector energy resolution has weak impact on the sensitivity of a Ho EC decay neutrino experiment.

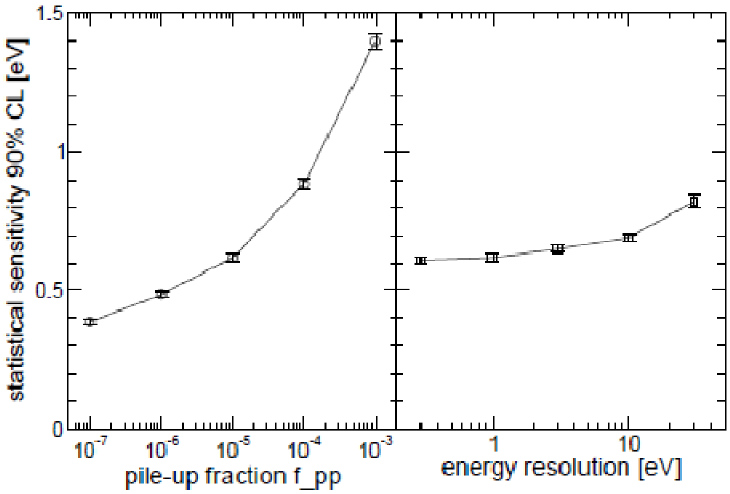

(FIG.3.5) *The impact of energy resolution and the pile-up fraction on statistical sensitivity of a Ho experiment.* $N_{ev} = 10^{14}, \Delta E_{FWHM} = 1\ eV,$ Q *= 2.6 eV (left) and* $N_{ev} = 10^{14}, f_{pp} = 10^{-5}, = 2.6\ keV$ *(right)* [66]

In Figure (3.6) the statistical sensitivity is plotted against the single detector activity A_β for four different Q-values and two different sets of detector parameters. The lower panel corresponds to the Configuration I with detector parameters $\Delta E_{FWHM} = 1\ eV, \tau_R = 1\ \mu s, T = 10^5$ detector×year. In this configuration, the experimental exposure of 10^5 could be achieved by operating 10^4 detector arrays for 10 years. The upper panel represents the more challenging configuration II, in which the energy and time resolution are improved by factor of 10 to obtain experimental exposures that are a factor of 10 higher. The most important pieces of information obtained from Figure (3.6) are:

1) For a given energy resolution ΔE, pile-up resolving time τ_R, and experimental exposure T, the statistical sensitivity significantly improves with the increase in single detector activity. In fact the increase in detector activity not only increases the experimental statistics but also the unresolved fraction of pile-up events. The resulting effect, however, is an enhancement in the statistical sensitivity of the experiment. About 2×10^{11} nuclei of ^{163}Ho isotope can produce activity of about one decay/sec [66].
2) The statistical sensitivity improves with the decrease in the Q-value but the increase in sensitivity is not consistent with the decrease in Q-value. The best sensitivity is obtained for Q = 2200 eV and it decreases drastically when Q increases to 2400 eV. A further increase in Q-value slightly degrades the sensitivity so that the three higher Q-value results are not considerably different. The pile-up spectrum for Ho EC decay is shown in Figure (3.7). The inconsistency in sensitivity can be explained by the irregular shape of the pile-up spectrum in the interval Q= 2000 eV to Q = 2600 eV.

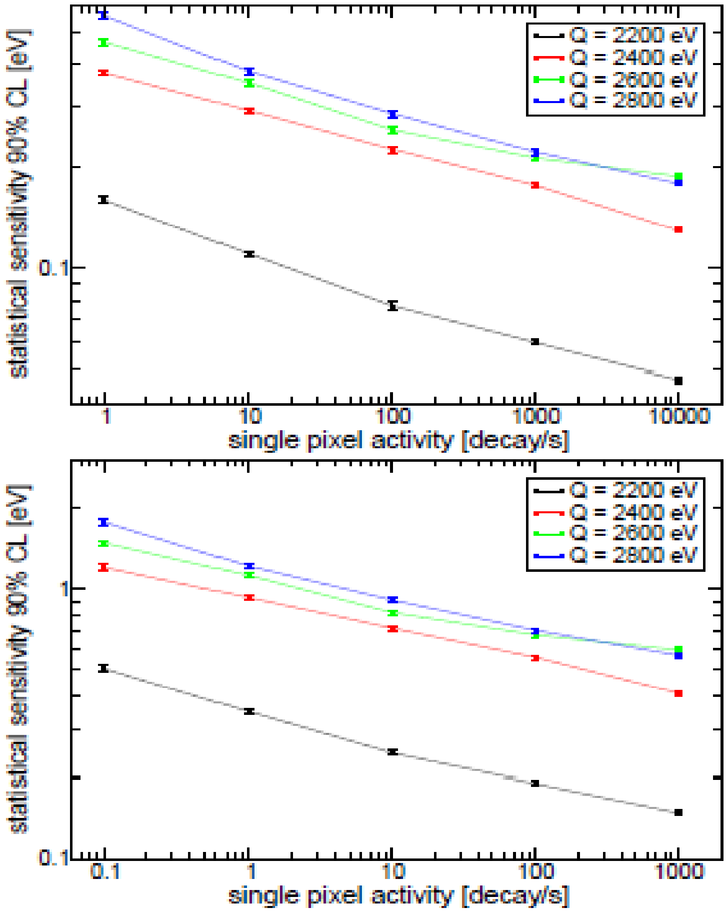

(FIG.3.6) *Statistical sensitivity as a function of single detector activity* A_β *for various Q-values. Detector parameters are:* $\Delta E_{FWHM} = 0.3\ eV, \tau_R = 0.1\ \mu s,$ *T =* 10^6 *detector×year (top) and* $\Delta E_{FWHM} = 1\ eV, \tau_R = 1\ \mu s,$ *T =* 10^5 *detector×year (bottom)* [66]

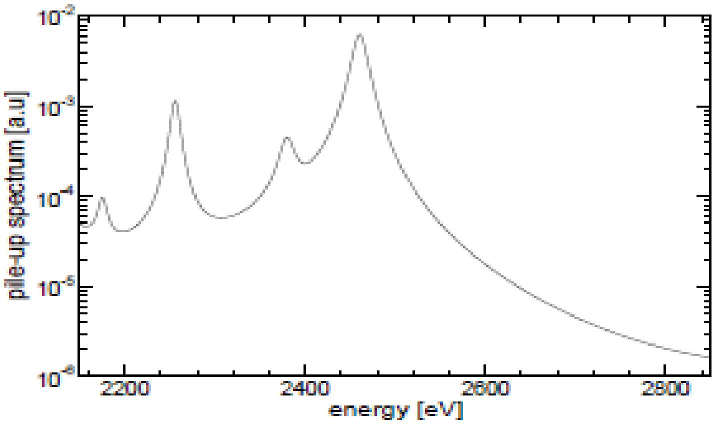

(FIG.3.7) *Expected pile-up spectrum for Ho EC decay when Q-value changes from 2200 eV to 2800 eV* [66]

Table (3.2) shows the calculated experimental exposure necessary to achieve neutrino mass statistical sensitivities of 0.2, 0.1, and 0.05 eV for the highest and lowest possible Q-values. Configuration I corresponds to the detector parameters $\Delta E_{FWHM} = 1\ eV, \tau_R = 1\ \mu s$, $A_\beta = 1000$ Hz, while configuration II refers to parameters $\Delta E_{FWHM} = 0.3\ eV, \tau_R = 0.1\ \mu s$ and $A_\beta = 10000$ Hz.

(Table 3.2) *The targeted sensitivities and required experimental exposure for two extreme Q-values and different sets of detector parameters: Configuration I refers the set of parameters* $\Delta E_{FWHM} = 1\ eV, \tau_R = 1\ \mu s$, *and* $A_\beta = 10^5$, *while the Configuration II refers* $\Delta E_{FWHM} = 0.3\ eV, \tau_R = 0.1\ \mu s$ *and* $A_\beta = 10000H$ [66].

Q	target sensitivity	exposure time [detector × years]	
(keV)	(eV)	Conf. I	Conf. II
2.2	0.2	2.6×10^4	3.3×10^3
2.2	0.1	4.1×10^5	8.8×10^4
2.2	0.05	6.6×10^6	7.7×10^5
2.8	0.2	6.5×10^6	6.3×10^5
2.8	0.1	1.0×10^8	1.0×10^7
2.8	0.05	1.7×10^9	1.6×10^8

In conclusion, the ^{163}Ho neutrino mass experiment is undeniably challenging but achievable. The potential of such an experiment is still under investigation.

Chapter 4

Experimental Setup

4.1 Cryostat Considerations

The low temperature measurements necessary as part of this thesis where performed using an Adiabatic Demagnetization Refrigerator (ADR) at the University of Miami. The technical details of the refrigerator are described in [78], here I summarize the critical aspects and working principle of the refrigerator.

The possibility of magnetic cooling was proposed independently in 1926 by P. Debye [80] and in 1927 by W.F. Giauque [81]. A few years later, in 1933, the magnetic disorder entropy of electronic magnetic moments (electron spins) of paramagnetic salts was applied to lower temperatures well below 1K [82, 83]. This process is known as adiabatic demagnetization of paramagnetic salts. Temperatures in the mK range can be achieved by using adiabatic demagnetization refrigerators. In an adiabatic demagnetization refrigerator, the cold plate, which is thermally attached to a paramagnetic salt pill, can be cooled below 50 mK, well matched to the working temperature of TES microcalorimeters, which is around 100 mK. The schematic and the actual top view of the ADR at the University of Miami are shown in Figure (4.1). It consists of three main parts: a cold plate attached to a salt pill filled with the paramagnetic salt FAA (ferric ammonium alum, $Fe_2\ (SO_4)_3.\ (NH_4)_2SO_4.\ 24H_2O$), a strong superconducting magnet, and a mechanical heat switch between the cold plate and the helium bath. The superconducting magnet produces magnetic field of well above 4T within the bore of the magnet when maximum magnetic current of 9.55A is applied [78].

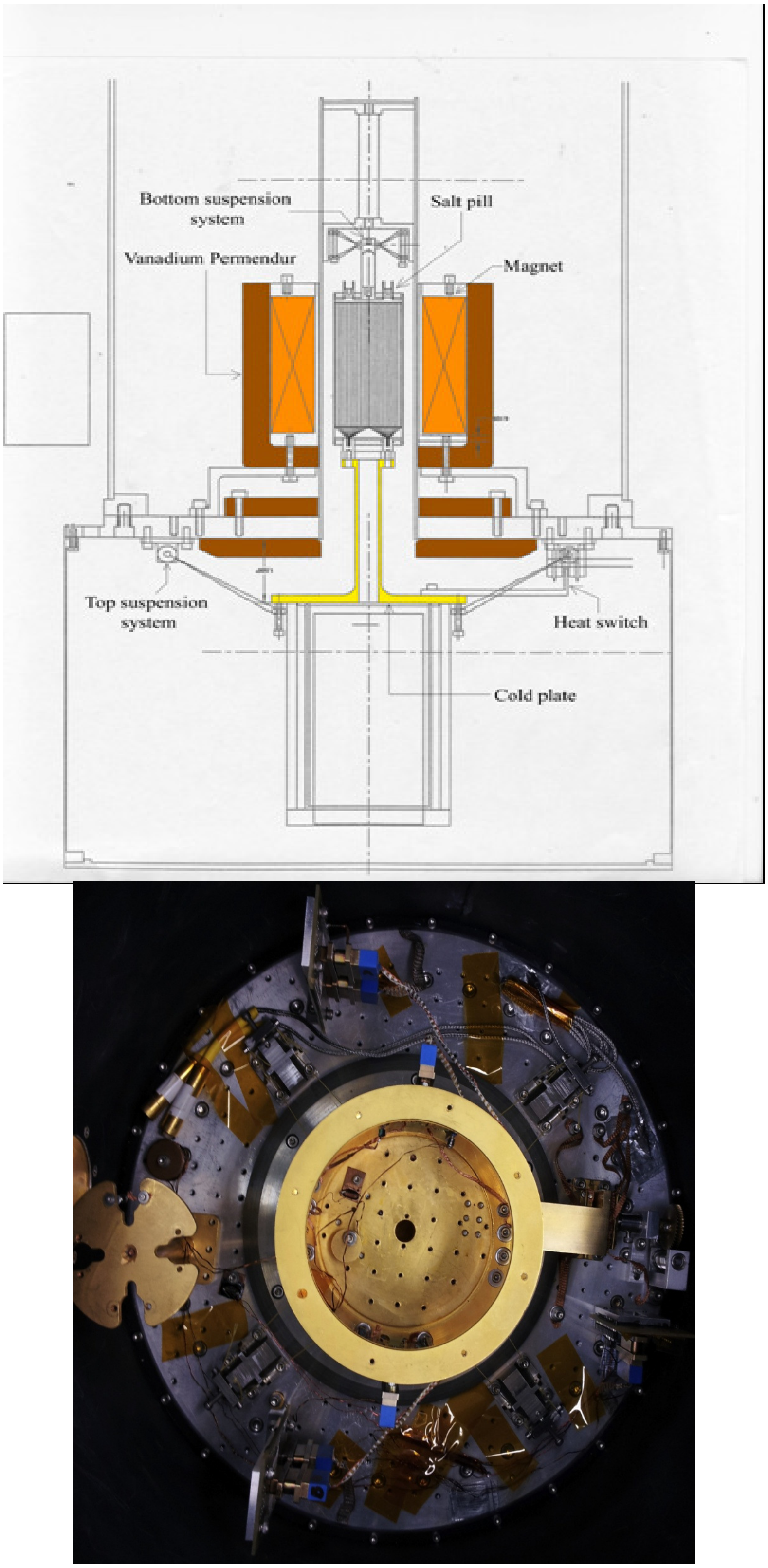

(FIG.4.1) *A schematic (top) and actual top view (bottom) of the ADR at the University of Miami*

The salt pill is suspended within the bore of the superconducting magnet by using two (top and bottom) suspension systems with Kevlar wires. The temperature of the cold plate is monitored by a neutron transmutation doped (NTD) germanium thermistor. A proportional integral derivative (PID) temperature control system connected to the thermometer and a heater is used to control the temperature to within 10 micro-K peak-to-peak. The superconducting magnet is shielded by Vanadium Permendur to minimize the magnetic field outside the bore of the magnet. The magnetic field at the cold plate is nearly zero during the time of measurments, when magnetic current is well below 0.1A [78]. The outer shell of the refrigerator acts as a Faraday cage to minimize noise and all electrical connections are in and out of the refrigerator are filtered through RF filters. The system is thermally insulated through a single high vacuum below 10^{-6}millitorr (mtorr). The refrigerator runs on cryogen liquids, with shields at 77K and 4.2K, using liquid nitrogen and liquid helium (^{4}He), respectively. During operations, the liquid helium stage, which works as heat bath for the ADR operations, is decreased below 2K by pumping on the liquid helium (which removes the most energetic helium molecules). Once the cold plate reaches below the constant super fluid helium bath temperature, the solenoid current is slowly ramped up (0.01A/s) from 0 to 9.5 A. This increases the magnetic field in the bore of the superconducting magnet, where the salt pill is, from almost 0 (residual field) to 4 tesla (T). During this magnetization, the electronic spins of the paramagnetic salt align with the magnetic field. The corresponding heat of magnetization in the cold-plate/salt-pill system is dumped to the heat bath through the heat switch, keeping the process (ideally) isothermal. (In reality, the thermal conductance to the heat bath is not sufficient to keep the process isothermal, and temperature of the cold-plate/salt/pill system first increases to about 3.5 K, then slowly decreases toward the heat bath temperature). When the thermal equilibrium of the system is reached, the heat switch is opened and then magnetic field in the magnet is slowly ramped down to zero. During this adiabatic demagnetization, alignment of the spins is broken and heat energy is absorbed from the atoms in the isolated system. As a consequence, the temperature of the salt pill and cold plate is lowered below 50 mK. The cooling mechanism of an ADR can be well understood from the analysis of the entropy change of the paramagnetic salt pill.

4.2 Cooling Mechanism of an Adiabatic Demagnetization Refrigerator (ADR)

Ions in a paramagnetic salt are regarded as distinguishable particles (occupying definite sites in the crystal lattice) obeying Boltzmann statistics. The expression for a paramagnetic salt is given by [84].

$$\frac{S(T,B)}{nR} = \ln\left[\frac{\sinh((2J+1)\,x/2)}{\sinh\left(\frac{x}{2}\right)}\right] + \frac{x}{2}\coth\left(\frac{x}{2}\right) - \frac{(2J+1)x}{2}\coth\left(\frac{(2J+1)x}{2}\right) \qquad 4.1$$

where $x = g\mu_B B/k_B T$ (g = Land$\acute{e}$ factor, μ_B = the Bohr magnetron, B = applied magnetic field, and k_B= the Boltzmann's constant) and J = the total angular momentum quantum number. For FAA salt, g is isotropic and close to 2, whereas J is 5/2 .The entropy S is therefore, the function of B/T. The magnetic disorder entropy $S\ (B,T)$ of a paramagnetic salt dominates all other entropies such as phonons and conduction electrons entropy.

An ADR is an entropy pump and its cycle of operation can be understood with entropy diagram shown in Figure (4.2). First, the temperature of the salt-pill is lowered below 2K using a super fluid helium bath. The point $U\ (B_i, T_i)$ in the Figure represents entropy of the system at the precooled stage with no external magnetic field. At this stage, dipoles moments (spins) are completely disordered and entropy contribution approaches constant value, $S = nR(2J + 1) = nR \ln 6$.The magnetic field is then slowly increased up to 4T with the salt-pill in contact with the He-bath. This isothermal magnetization takes place from $U\ (B_i, T_i)$ to $V\ (B', T_i)$ on the graph, during which magnetic work is performed on the salt. This work is converted into the heat energy, which is absorbed by the He-bath.

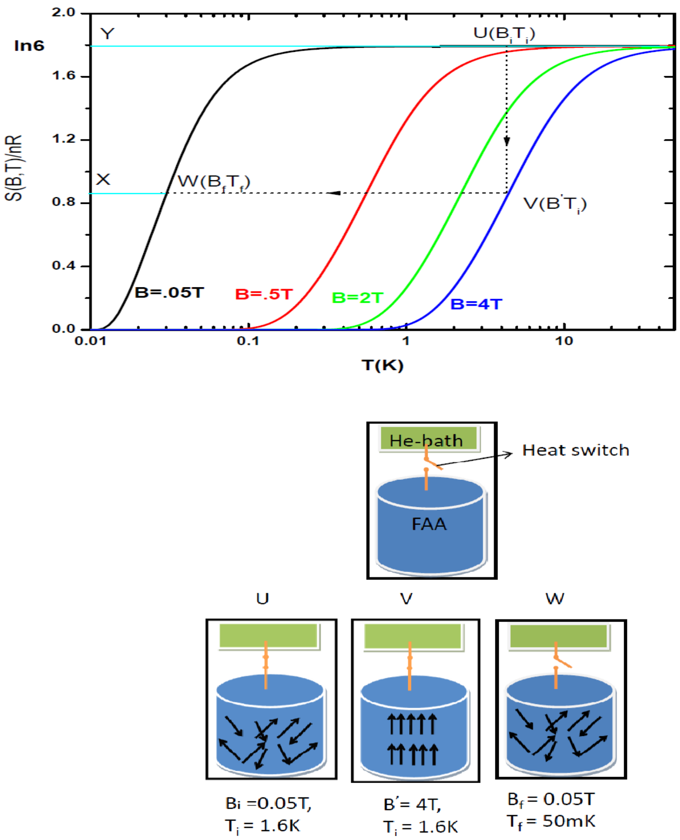

(FIG.4.2) *Predicted ADR cycle (top) and the orientation of dipoles in the salt pill (bottom)*

At $V\ (B', T_i)$, the salt pill is kept isolated by disconnecting the heat switch from the He-bath and then magnetic field is slowly reduced B' to B_f. This adiabatic demagnetization takes place from $V(B', T_i)$ to $W\ (B_f, T_f)$ on the graph. During this process, the overall entropy of the system remains constant; however, the lattice entropy is converted to the spin entropy. In other words, the dipoles absorb heat energy from the surrounding atom or molecules in order to break their alignment. As a consequence, the overall temperature of the salt pill and the cold plate is decreased to T_f. In this isentropic process, magnetic field is simply proportional to the temperature.

$$\frac{B^{'}}{T_i} = \frac{B_f}{T_f} \quad or\ T_f = \frac{B_f}{B^{'}} T_i \qquad 4.2$$

In principle, the precooled conditions of $T_i = 1.6K, B_f = B_i = .05T\ and\ B^{'} = 4T$ result in the final temperature T_f down to 20 mK. Once the lowest temperature is reached, the salt pill slowly warms up via the path $W\ (B_f, T_f)$ to $U\ (B_i, T_i)$ due to heat load or stray power of the ADR. The heat absorbed by the salt pill during the warming up process is represented by the area WXYU.

The system cannot be demagnetized to down to zero magnetic fields. As a result, the absolute zero temperature can never be achieved by the adiabatic demagnetization of paramagnetic salts. Below sufficiently low temperature T_c, the interactions between the neighboring dipoles are no longer negligible. At sufficiently low temperature, the mutual interactions between the dipoles tend to align them in same direction producing a small resultant magnetic field b and therefore, final temperature is modified as

$$T_f = \frac{\sqrt{B_f^2 + b^2}}{B^{'}} T_1 \qquad 4.3$$

The temperature T_c, below which the effect of the mutual interactions becomes significantly strong, is called the magnetic ordering temperature or transition temperature. At temperature $T \leq T_C$, the interaction energy $(\epsilon = \mu b)$ is comparable to the average thermal energy $k_B T$.

4.3 Determination of Stray Power of an ADR

The observation time of an ADR after each cooling is determined by stray power, which is the result of heat leak to the cold plate. In order to provide better insulation, the salt pill and cold plate are suspended with Kevlar wires by using two suspension systems , the pressure inside the ADR is kept below 10^{-6} torr, and the samples are connected via superconducting wires, which are heat sunk on the supercooled helium stage. At the working temperature, the heat radiation from the helium stage and the conduction via connecting wires are the main sources of stray power.

The UM ADR, originally constructed in 2004, was refurbished in 2010. The refurbishment included following changes

- We build two cylindrical covers made of gold plated copper. Once the samples are installed on the cold plate, these removable covers were attached to the cold plate. The samples were therefore well shielded from radiation leaks from 4.2K plate. This change does not affect the hold time of the ADR, however, it significantly reduce any stray power going directly on the devices tested.
- Electrical connections between the liquid helium stage and the cold plate were originally made through RADIUS manganin wires. This would generate significant residual stray power to the cold plate and, due to the fragility of the wire insulation, was often subject to shorts at low temperature. The manganin

wires have been replaced by superconducting ribbon cable. The cable was connected via 25-pins MDM connectors installed on the liquid helium plate and the new copper cover on the cold plate.

After refurbishment of the ADR, the heat load or stray power was measured at the base temperature 100 mK and compared to original measurements made in 2004 before the manganin wires were installed. A high resistance (50 kΩ at room temperatures) heater was installed on the cold plate and heat load or stray power was determined by two different methods.

Method 1: The temperature of the cold plate was kept constant by applying regulating current and multiple known powers were dissipated on the cold plate by applying dc current through the high resistance. The measured power was plotted against the rate of change of the regulating (magnet) current. The stray power was determined from the linear fit of the plot. The plot of power vs. rate of change of current at constant temperature of 100 mK is shown in Figure (4.3). From the plot, the stray power (-A) is 0.923

Method 2: Different known powers were dissipated on the cold plate without regulating temperature of the cold plate and the rate of change of temperature of the cold plate was plotted against the measured applied power. The plot of power vs. rate of change of temperature is shown in Figure (4.4). Linear fit of the plot gives the stray power (-A) at temperature 100mK is 1.01 microwatts.

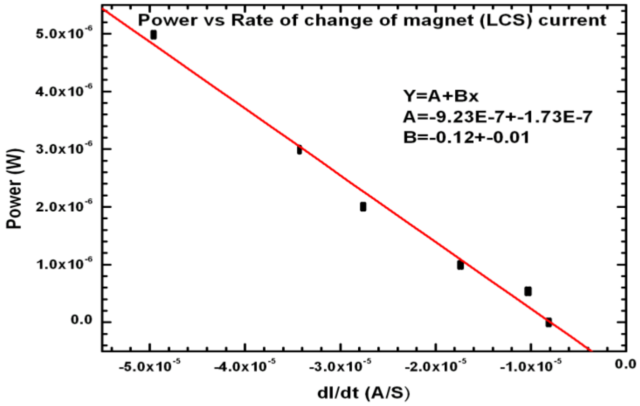

(FIG.4.3) *At constant temperature 100mK, the applied power is plotted as a function of rate of change of current. The linear fit of the plot gives the stray power,* $-A = 0.92\ \mu W$.

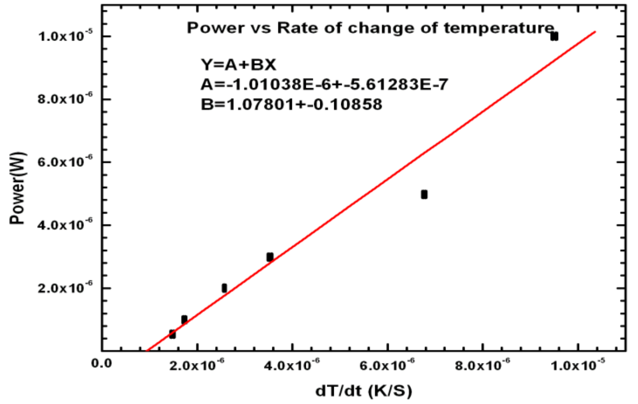

(FIG.4.4) *At base temperature 100mK, the applied power is plated as a function of rate of change of temperature The linear fit of the plot gives the stray power,* $-A = 1.01\ \mu W$.

The original heat load of the ADR at 100mK was 1.25 μW [78]. By refurbishing the ADR, we were able reduce the heat load below 1 μW. The most importantly, we never have had short circuit problem after the refurbishment of the ADR.

4.4 Fabrication of Thin Film

The thin film manufacturing facility at the University of Miami, Physics Department, consists of a self-built dust free clean room kept under positive pressure. One of the cornerstones pieces of equipments in this laboratory is a multisource Radio Frequency

(RF) magnetron sputtering system (from AJA international, Model: ORION 4 HV with load lock) capable of depositing thin film of metals, semiconductors, and insulating materials. A spinner system, UV source (Oriel), mask alignment fixer, MEI1204 hybrid wedge bonder and timer for UV exposure are other key equipments in our clean room.

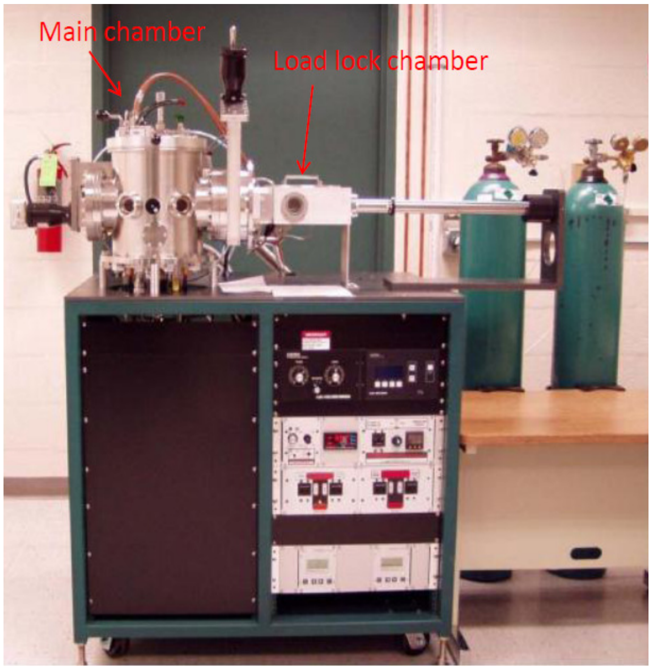

(FIG.4.5) *Magnetron sputtering system at the University of Miami*

The sputtering system is equipped with two sources (Al and Ir) and a load-lock chamber capable of accommodating up to six inches substrates. The main chamber has an everyday base pressure nearly 10^{-8} torr whereas the load-lock chamber can reach pressure nearly 10^{-7} torr in few minutes. The substrate can be heated to 800^{o}C and the thin film material can be deposited in a combinatorial or layered fashion.

4.5 X-Ray Diffractometer

We used the Philips X'pert X-Ray Diffractometer to analyze the crystal structure of the thin films. The technical details of the Diffractometer are described in [100], here I summarize the important aspects and working principle of the Diffractometer.

The Diffractometer consists of three main parts, an X-ray source (tube), a sample holder, and a detector, as shown in Figure 4.6.They are arranged in such a way that the distance between the X-ray focal spot and the sample is equal to the distance between the sample and the detector. This typical arrangement is also referred to as the Bragg-Brentano geometry. The mechanical assembly that makes up the sample holder, the detector arm and associated gearing is known as goniometer.

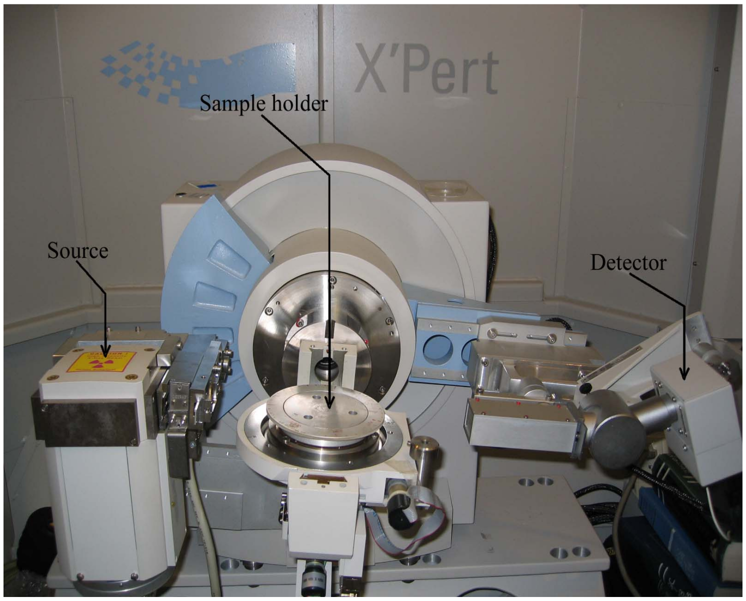

(**FIG.4.6**) *Phillips X'pert Diffractometer at the University of Miami*

In the X-ray tube, a tungsten filament and a Cu-target are used to produce X-rays which mainly consist of the most prominent $K_\alpha(K_{\alpha1}, K_{\alpha2})$ lines of wavelength 1.54 Å and K_β lines of wavelength 1.39Å.The unwanted K_β radiation is eliminated using Ni filter. The voltage and current of the X-ray tube can be adjusted between $15kV/5mA$ to $40kV/55\,mA$ and the X-ray beam can be set up with either a point focus or line focus. The reflected radiation is counted by the detector, which is a Xe-filled proportional counter capable of rotating nearly 140^o. The desired sample is placed at the center of the sample holder with appropriate choice of a slit, depending on the sample size. The sample on the stage is then aligned with half beam splitting process using $40kV/15mA$ and Fe filter. Once the alignment is completed a detector filter is placed, the Fe filter is replaced with β-filter (Ni filter) and tube voltage and current is adjusted as per the requirements (commonly 40kV/30mA).Successive short term scans of $2\theta - \omega, \Phi, \psi$ and ω scans are made repeatedly until all the parameters are optimized giving maximum intensity of a peak for each scans.

The crystal peaks are determined by using and $2\theta - \omega$ scans. This is the most common mode of scan in which the incident angle θ is changed by rotating the sample holder and the detector is rotated with twice the angular speed of the sample holder. The detector is therefore always kept at the 2θ position with reference to the direction of incident beam. This one dimensional scan with constant $(\omega - \theta)$, allows us to observe all possible reflections of all planes that are parallel to the focused (h k l) planes. The ω-scan, also known as the rocking curve, provides the information about the magnitude of spread in the orientation of the crystallites and the presence of mosaic. In this scan, the detector is oriented at a fixed Bragg's angle and the incident angle is varied by few degrees around the θ angle that gives the reflection peak. In particular, a wide rocking curve is expected for a large spread in the crystal orientation, while more than one peak at the same angle of incidence θ indicates the presence of mosaic.

Chapter 5

Properties of Yttrium Silicide (Y_5Si_3)

5.1 Motivation

The potential of a ^{163} Ho electron capture (EC) decay neutrino mass experiment is still under investigation but the basic requirements of such experiment have been identified (Chapter 3). One of the major requirements for such experiments is to design a high resolution detector with a source embedded in the absorber of a microcalorimeter. Different combinations of geometries, TES, and absorber materials have been used, with various degree of success, for the fabrication of TES microcalorimeters [89]. A possible candidate to use directly as absorber is yttrium silicide (Y_5Si_3). However the thermal properties of Y_5Si_3 have not been measured in the working temperature range of TES microcalorimeters. The investigation of yttrium silicide is motivated by the need of using rare earths compounds in the extraction of the radioactive ^{163}Ho after fabrication [66].

We have measured the heat capacity and electrical resistivity of a Y_5Si_3 sample in the temperature range 80-300 mK using a bolometric technique [90].

5.2 Sample Preparation

A 2 g sample of Y_5Si_3 was prepared at the University of Genoa, Italy, by arc melting the elements under a pure Ar atmosphere and on a water-cooled copper hearth (99.95 wt.% purity yttrium, and >99.999 wt.% purity silicon); the surface of the rare earth was mechanically cleaned before weighing and synthesis. The arc-melted button was remelted three times, turning them over each time, to achieve good homogenization. It was then wrapped into an outgassed Ta foil, sealed under vacuum into silica ampoules, and annealed at 1000 °C – 1 day. The final total weight loss was 0.35 %.

The heat capacity and electrical resistivity were measured in the Adiabatic Demagnetization Refrigerator described in Chapter 4. Two bolometers were constructed to measure the thermal conductivity and heat capacity of the bulk Yttrium Silicide (Y_5Si_3) sample. Each bolometer consisted of a silicon piece (1cm×1cm, 400μm thick) suspended on a silicon stem glued on a copper plate, which was then heat sunk to the cold plate of the refrigerator. Each was equipped with a Ruthenium oxide thermometer (RX-102A-BR from LakeShore) and a heater (thick film chip resistor ERJ-2GE J102 from Panasonic). The dimensions of the thermometer and heater are (1.45×1.27×0.65) mm^3 and (1×0.5×.35) mm^3 respectively. The electrical connections for thermometers and heaters were provided by $20\ \mu m$ diameter Al wires ultrasonically bonded. A small Y_5Si_3 sample ($1.02\ g$) was glued on one bolometer, while the other bolometer was used for reference. For simplicity we name the sample as follows:

- Sample-0: Si-plate equipped with heater and thermometer
- Sample- A: Si-plate equipped with heater, thermometer and the small piece of Y_5Si_3 metal

The schematic view of the two bolometers constructed for the measurement of heat capacity of Y_5Si_3 is shown in Figure (5.1), while side view of the bolometers is shown in Figure 5.2. Sample-0 was used to measure the contribution from the heater, thermometer, and the Si-plate, while the combined heat capacity of the heater, thermometer, silicon plate, and the Y_5Si_3 sample was measured using sample-A. The difference of the two provides the value of the Y_5Si_3 sample.

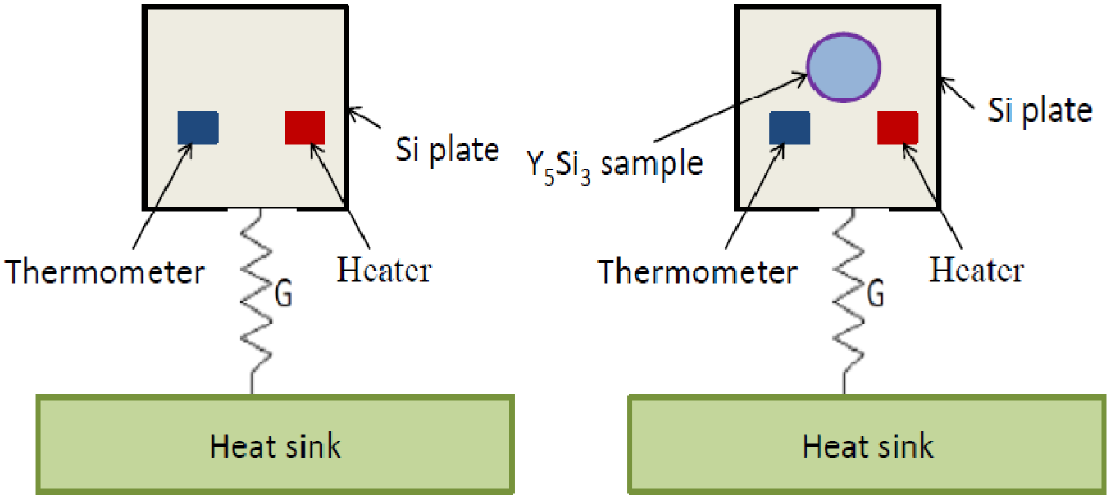

(FIG.5.1) *Two bolometers: sample-0 (left) consists of a Si-plate equipped with heater and thermometer, while sample-A (right) consists of a Si-plate, heater, thermometer, and a small piece of* Y_5Si_3 *metal.*

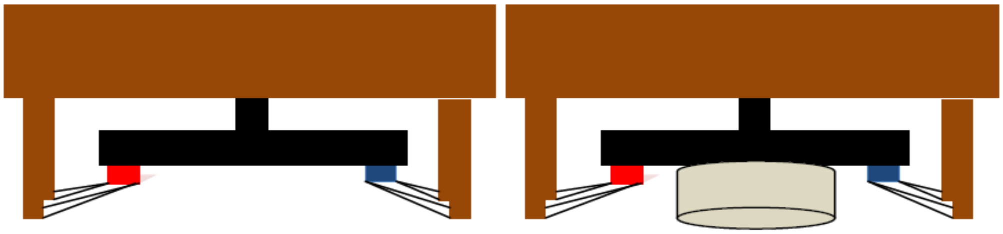

(FIG.5.2) *The side view of bolometers constructed to measure heat capacity of* Y_5Si_3 *sample*

We use a lock-in amplifier and four wire measurements to determine the resistance of the thermometer and heater at various temperatures. Each thermometer on the sample was locally calibrated using the commercially calibrated germanium resistance thermometer (GRT) installed on the cold plate of the ADR. The magnetic field at the sample site, due to the ADR operation was well below 1 Gauss [78].

5.3 Thermal Conductance Measurements

The procedure used for the heat capacity measurement is the same described in Galeazzi et al. (2010) [91]. For each temperature, the first step was measuring the thermal conductance between the samples and the cold plate. The temperature of the cold plate was kept constant while a known power was dissipated on the bolometers by supplying a fixed dc current to the sample heater. Multiple values of power were chosen such that the rise in temperature of the samples remained within a few mK.

I have already presented the Microcalorimeter and bolometer theory in Section (3.2). In our calculation, it is assumed that there is no input power other than the Joule power of the heater, P (T) = i^2R (T). For this measurement, the current, and hence the Joule power of the thermometer was kept very small and did not affect the temperature of the bolometer. Using Equation (2.13) we obtained

$$G_0 = \frac{(\beta + 1)P(T)}{\left(T_H^{\beta+1} - T_C^{\beta+1}\right)}, \tag{5.1}$$

where T_H is the temperature of the sample while the heater is turned on, T_C is the temperature of the cold plate (equal to the temperature of the sample when the heater is turned off), and we assumed that the thermal conductance has the form $G = G_0 T^\beta$. To determine the heat capacity of each sample we applied small known current to the heater to raise the sample temperature by a few mK and waited for the sample to reach thermal equilibrium. We then turned off the heater and waited until the sample returned to the base temperature. Multiple powers were deposited on the heater and the corresponding constant dc current was recorded for each heating. The power dissipated on the heater was calculated using the measured resistance of the heater and the measured current. Figure (5.3) shows the measured resistance of the heater on sample-A in the 80-700mK range. The difference in the measured resistance during ramping up and ramping down current is due to the temperature difference between the cold plate and the sample heater. The calibration and multiple heating of sample-A at the base temperature 150mK is shown in Figure (5.4), while the same plot converted into temperature is shown in Figure (5.5). Similar plot for sample-0 is shown in Figure (5.6).

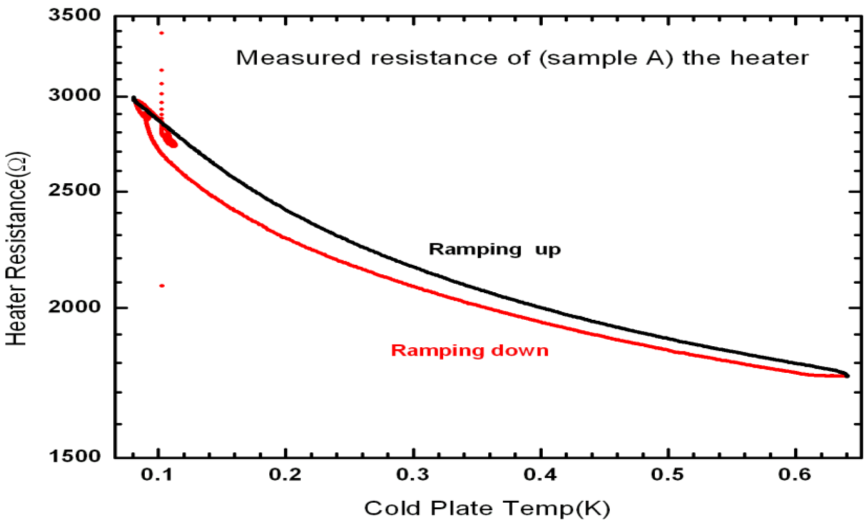

(FIG.5.3) *Heater resistance is plotted as function of cold plate temperature. The black and red curves, respectively, represent the measured heater resistance when current was ramping up and ramping down.*

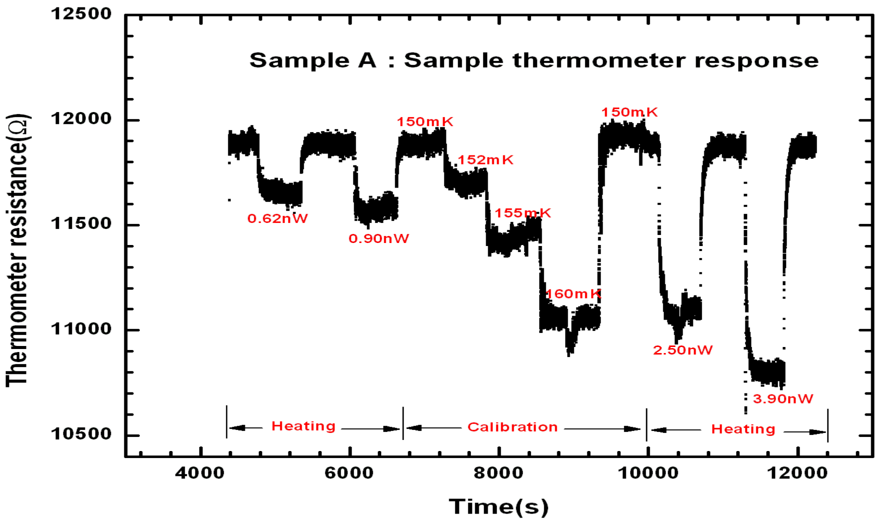

(FIG.5.4) *The response of the sample thermometer during heating and calibration is plotted as a function of time.*

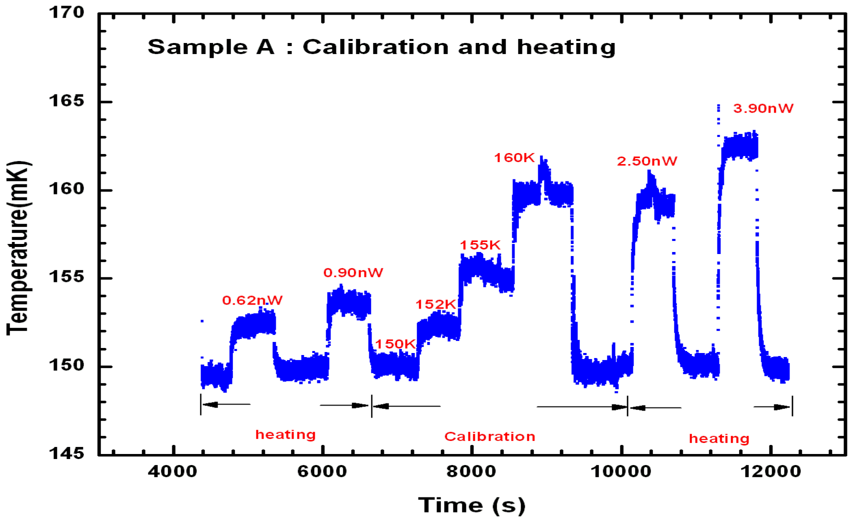

(FIG.5.5) *Sample-A thermometer response is converted in terms of temperature in K.*

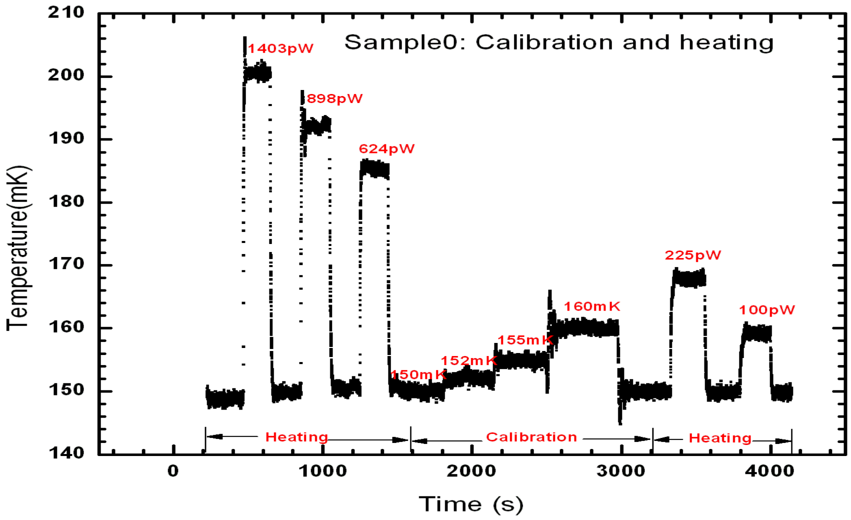

(FIG.5.6) *Sample-0 thermometer response showing heating and calibration*

We determined thermal conductance G in two different ways as described in Galeazzi et al. [99] and we verified the results. The measured values of G_0 and G at different base temperatures are presented in the table (5.1), where G_1 and G_2 are measured values of G from two different approaches.

(Table 5.1) *Measured thermal conductance between the sample and cold plate at different base temperatures*

Temp (mK)	G_0 (WK^{-4})	$G_1 = G_0T^{\beta}$ (WK^{-1})	$G_2 = {dP}/{dT}$ (WK^{-1})	G (Average) (WK^{-1})
80	1.4×10^{-4}	8.67×10^{-8}	8.67×10^{-8}	$(7.91\pm 0.76)\times10^{-8}$
90	1.13×10^{-4}	8.19×10^{-7}	1.02×10^{-7}	$(9.19\pm 1.0)\times10^{-8}$
100	10^{-4}	10^{-7}	1.24×10^{-7}	$(1.11\pm 0.11)\times10^{-7}$
120	8.02×10^{-5}	1.38×10^{-7}	1.52×10^{-7}	$(1.44\pm 0.07)\times10^{-7}$
150	8.78×10^{-5}	2.98×10^{-7}	3.17×10^{-7}	$(3.07\pm 0.01)\times10^{-7}$
200	8.37×10^{-5}	6.70×10^{-7}	7.26×10^{-7}	$(6.98\pm 0.28)\times10^{-7}$
250	8.25×10^{-5}	$1.28\times10^{--6}$	$1.37\times10^{--6}$	$(1.32\pm 0.04)\times10^{-6}$
300	1.02×10^{-4}	$2.77\times10^{--6}$	$2.98\times10^{--6}$	$(2.87\pm 0.10)\times10^{-6}$

The measured thermal conductance (using two different approaches) was plotted as a function of temperature (Figure 5.7). Clearly, from the plot, the results from two methods closely agree with each other. Figure (5.8) shows average of the measured thermal conductance as a function of the cold plate temperature, which closely agreed with the power law fit. In the plot, the red curve is the power law ($G = G_0T^{\beta}$) fit. We also determined thermal conductance at each temperature from the plot of the power dissipated on the thermometer as a function of the temperature difference between cold state and hot state of the sample (ΔT). Figure (5.9) shows the plot of the power as function of ΔT for base temperature 150mK.The slope of the plot ($3.10\times10^{-7}WK^{-1}$) gives the thermal conductance at 150 mK, which agree with the directly calculated value presented on Table (5.1).

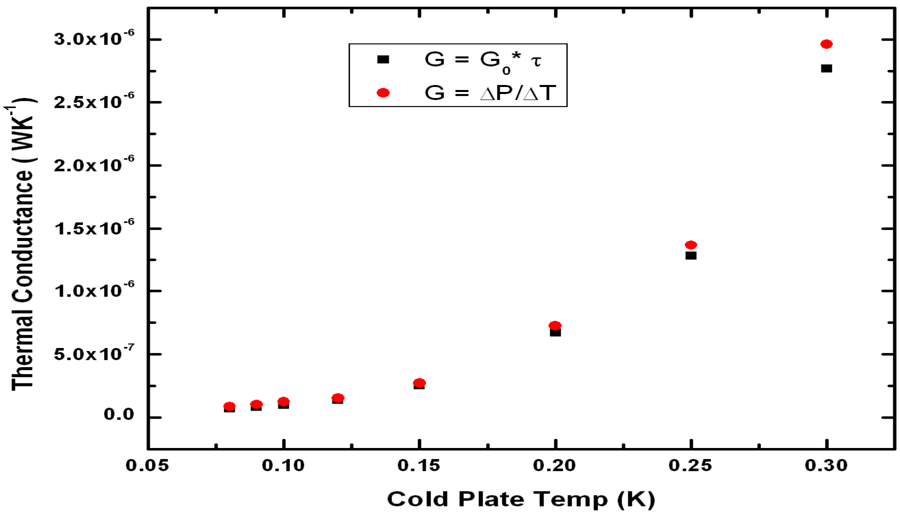

(FIG.5.7) *Measured thermal conductance (using two different methods) is plotted as a function of cold plate temperature (base temperature of the sample).*

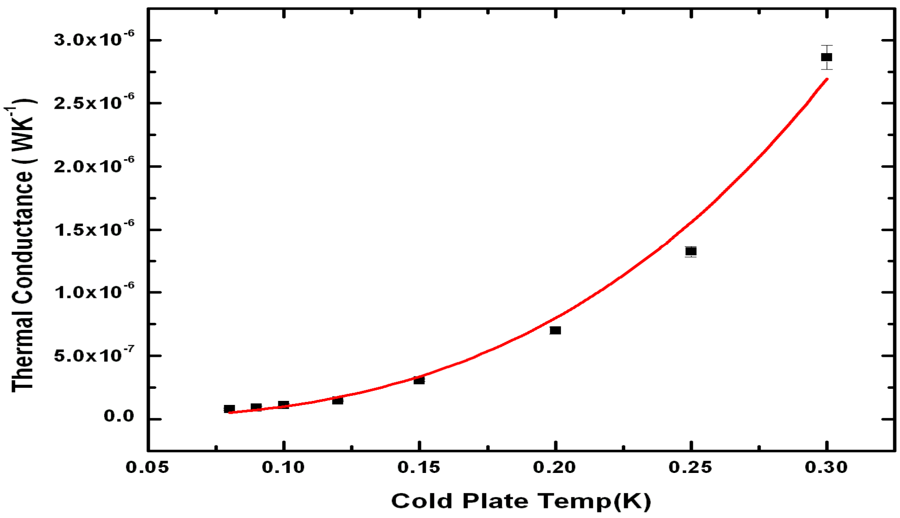

(FIG.5.8) *Average of the measured thermal conductance is plotted as a function of cold plate temperature. The red curve is the power low fit.*

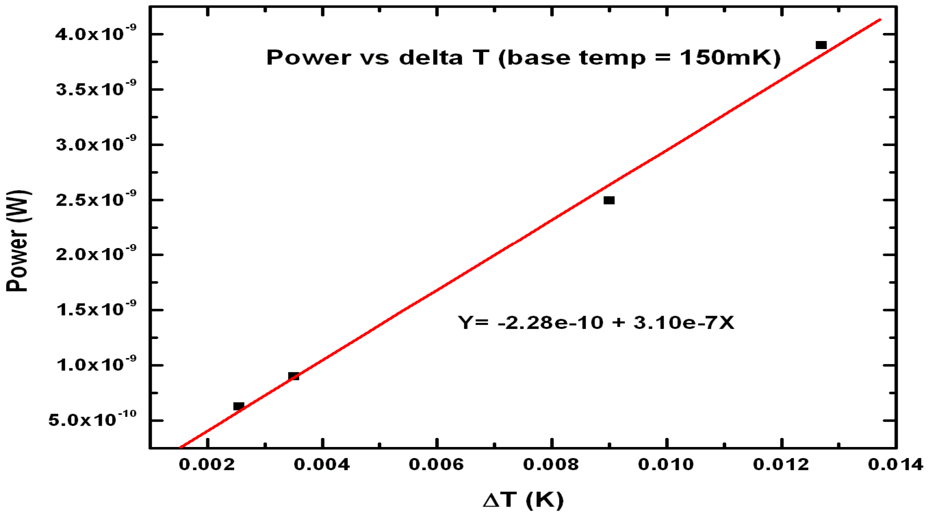

(FIG.5.9) *Power dissipated on the heater (at base temp 150mK) was plotted as a function of* ΔT*. From the linear fit of the plot the thermal conductance G is* $3.10\times10^{-7}\mathrm{WK}^{-1}$.

5.4 Heat Capacity Measurement

For the heat capacity measurement, we used the thermal conductance G and time constant τ of the relaxation. From the simple bolometer theory described in chapter 2 we expect that the relaxation of the samples follows an exponential decay curve of temperature vs. time with time constant $\tau = C/G$. We verified that, indeed, our samples follow such behavior and can be described with the simple theory (i.e., we do not need more complex bolometer theory). The time constant, τ — time required for the thermometer to return back to the initial temperature — was determined by fitting the exponential curve. The exponential fit for a typical relaxation at base temperature 150mK is shown in Figure (5.10). Figure 5.11 shows the time constant τ as a function of cold plate temperature. The measured data set closely agree with the inverse square law fit ($\tau \propto T^{-2}$) as expected. The blue line shows the fit of the plot.

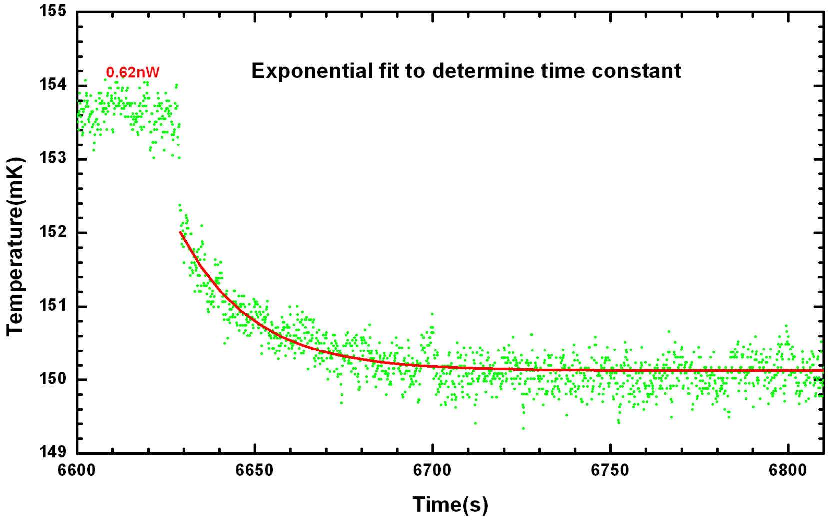

(FIG.5.10) *Exponential fit of a typical relaxation at base temperature 150mK*

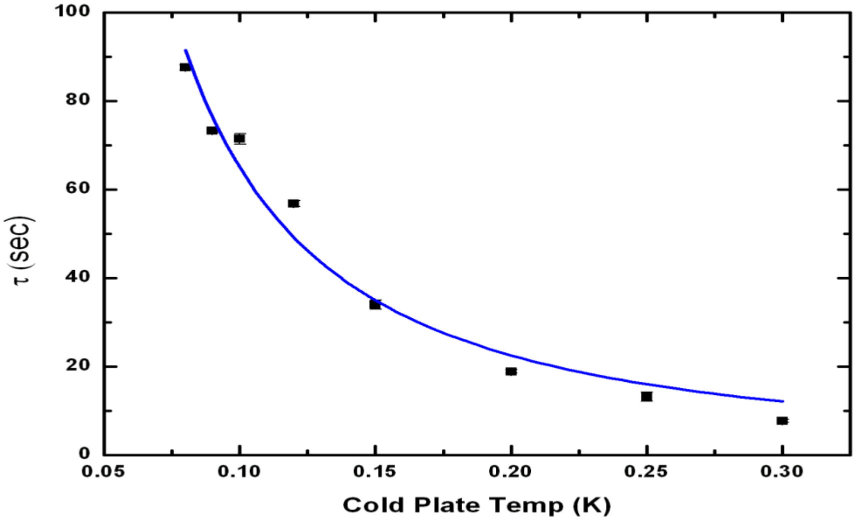

(FIG. 5.11) Time constant τ was plotted as a function of temperature. The blue line shows the inverse square fit of the plot.

The heat capacity of each sample at any given temperature was therefore determined using simple relation given in Equation (2.3)

$$C = G * \tau \qquad 5.2$$

For each sample, the heat capacity measurement was repeated with a different base temperature ranging from 80mK to 300mK. The measured values of heat capacity of both samples are shown in Figure (5.12). The black squared data set represents the heat capacity of sample A, while the red circles represent the heat capacity of sample-0. Clearly, the contribution from the heater, thermometer, and silicon plate is much smaller (~ factor of 100) than that of the Y_5Si_3 sample.

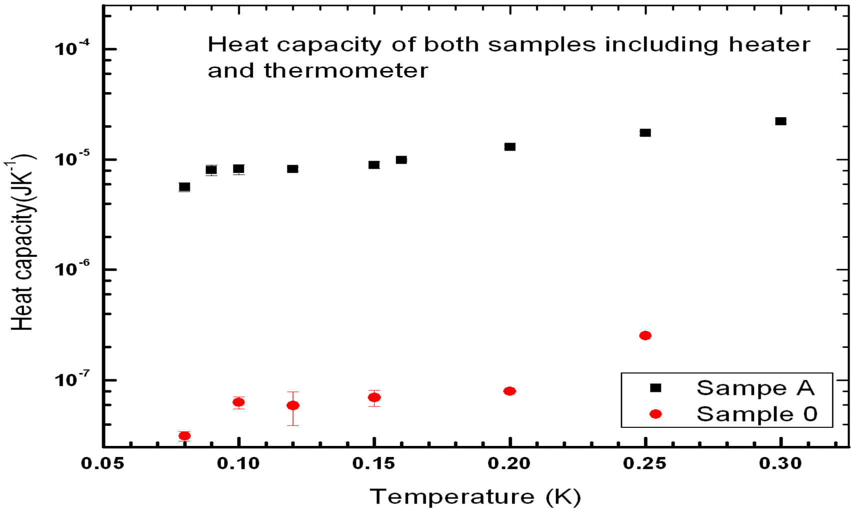

(FIG.5.12) *Measured heat capacity of sample-A (the black squared data set) and sample-0(the red circles) are plotted as a function of temperature.*

The heat capacity of the Y_5Si_3 sample was determined by subtracting the contribution of heater, thermometer, and silicon plate from the measured heat capacity of sample-A and the measured mass of the sample was used to determine the specific heat capacity of the Y_5Si_3. Figure (5.13) shows the measured specific heat capacity of the sample in the temperature range 90 to 300 mK.

The data follow quite a well a linear dependence of the specific heat capacity versus temperature. A fit assuming a linear dependence of the specific heat capacity on temperature, $c = \gamma T$, gives a best value for the linear coefficient of:

$$\gamma = (6.79 \pm 0.15) \times 10^{-5} J\ g^{-1}\ K^{-2}, \qquad 5.3$$

which corresponds to a specific heat capacitance at 100 mK of

$$c(0.1) = (6.79 \pm 0.15) \times 10^{-6} J\ g^{-1}\ K^{-1}. \qquad 5.4$$

The red line in the figure represents the linear fit to our data, while the blue line represents the specific heat capacity of pure gold, from the Handbook of Chemistry and Physics [92]. Gold was used as a reference in this work because is a typical material used in the fabrication of microcalorimeter absorbers.

Figure 5.14 shows the same data, plotted as heat capacity per unit volume. The linear fit to the data gives a best value for the linear coefficient of

$$\gamma = (2.96 \pm 0.07) \times 10^{-4} J\ cm^{-3}\ K^{-2}, \qquad 5.5$$

which represents the same result of Equation 5.4, divided by the density of Y_5Si_3.

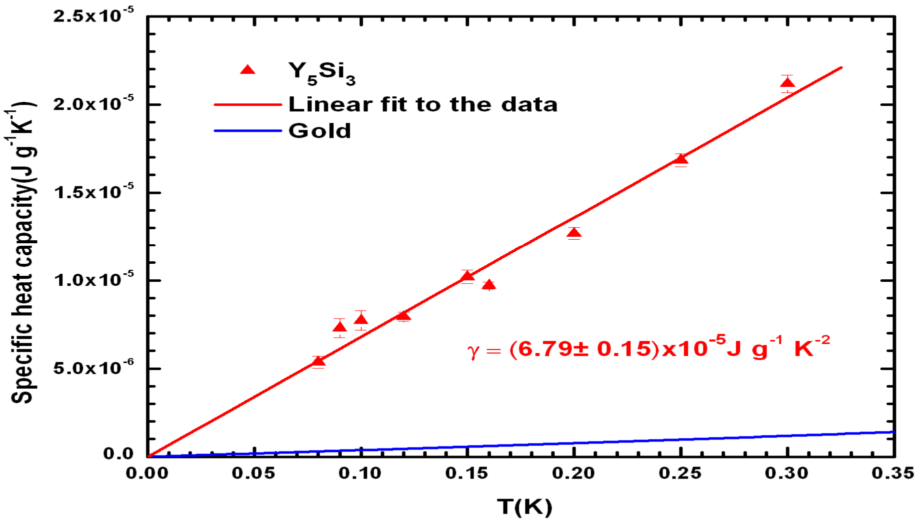

(FIG.5.13) *The measured specific heat of the Y_5Si_3 sample plotted as a function of temperature. The red line represents the linear fit of our data, whereas the blue line represents the heat capacity of gold.*

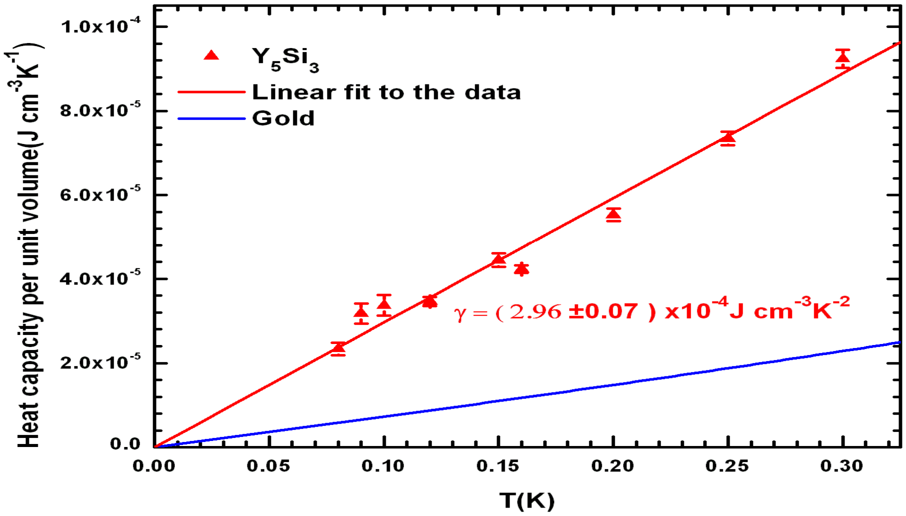

(FIG.5.14) *Measured heat capacity per unit volume of the sample plotted as a function of temperature. The red line represents the linear fit of the data whereas the blue line represents the heat capacity of gold.*

5.5 Measurement of Electrical Resistivity

We also measured the electrical resistivity of Y_5Si_3. A small cylindrical sample of cross sectional area 0.053 cm^2 and length 0.29 cm was heat sunk to the refrigerator cold plate and measured using 4-wires and a very small current (100 μA RMS). We verified, by changing the current value, that the power dissipated in the sample did not rise its temperature above that of the cold plate.

Figure (5.15) shows the measured resistivity of our Y_5Si_3 in the temperature range 0.09K to 300K in logarithmic scale, whereas Figure (5.16) shows the same plot in linear scale. The blue line in both represents the previously published resistivity of Y_5Si_3 in the temperature range 10K to 300K [93]. We assume that the difference in the resistivity of our data and previously published work is due to differences in the manufacturing process and level of impurities in the two samples. The resistivity at room temperature is

176.20 μΩ cm, while the resistivity at 4.2K is 88.60 μΩ cm for a Residual Resistance Ratio (RRR) of 1.99.

Our result indicates that the electrical resistivity of Y_5Si_3 is almost constant in the temperature range 90mK to 300mK. The electrical resistivity of the sample in that range of temperature is

$$\rho = (87.21 \pm 0.08) \times 10^{-8} \Omega\, m. \qquad 5.6$$

Using the Wiedemann–Franz law($\kappa/\sigma = L * T$), with a Lorenz number of $2.44 \times 10^{-8}\, W\, \Omega\, K^{-2}$[99], this corresponds to a thermal conductivity($\kappa = \kappa_0 T$) in the temperature range 90-300 mK with

$$\kappa_0 = (27.10 \pm 0.3) \times 10^{-3}\, W\, m^{-1}\, K^{-2}. \qquad 5.7$$

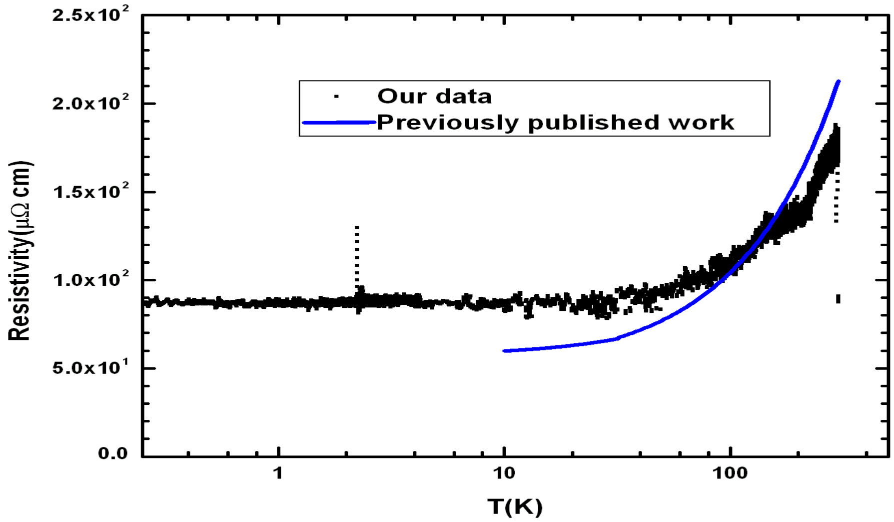

(FIG.5.15) *Measured electrical resistivity of the sample plotted as a function of temperature (in logarithmic scale). The blue line represents the resistivity from previously published work [93].*

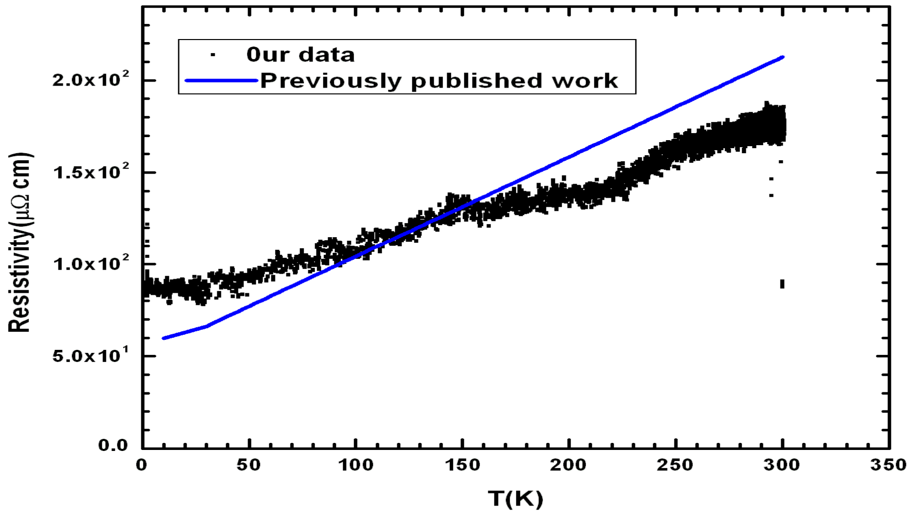

(FIG.5.16) *Measured electrical resistivity of the sample plotted as a function of temperature (in linear scale). The blue line represents the resistivity from the previously published work [93].*

5.6 Final Remarks

In conclusions, the heat capacity of Y_5Si_3 is about 5 times bigger than that of pure gold, which is typically used as absorber in cryogenic microcalorimeters. This implies that Y_5Si_3 probably cannot be used as sole absorber material for high performance detectors. However, it can be used in relatively small quantity (e.g., in "sandwich" structures), to fully embed a radioactive source in a microcalorimeter absorber. We also note that the efficiency of Y_5Si_3 in the extraction of the radioactive holmium has not yet been verified.

Chapter 6

Properties of Holmium-Implanted Gold Films

6.1 Motivation

Gold is currently one of the primary materials used as absorber in the fabrication of microcalorimeters and the possibility of implanting the holmium source (^{163}Ho) directly into gold films is under investigation. The variations in properties of gold films before and after the implantation were unknown in the working temperature region of cryogenic microcalorimeters. .

Holmium is paramagnetic in the temperature range 133K to 300K, antiferromagnetic in the temperature range 20K to 133K, and ferromagnetic in the temperature range 4.2K to 20K [98]. The result of low temperature (1.6 to 300K) measurements of the magnetic susceptibility of Holmium dissolved in gold (Au-HO 2.0 at % Ho) was presented by Murani [106]. In the paper, it is reported that Ho has a group of low-lying energy levels and non-magnetic ground state doublet and there is a magnetic triplet only 0.14K above the non-magnetic ground state duplet. The possibility of a hyperfine interaction in both of these multiplets is indicated by Bleaney [107]. If the gold films became magnetic due to the implantation, the heat capacity of the gold film might be dominated by the magnetic contribution. Depending on the concentration of Ho, there could be a risk of increasing heat capacity of the gold films even when concentration of Ho is relatively small. It is, therefore, critical to investigate heat capacity of gold films after implantation of Ho.

We investigated the thermal properties of implanted gold films in the working temperature of microcalorimeters. Gold samples were measured with and without implantation of various concentrations of (non-radioactive) holmium and erbium ions. Erbium is a byproduct of some of the ^{163}Ho production processes and would therefore be implanted together with holmium in a final experiment. In this chapter we report the results of the thermal

6.2. Sample Preparation

For the measurement, ten samples, each consisting of a 2 μm thick gold film deposited on 0.530 mm thick Si (100) substrate 1 cm × 1 cm, were prepared at the University of Genoa, Italy. The gold was deposited via e-beam deposition and a thin (60nm) iridium adhesion layer was used. The samples were also weighted with high accuracy before and after the deposition for an accurate determination of the gold mass. We notice that the samples were larger than the typical dimensions of microcalorimeters to facilitate the measurement and reduce the errors. However, the thickness used was comparable to what is necessary for a microcalorimeter absorber.

After deposition, nine of the samples were implanted with various concentrations of Ho^+ and Er^+ ions using the IST-ID ion implanter at the University of Lisbon/Center for Nuclear Physics. The tenth sample was kept without implant to use as reference. The IST-ID ion implanter has a chamber allowing the implantation of an area of 20cm×20cm in the temperature range of 77K to 1273K in a controlled way. The samples were characterized using particle induced x-ray emission (PIXE) line at the 2.5 MV Van de Graaff accelerator at the IST- ID with three bean lines, with all the relevant ion beam techniques available: RBS(Rutherford Backscattering Spectrometry), PIXE, NRA, Channeling, ERDA and NRB with proton and gamma. The ion concentration for each sample is shown in Table (6.1), where the ionization energy is in keV and concentration of ions is in cm^{-2}. The samples were implanted with different ion energies, to reach different depths within the film. The analysis indicated that: for the Er+ with implantation energy of 180 keV the penetration depth was 190.2 angstrom, Er+ with 250 keV 245.3 angstrom, Ho+ with 180 keV 186.0 angstrom and Ho+ with 250 keV 244.0 angstrom.

(Table 6.1) *Properties of the samples used (Ionization energies are in keV and ion concentrations are in* cm^{-2}*).*

	Implanted ion concentrations (cm^{-2})			
Samples	Ho^+(180KeV)	Ho^+(250KeV)	Er^+(180KeV)	Er^+(250KeV)
Au-I				
Au-II	$4x10^{15}$			
Au-IV	$4x10^{15}$		$9.6x10^{15}$	
Au-VI			$9.6x10^{15}$	
Au-1	$4x10^{15}$	$8x10^{15}$		
Au-2		$8x10^{15}$		
Au-3	$4x10^{15}$	$8x10^{15}$	$9.6x10^{15}$	$1.9x10^{16}$
Au-4		$8x10^{15}$		$1.9x10^{16}$
Au-5			$9.6x10^{15}$	$1.9x10^{16}$
Au-6				$1.9x10^{16}$

The holmium concentrations were chosen to be equivalent to a count rate of 1-10 counts/s (when radioactive material is used) in a typical microcalorimeter with sub-mm absorber. The erbium concentrations were determined by the process to manufacture the radioactive material [66] and correspond to a typical concentration of 30% radioactive holmium, 70% non-radioactive erbium. The samples were produced in two separate batches, labeled Au-I, Au-II, Au-IV, Au-VI, and Au-1, Au-2, Au-3, Au-4, Au-5, Au-6 respectively. Sample Au-I is the control sample without any implant. The heat capacity of each of the sample in the temperature range 70mK to 300mK was investigated at the University of Miami as part of this thesis**.**

6.3. Measurement of the Thermal Conductance

To study the thermal properties of each gold film, we built a bolometer for each sample. Figure (6.1) shows the actual (top) and schematic (bottom) views of a typical bolometer constructed for the investigation. Each bolometer was equipped with a Neutron Transmutation Doped (NTD) thermometer (bare Ge RTD thermometer from LakeShore Cryotronics) and a thin gold film heater. The dimensions and mass of each thermometer are ($2.555 \times 1.005 \times 0.526\ mm^3$) and ($5.7 \pm 0.1$) mg respectively.

Each heater consists of a 10 nanometer thick rectangular gold film with bonding pads deposited on about 0.05 mm thick Si (100) substrate. Overall, the mass of a single heater is about (0.1 ± 0.05) mg. The thermometer and heater were ultrasonically bonded using $25\ \mu m$ diameter Al bonding wires. The whole structure was suspended using the bonding wires, which also provided the weak thermal link to the heat sink for the bolometers. In addition to the ten samples, we built an identical bolometer using a $1\ cm\ \times 1\ cm$ bare silicon substrate (sample-0) to measure the heat capacity of heater, thermometer, and silicon. Figure 6.2 shows the side view of sample-0 and one of the gold film samples. The heat capacity of each implanted god film was then determined by subtracting the value of sample-0 from the sample one.

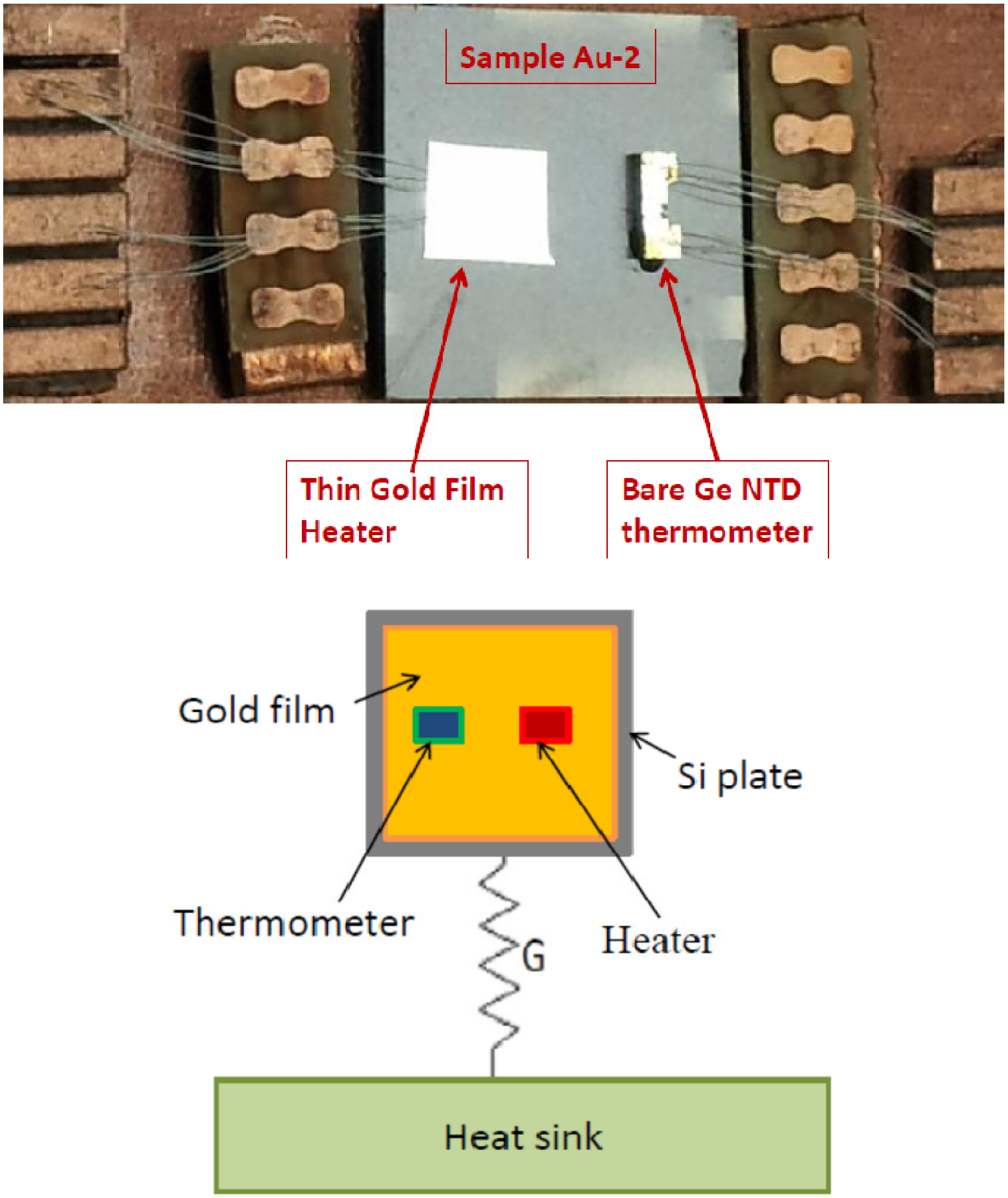

(FIG.6.1) *Actual bolometer with sample Au-2, thin gold film heater, and bare Ge NTD thermometer (top) and schematic view (bottom) of the bolometer constructed for measuring the heat capacities of holmium and erbium implanted gold films.*

As will be shown later in this chapter, the values of heat capacity to be measured in this experiment were significantly smaller than the ones measured in Chapter 5. For this reason, the whole measurement setup had to be updated. Either the thermometer and heater have significantly smaller heat capacity, or they would dominate that of gold. Moreover, in order to keep the bolometer time constant in a range easy to measure, the thermal conductance to the refrigerator cold plate had to be reduced accordingly, which is why the Si stem was removed and the thermal conductance was provided by the superconducting Al wires.

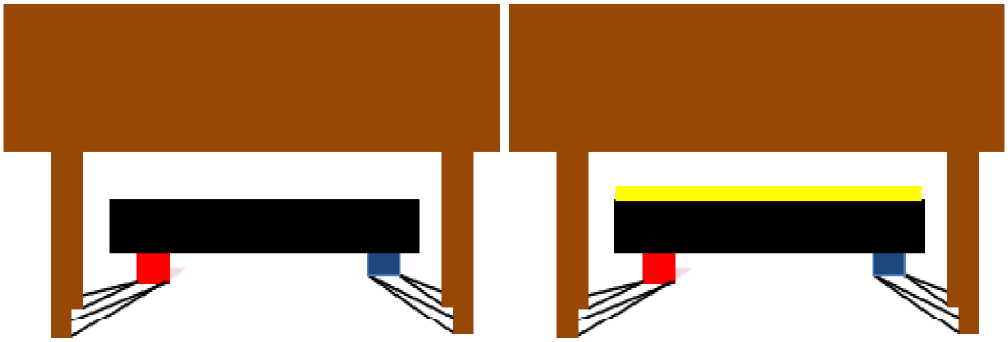

(FIG.6.2) *The side view of sample-0 (left) and one of the gold film samples (right).*

Each bolometer was installed on the cold plate of our ADR. As discussed before the heat capacity of the films may be dependent on the values of external magnetic fields. For this reason, the value of the magnetic field at the sample location due to the ADR magnet was kept below 1 Gauss. Moreover, we verified that there was no effect on the measured values due to changes in the magnet current. The measurement setup was similar to the one described in the previous chapter. We used a lock-in amplifier to determine the resistance of thermometer and heater at various temperatures ranging from 70 to 300 mK. Each NTD thermometer was locally calibrated using the commercially calibrated germanium resistance thermometer (GRT) installed on the cold plate of the ADR. Each sample was then heated with a small known current through the heater. The current was adjusted so that the raise in temperature of the samples was always kept within few MilliKelvins.

The heat capacity value for each sample was determined through simple bolometer theory in the linear approximation as describe in Section (2.3) and Chapter 5. The first step was the calculation of the thermal conductance to the cold plate. Multiple values of the input powers were used and the results fitted to obtain G_o and β for each base temperatureT_C. Figure (6.3) shows the thermometer data for a typical individual measurement (sample Au-2 at $T_C = 110\ mK$). The thermometer is first locally calibrated by changing the value of T_C, then T_C is kept constant at the base temperature while a small power is dissipated in the heater, rising the bolometer temperature. The plot on the top shows the raw resistance value of the thermometer as a function of time, while the plot on the bottom shows the data already converted to temperature using the local calibration. The heater current and the measured resistance of the heater were used to calculate the multiple powers deposited on the sample. The resistance of each heater was measured in the temperature range of interest. Figure (6.4) shows the measured resistance of a typical sample heater (for Au-2) in the temperature range 60-300mK.

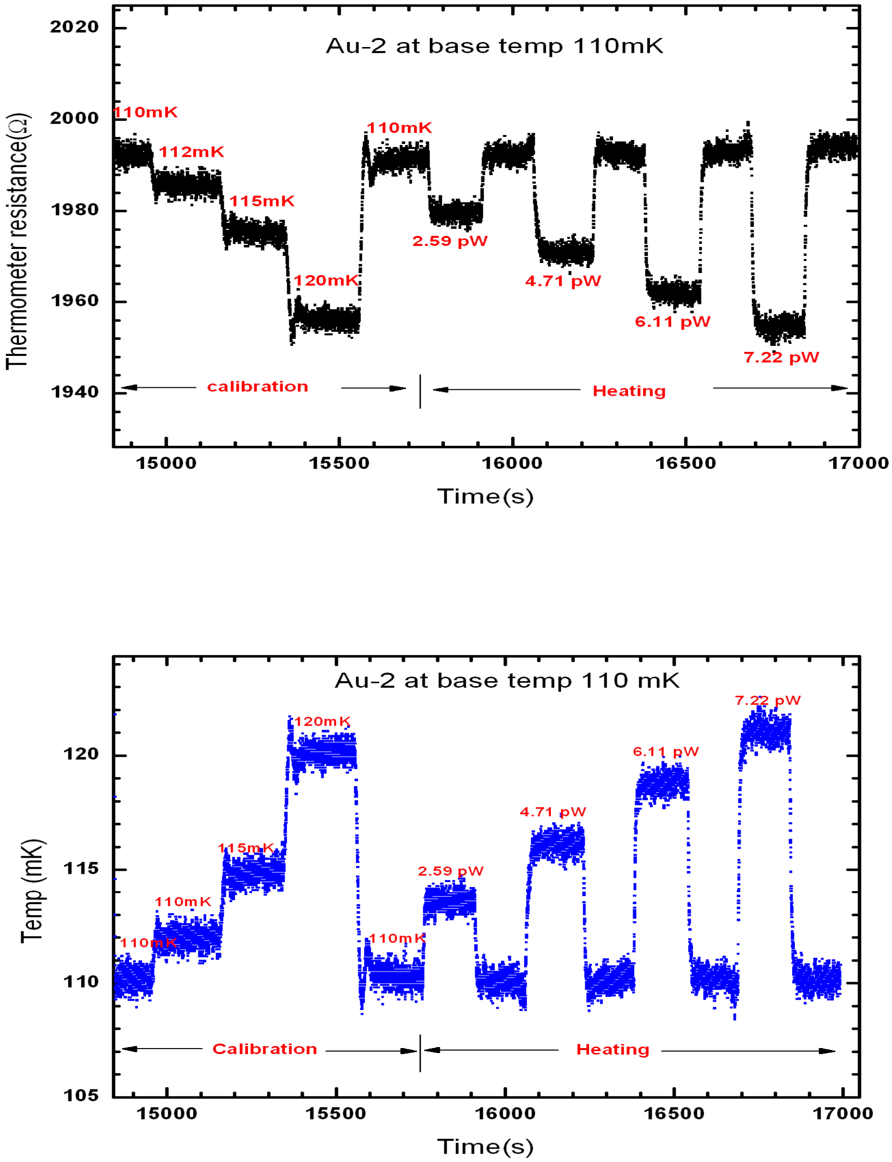

(FIG.6.3) Sample thermometer resistance vs time (top) and temperature vs time (bottom) for sample Au-2 at a base temeprature of 110 mK.

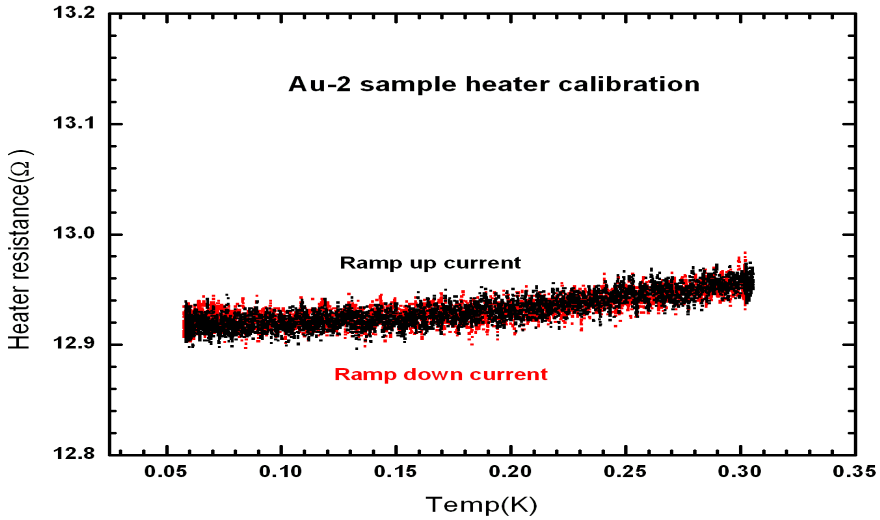

(FIG.6.4) *Resistance of the sample heater in the temperature range 60-300mK*

Thermal conductance of the heat link (in this case the bonding wires) was determined by two different ways as described in section 5.3 and the measured values are shown in Table 6.2.

(Table 6.2) *The measured thermal conductance of the heat link at different temperatures*

Temp (mK)	G_0 (WK^{-4})	$G_1 = G_0 T^{\beta}$ (WK^{-1})	$G_2 = {dP}/{dT}$ (WK^{-1})	G (Average) (WK^{-1})
70	2.27×10^{-6}	1.15×10^{-9}	1.32×10^{-9}	$(1.32\pm 0.01)\times10^{-9}$
80	2.29×10^{-6}	1.17×10^{-9}	1.33×10^{-9}	$(1.25\pm 0.01)\times10^{-9}$
90	2.28×10^{-6}	1.66×10^{-9}	1.89×10^{-9}	$(1.77\pm 0.12)\times10^{-9}$
100	2.17×10^{-6}	2.14×10^{-9}	2.37×10^{-9}	$(2.26\pm 0.12)\times10^{-9}$
110	2.12×10^{-6}	2.81×10^{-9}	3.04×10^{-9}	$(2.93\pm 0.13)\times10^{-9}$
120	2.04×10^{-6}	3.54×10^{-9}	3.78×10^{-9}	$(3.66\pm 0.12)\times10^{-9}$
150	2.36×10^{-6}	8.08×10^{-9}	8.62×10^{-9}	$(8.33\pm 0.30)\times10^{-9}$
200	2.85×10^{-6}	2.28×10^{-8}	2.37×10^{-8}	$(2.33\pm 0.45)\times10^{-8}$

By removing the silicon stem used in previous experiment (see Chapter 5), the thermal conductance was reduced by factor of 100, which allowed us to obtain reasonable time constant. The measured thermal conductance of the link as a function of temperature is shown in Figure 6.5. From the plot it is clearly seen that measured results using two different methods closely agree with each other. Figure 6.6 shows the average value of the measured thermal conductance as a function of temperature. The red curve in the figure is the power law, $G = G_0T^\beta$, fit for $\beta = 3$. Figure (6.7) shows power, dissipated on the sample-I (pure gold sample) at base temperature 100mK, as a function of delta T. The measured thermal conductance (at 100mK) obtained from the plot is 2.27×10^{-9} WK^{-1}, which is consistent with the tabulated value (see table 6.2).

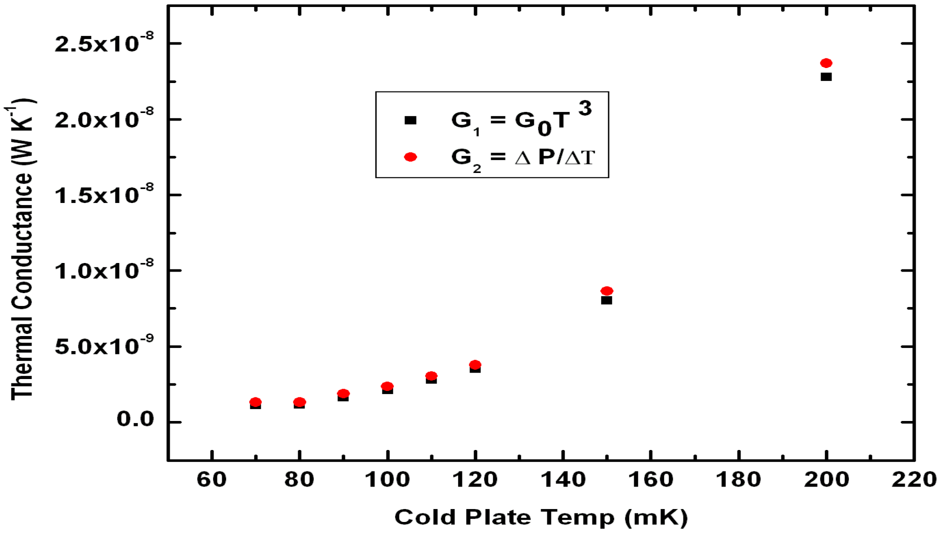

(FIG.6.5) *Measured thermal conductance of the link (using two different methods) plotted as a function of temperature.*

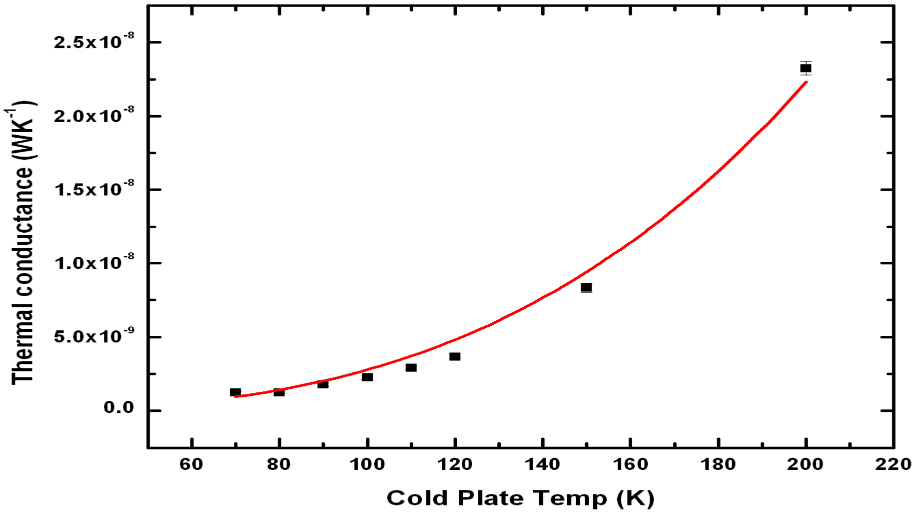

(FIG 6.6) *Power law fit of the measured thermal conductance for the sample-I at base temperature 100mK.*

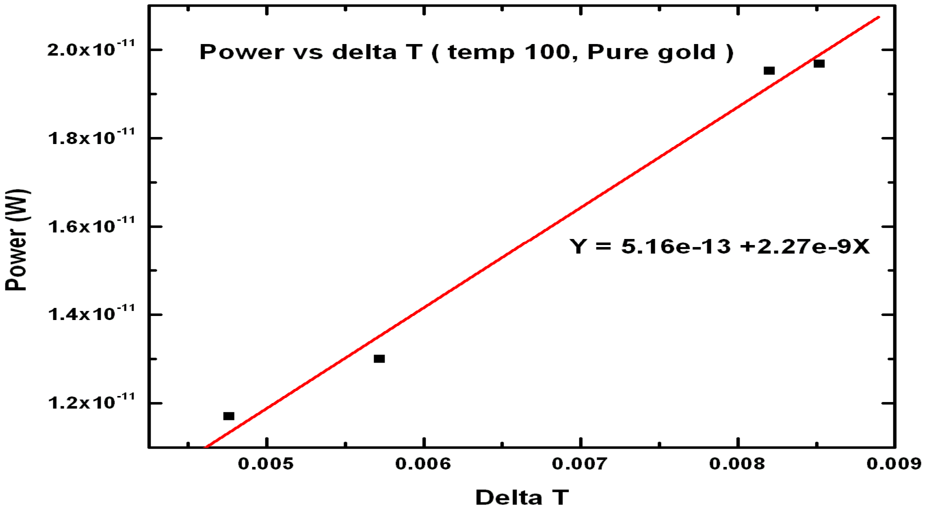

(FIG.6.7) *Power vs delta T plot for sample-I (base temperature 100mK) to determine thermal conductance*

6.4 Measurement of the Heat Capacity

For the heat capacity measurement, we used the time constant τ necessary for the bolometer to return to the base temperature once the heater has been turned off and the sample's heat capacity is (Eq. 2.3).

$$C = G \times \tau. \tag{6.1}$$

Figure (6.8) shows the typical exponential fit of a sample cooling used to determine the time constant. The measurements were repeated for different base temperatures from 70 mK to 300 mK. Figure 6.9 shows the plot of the time constant as a function of the cold plate temperature. The blue curve shows the inverse square law fit of the plot. For each base temperature, the heat capacity of each sample we calculated combining the data from all heater powers.

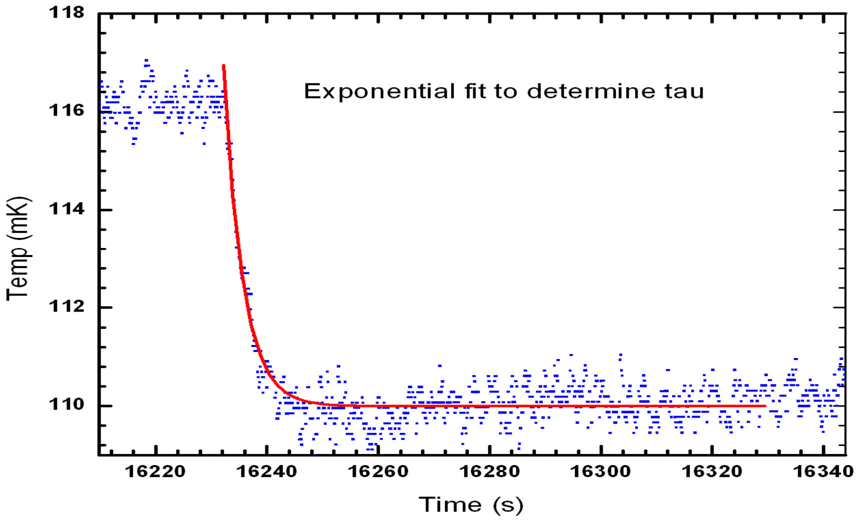

(FIG.6.8) *Exponential fit of the relaxation plot to determine* τ*.*

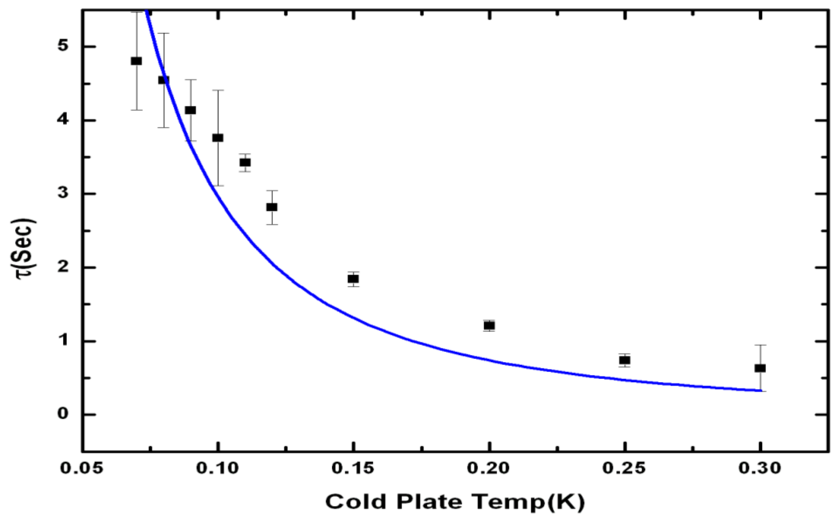

(FIG.6.9) *Time constant τ as a function of temperature T (for sample Au-2)*

6.5. Results

The heat capacities of all ten samples, plus sample-0 were determined in the temperature range 70 to 300 mK. Figure (6.10) shows the values of heat capacity for each sample (color data points) as a function of temperature before the contribution of substrate, heater, and thermometer (sample-0 – black squares) were subtracted. As it is immediately evident from the figure, the heat capacity of substrate, thermometer, and heater, starts dominating the total value of heat capacity at temperatures of 200 mK and higher. We therefore decided to limit our further analysis below 150 mK. That is, in any event, the critical range of temperatures for a microcalorimeter for a holmium neutrino mass experiment.

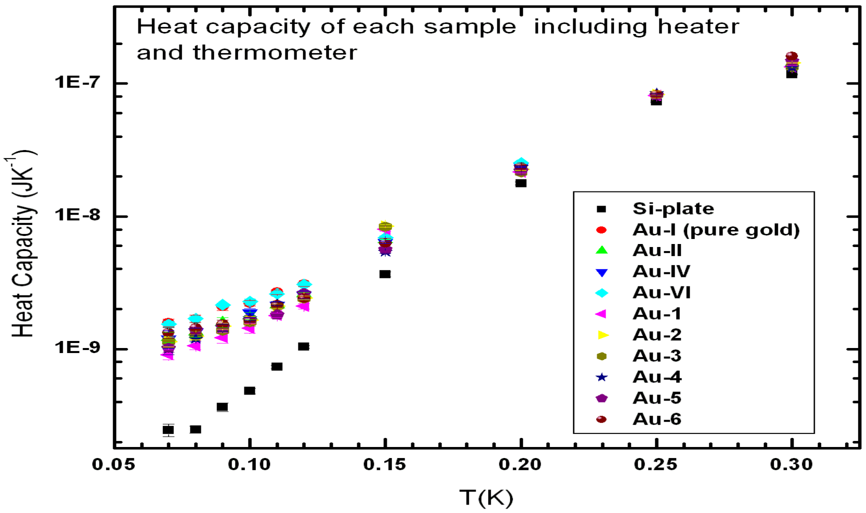

(FIG.6.10) *Measured heat capacities of all samples are plotted as a function of temperature. The combined heat capacity of substrate, heater, and thermometer (black squares) starts dominating above 200 mK.*

After the contributions from heater, thermometer, and substrate were subtracted from the measured heat capacities of each sample, the measured mass of the gold films was used to determine the specific heat capacity of each sample. The results are shown in Figure (6.11). We also used a polynomial function with only linear and cubic term ($c = \gamma T + \alpha T^3$) to fit individual data sets. The fitting curves are shown in Figure (6.12) and the values of γ, α, and specific heat at 0.1K for each sample are reported in Table 6.3.

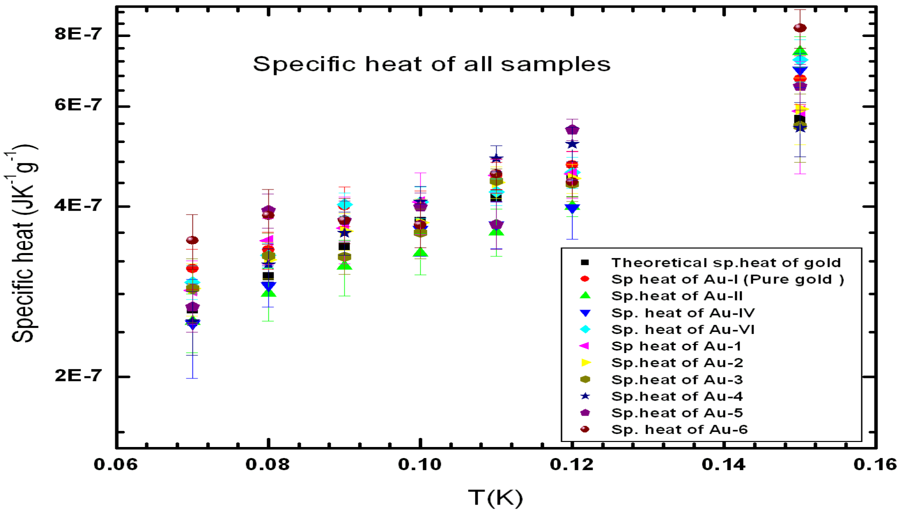

(FIG.6.11) *Measured specific heat capacities of all samples in the temperature range 70 to 150 mK.*

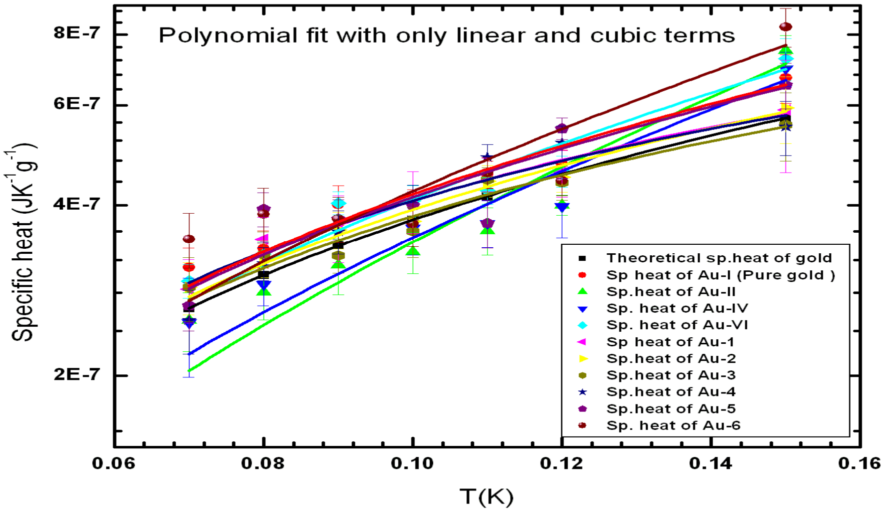

(FIG.6.12) *Polynomial fits using only linear and cubical terms.*

(Table 6.3) *The values of fitting parameters obtained from polynomial fit of individual data sets. Specific heat of each sample at 0.1K was calculated using the fitting parameters.*

Samples	γ	α	Sp. heat at 0.1K
Au-1	$(42.24\pm1.32)\times10^{-7}$	$(-20.00\pm8.71)\times10^{-6}$	$(40.24\pm1.58)\times10^{-8}$
Au-2	$(39.51\pm1.38)\times10^{-7}$	$(-22.82\pm9.05)\times10^{-6}$	$(39.93\pm1.65)\times10^{-8}$
Au-3	$(39.50\pm1.93)\times10^{-7}$	$(-10.00\pm10.00)\times10^{-6}$	$(38.50\pm2.17)\times10^{-8}$
Au-4	$(42.59\pm3.06)\times10^{-7}$	$(-20.00\pm20.00)\times10^{-6}$	$(40.59\pm3.66)\times10^{-8}$
Au-5	$(40.00\pm4.77)\times10^{-7}$	$(10.00\pm30.00)\times10^{-6}$	$(41.00\pm5.64)\times10^{-8}$
Au-6	$(35.31\pm6.66)\times10^{-7}$	$(70.00\pm40.00)\times10^{-6}$	$(42.31\pm7.77)\times10^{-8}$
Au-I	$(40.51\pm2.27)\times10^{-7}$	$(10.00\pm10.00)\times10^{-6}$	$(41.51\pm2.48)\times10^{-8}$
Au-II	$(24.09\pm4.36)\times10^{-7}$	$(100.00\pm30.00)\times10^{-6}$	$(34.09\pm5.29)\times10^{-8}$
Au-III	$(27.59\pm4.32)\times10^{-7}$	$(70.00\pm30.00)\times10^{-6}$	$(34.59\pm5.26)\times10^{-8}$
Au-IV	$(36.69\pm3.49)\times10^{-7}$	$(40.00\pm20.00)\times10^{-6}$	$(40.69\pm4.02)\times10^{-8}$

While Figure 6.11 is comprehensive, it is rather difficult to properly understand the details and directly compare the samples. For an easier comparison of the samples we used the results of the polynomial fits to extract the specific heat capacities of all samples at 100 mK (see Table 6.3). The result is shown in Figure 6.13. In the figure, the extracted value at 100 mK for each sample is plotted together with the literature value for pure gold from the Handbook of Chemistry and Physics [100]. On average, the measured values are about 5% higher than the literature one, probably due to the characteristics of the gold used. However, all data are consistent with the literature value and with the sample without implant (sample Au-I). More in general, within the implant concentration probed, we do not see any effect of the implanted holmium and erbium on the heat capacity of gold. This make the direct implant of ^{163}Ho in a gold absorber a promising procedure to fully embed the radioactive material in a microcalorimeter absorber for the measurement of the neutrino mass.

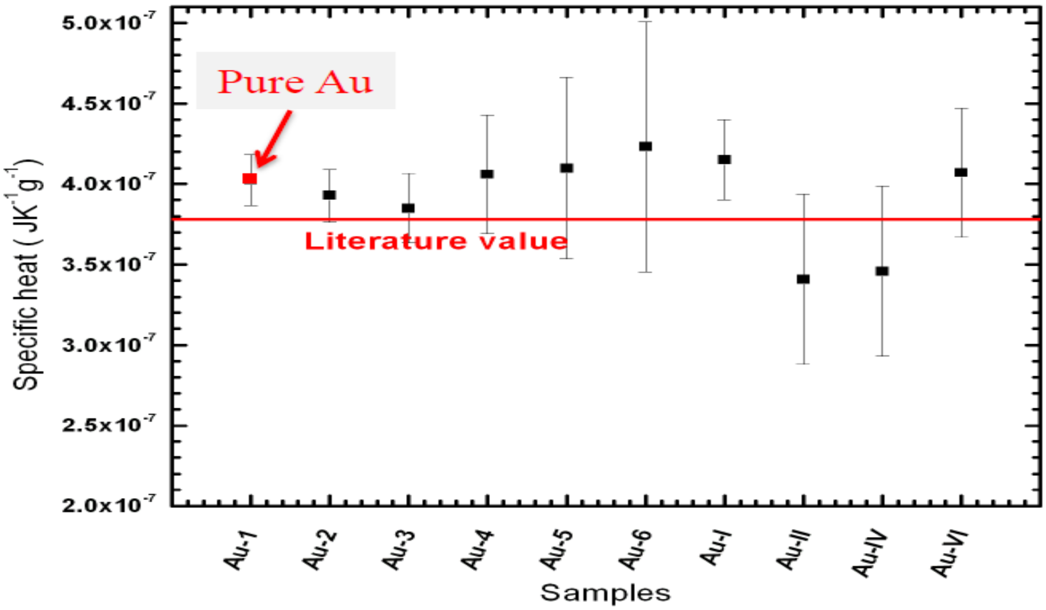

(FIG.6.13) *Specific heat capacity of individual samples at 100mK (extracted from polynomial fitting parameters). The red line represents the specific heat capacity of pure gold from the literature.*

6.6 Investigation of Crystal Structure and Crystal Size Using X-ray Analysis

We did not expect visible effects of implantation on the polycrystalline gold films, but we wanted to verify it experimentally. We used the Philips X'pert X-Ray Diffractometer to analyze the crystal structure of the thin films. The working principle and some important aspects of the X-ray Diffractometer are presented in section (4.5).

The crystal peaks all 10 gold film sample were determined by using $2\theta-\omega$ and ω-scans. Figure 6.14 shows the XRD pattern of sample Au-I (pure gold), while Figure 6.15 shows the XRD patterns of all ten samples. Both the implanted and non-implanted samples show similar patterns. For each sample, nine distinct peaks were identified between the diffraction angle 20^0 to 140^0.We noticed few Ir peaks in the second batch samples, particularly samples Au-1, Au-2, Au-3, Au-4, Au-5 and Au-6, which were absent in the first batch samples. This must be due to a thicker Ir layers or a thinner Au layers in the second batch samples.

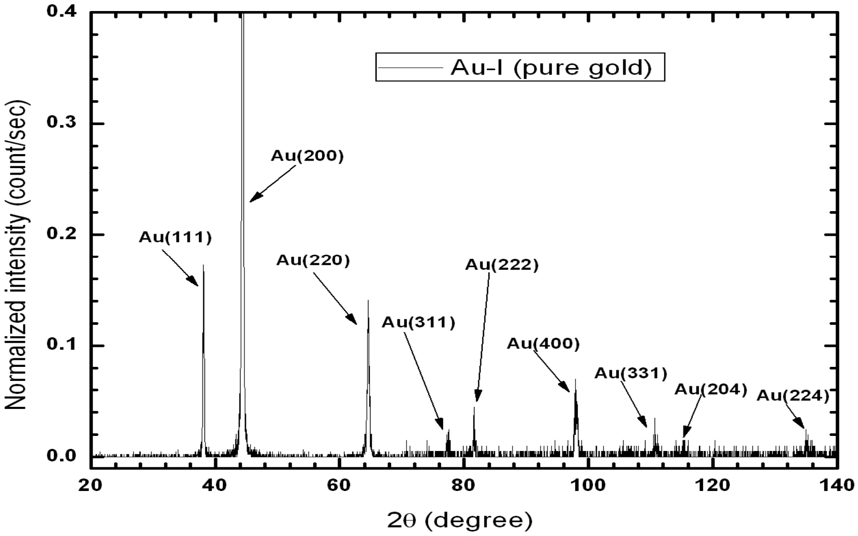

(FIG.6.14) *X-ray diffraction patterns for the pure gold film sample Au-I are shown. The normalized intensity was plotted as a function of 2θ, and nine distinct gold peaks were found in the 20 to 140 degree range.*

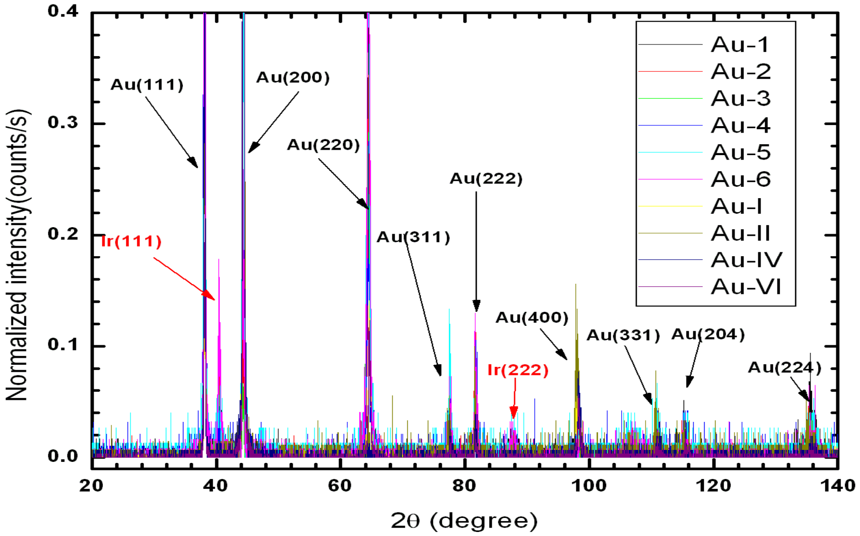

(FIG.6.15) *X-ray diffraction patterns for all 10 gold film samples plotted as function of 2θ.Nine distinct peaks were found for each sample. Few Ir peaks were identified for 2nd batch samples.*

The broad half-width diffraction peaks indicated that the films are quite amorphous with very small grains. The width of the diffraction peaks were used to estimate the crystal size of each sample. Particularly, we used Scherrer formula [101]:

$$t = \frac{0.9\lambda}{B\, cos\theta} \qquad 6.2$$

where t is average crystal size, λ is the wavelength of the x-ray, 2θ is the XRD peak position and B is the peak FWHM. The width B is measured, in radians, at the intensity equal to half the maximum intensity and is also called half width of Gaussian distribution. We determined B and θ for each peak by fitting the Gaussian equation given by

$$y = y_0 + \frac{A}{w\sqrt{\pi/2}} e^{-2\frac{(X-X_C)^2}{w^2}} \qquad 6.3$$

where 2.35×w is the half width and X_C is the XRD peak position. The crystal sizes of all the samples determined from the width of different peaks are shown in Figure 6.16. We found that the crystal size lies between 80 to 180Å. There is no dependence of the crystal size on the concentration of the implanted ions.

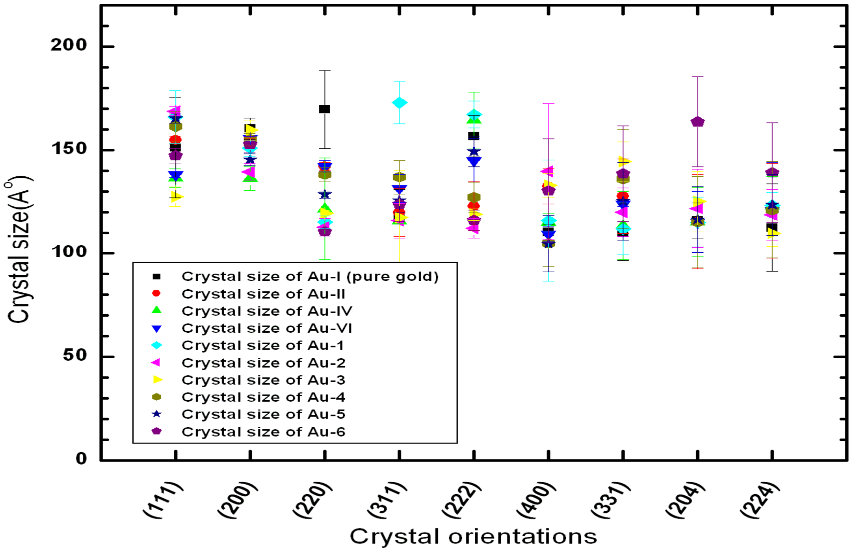

(FIG.6.16) *Crystal size of all samples obtained from the width of the nine distinct peaks.*

Chapter 7

Conclusions

My Ph.D. dissertation research has been focused on the research and development for a holmium experiment. The experiment goal is the calorimetric measurement of the electron neutrino mass with a source (^{163}Ho) embedded absorber. Knowing the thermal properties at the working temperature of the microcalorimeter components is critical for choosing the absorber material and for optimizing detector performance. From the experimental point of view, I have focused primarily on the investigation of the thermal properties of the potential absorber in the working temperature region of microcalorimeters. As a part of this thesis work, we have investigated the thermal properties of an Yttrium silicide sample and Ho^+ or Er^+ implanted gold films as potential candidates of source imbedded absorbers for a holmium experiment. We used a bolometric technique to measure the heat capacity of each samples.

The starting point was designing a bolometer with a properly chosen heater and thermometer so that the bolometer is sensitive enough to measure the heat capacity of a sample. Heat capacity of a 2 gram Y_5Si_3 sample in the temperature range 90-300mK was measured by using bolometers equipped with bare Ruthenium oxide thermometers and thick film chip resistor heaters (details in Chapter 5). We also measured the electrical resistivity and electrical conductivity of the sample in the temperature range 0.09 to 300K. We found that the specific heat capacity of the sample is well behaved and predictable in the temperature range of interest. However, the measured specific heat capacity of the Y_5Si_3 sample is greater than that of pure gold and too high to be used as absorber material in a microcalorimeter with high performance. The measured specific heat capacity and heat capacity per unit volume of Yttrium Silicide are linear with $\gamma = (6.79 \pm 0.15) \times 10^{-5} \mathrm{Jg^{-1}K^{-2}}$ and $\gamma = (2.96 \pm 0.07) \times 10^{-5} \mathrm{Jcm^{-3}K^{-2}}$ respectively. The electrical resistivity and the electrical conductivity of the sample are constant in the temperature range of interest.

In order to measure the heat capacity of gold films at the working temperature of microcalorimeters, we required a much more sensitive (order of 10^{-10} $\mathrm{jK^{-1}}$) bolometer. We first verified that a bolometer with a silicon plate, bare Ge NTD thermometer, and thin film heater was sensitive enough to measure the heat capacity of a gold film in the temperature range of interest. We then used a bolometric technique to measure the heat capacity of gold films, implanted with various concentrations of holmium and erbium (a byproduct of the ^{163}Ho fabrication), in the temperature range 70 mK to 300 mK. We found that at the working temperature range of microcalorimeters, the measured specific heat of a gold film agrees with the theoretical value and is independent of the implanted ions concentration. We also analyzed our gold film samples using the X-ray Diffraction (XRD) technique. The XRD analysis shows that the crystal structure and crystal size of a gold film remains unchanged after the implantation of ions, which is not surprising for amorphous gold films. Based on our results we concluded that the specific heat capacity of the gold films is not affected by the implant, making this a viable option for a future microcalorimeter holmium experiment.

Microcalorimeters with regular gold film absorber and energy resolution better than 2eV already exist. The next natural step is to replace the regular gold film absorber with the

^{163}Ho implanted absorber in such microcalorimeters. This modified microcalorimeter with a source imbedded absorber can be used to carry out a small size, short-time scale pilot experiment for testing the potential of a Holmium experiment.

Appendix A

Magnesium as a light-weight alternative to copper for manufacturing refrigerators

A.1 Overview

Microcalorimeters or bolometers, working around 100mK, require low temperature cooling system, namely, Adiabatic Demagnetization Refrigerators with liquid cryogen. Copper has been widely used for making the cold plates and other parts of the cryogenic refrigerators because it remains excellent conductor without being superconducting even at very low temperature (below 100mK). However, the heavy cold stage copper components are not good choices for space based experiments, where mass of the detector always becomes an issue. Therefore, the lightweight alternative to the copper components, which reduce vibrational heat input and maximize mechanical resonant frequency, are highly desirable for space applications.

The density of magnesium (1.74 gcm^{-3}) is more than five times lower than that of copper (8.94 gcm^{-3}). However, experimental values of thermal conductivity and heat capacity of magnesium had not been previously determined over the working temperature range, 50mK-150mK, of most of the TES detectors. We have measured the thermal properties (conductivity, heat capacity, and diffusivity) of high purity magnesium as well as commercial grade, and then compared our results with that of typical Oxygen Free High Conductivity (OFHC) copper.

We found that the characteristics of high purity (99.95%) magnesium are comparable to that of OFHC copper, but with a factor of 5 smaller weights. The results were already published in 2010 (see reference [99]). Here we summarize our results and show some applications where Cu has already been replaced with Mg in the cold end of refrigerators.

A.2 Experimental Setup

Three samples of identical shape, but different materials were measured.

- <u>Sample#1:</u> 99.95% high purity Mg from Sigma-Aldrich (Mn 0.01%, Fe < 0.005%, Cu < 0.001%, Ni < 0.001%) [104].
- <u>Sample#2:</u> 95% pure Mg structural alloy
- <u>Sample#3:</u> Commercial grade of oxygen free high conductivity (OFHC) copper (used as reference)

All three samples were in the form of long stems with 66 mm length, 6.8 mm width and 3.5 mm height.

A.3 Thermal Conductivity Measurements

The measurement procedure is (in principle) similar to one described in Chapter 5 and Chapter 6. To measure the thermal conductivity we constructed a bolometer using each sample. One end of each sample was connected to the ADR Cold Plate, while the other end was equipped with a heater (10 kΩ resistor at room temperature) and a ruthenium oxide thermometer (RX-102A-BR) as discussed in Chapter 5. Each of the sample thermometers was first locally calibrated using a germanium resistance thermometer (GRT) installed on the cold plate of the ADR .The calibrated thermometers were then used to measure the temperature of the hot ends. Small power was dissipated on the heater keeping the temperature of the cold plate constant. The measurements were repeated for constant current (about 1 μA), but three slightly different applied voltages across the heater. Each of these voltages was chosen in such a way that the power dissipated on the resistor was able to produce temperature difference of a few milliKelvins across the two ends.

We calculated the thermal conductance G using two different approximations as described in Chapter 5 and Chapter 6. We also verified that the results from both methods are equivalent within the experimental uncertainty. The measured dimensions of each sample were used to determine thermal conductivity. Figure (A.1) shows the measured thermal conductivity for the all three samples. The blue line, which is taken as a reference, represents the typical conductivity curve for OFHC with residual resistivity ratio (RRR) of 30 (note: variations of more than an order of magnitude may occur depending on the sample) [105]. From the figure, it is clear that the commercial magnesium alloy has a very poor thermal conductivity and therefore, useless for the low temperature applications. We therefore decided to consider only the high purity Mg (sample #1) for the further (heat capacity, diffusivity, and electrical resistivity) measurements.

High purity magnesium has conductivity comparable to that of OFHC. A fit with linear dependence of conductivity on temperature, $\kappa = \kappa_0 T$, gives:

$$\kappa_0 = (17.7 \pm 0.6)\mathrm{Wm^{-1}K^{-2}} \qquad \mathrm{A.1}$$

which gives a conductivity at 100 mK as

$$\kappa(0.1K) = (1.77 \pm 0.06)\mathrm{Wm^{-1}K^{-2}} \qquad \mathrm{A.2}$$

The measured electrical resistivity of the high purity magnesium at room temperature is $3.9\mu\Omega$ cm, while the resistivity at 4.2 K is $0.12\mu\Omega\mathrm{cm}$ giving an RRR of 32.5. Using

Wiedemann-Franz law with a Lorenz number $L = 2.44 \times 10^{-8} W\Omega K^{-2}$, this corresponds to $\kappa_0 = 20\mathrm{Wm}^{-1}\mathrm{K}^{-2}$, which is in good agreement with our measured value.

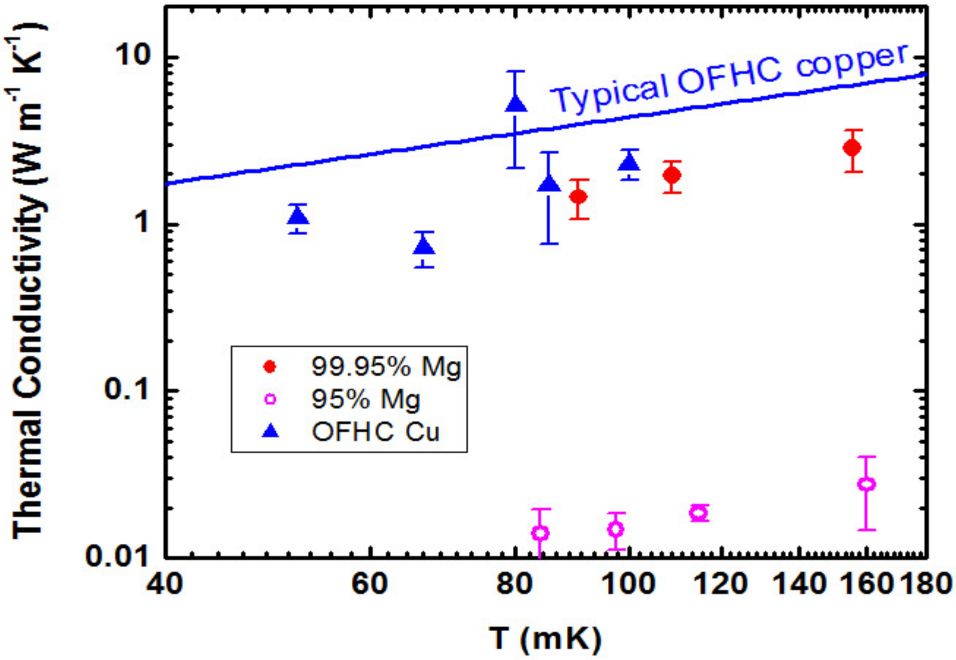

(FIG.A.1) *The measured thermal conductivities of three samples are plotted as a function of Temperature. The blue line represents the conductivity curve for typical commercial product of OFHC cu with RRR = 30 [105].*

A.4 Heat Capacity Measurements

For capacity of high purity Mg (sample #1), two bolometers were constructed using two identical Al posts. The dimension of each post was 60mm length, 2 mm width, and 2 mm thick. One end of the post was fixed on the cold plate of the ADR, while a heater and thermometer were placed on a small platform of the other end. The thermal conductance of the post was measured using the procedure described in previous section (and previous two chapters). The relaxation of the sample thermometer, after the heater was turned off, followed the exponential decay curve. The time constant τ was determined by exponential fitting. The combined heat capacitance of the post with heater and thermometer was determined by using following simple relation as described in previous chapters.

$$C = \tau \times G \qquad A.3$$

The measurements of heat capacitance were repeated at different base temperatures in the range 60 to 160mK. Similar measurements were repeated with a block of high purity Mg sample of volume 0.934cm^3 mounted on the platform. The heat capacitance of the high purity Mg sample was determined by subtracting contribution of heater, thermometer, and the Al post. Measured volume of the sample was used to determine the heat capacity per unit volume. Figure 2 shows the measured thermal heat capacity of high purity Mg (sample #1). The blue line in the figure represents a plot of the electronic heat capacity from the measurements of at higher temperature in the literature [92], where $C = \gamma T$, $\gamma = 1.31 mJmole^{-1}K^{-2}$. In the temperature range of interest, the lattice contribution is negligible. A linear fit to our data (assuming a linear dependence on temperature) gives:

$$\gamma = (1.5 \pm 0.2) mJmole^{-1}K^{-2}, \qquad A.4$$

which yields the heat capacitance at 100 mK of:

$$c(0.1K) = (0.15 \pm 0.02) mJmole^{-1}K^{-2}\ . \qquad A.5$$

We also notice that the copper has a smaller γ, however its higher molecular density results in almost equal heat capacity per unit volume at low temperature. As the temperature approaches to the room temperature, volumetric heat capacity of magnesium is a factor of 2 smaller than copper, which makes cooldowns faster.

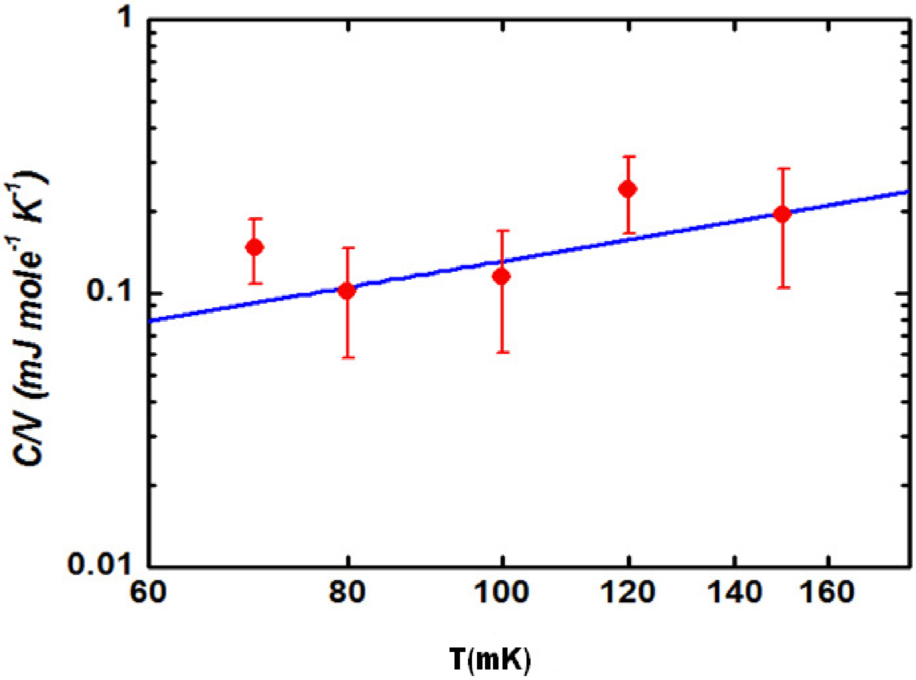

(FIG.A.2)*The measured Heat capacity per unit volume of high-purity magnesium plotted as a function of temperature. The blue line is not a fit, but a plot of the electronic heat capacity* $c = \gamma T$ *where* $\gamma = 1.31 mJmole^{-1}K^{-2}$ *obtained from measurement at higher temperature in the literature [92].*

A.5 Diffusivity

The diffusivity (α) of high purity Magnesium was calculated using the measured value of conductivity and heat capacity.

$$\alpha = \frac{\kappa}{\rho \, c_p} \qquad A.6$$

where ρ is the density and c_p is the specific heat capacity at constant pressure.

Combining the results of thermal conductivity and heat capacity we obtained a value for the diffusivity in the 60-150mK range of

$$\alpha = (0.16 \pm 0.02) m^2 s^{-1} \qquad A.7$$

A.6 Applications

In conclusion**, t**he thermal properties of high purity magnesium are well-behaved and predictable in the temp range 60-150 mK, and are comparable to those OFHC copper. Our results established magnesium as a promising alternative to copper for making components of refrigerator for space. Based on our results, two leading space based (sounding rockets) experiments, “x-ray quantum calorimeter (XQC) experiment [102] and the Micro-X experiment” [103], have already replaced their copper based cold end components with magnesium one. The original OFHC copper cold plate of the XQC experiment has been replaced with a magnesium one (recent photo is shown in Figure A.3), and the cold end of the Micro-X experiment has been directly designed and built using magnesium (recent photo is shown in Figure A.4). In the XQC experiment, the original total weight of the cold stage was 240 grams. Simply replacing the copper cold plate and outer cover with magnesium ones saved about 68 grams, reducing the weight to 172 grams. This reduced the heat input from launch vibration, and improved the microphonic performance and the probability of surviving recovery loads. It is noteworthy mention that magnesium oxidizes readily, particularly on prolonged exposure to moisture. However, it can be readily gold plated, which provides a stable surface with good thermal conductivity at mechanical attachment points.

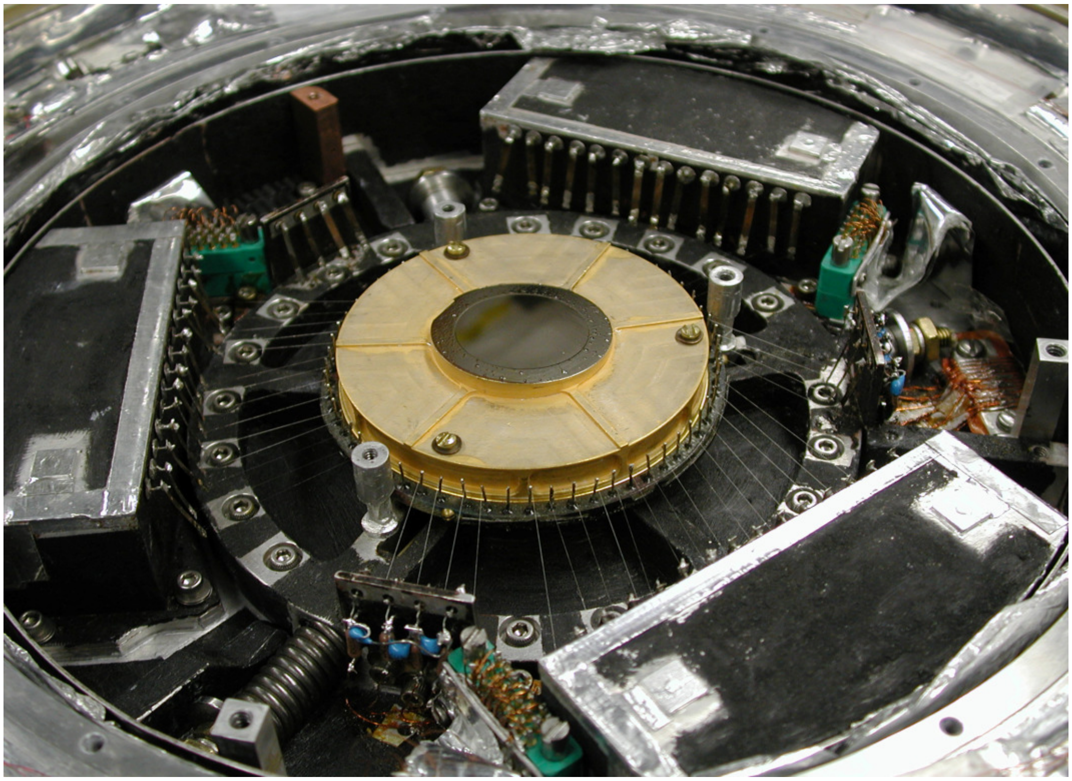

(FIG.A.3) *The original OFCH copper cold plate of XQC experiment was replaced by high purity Mg (Recent photo).*

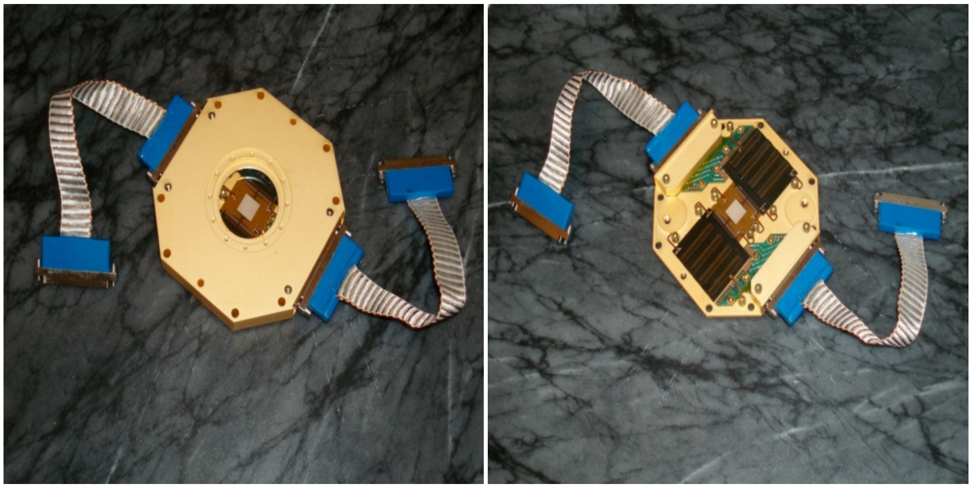

(FIG.A.4) *The cold end of Micro-X experiment was replaced by Mg (Recent Photo).*

References

1. E. Fermi, *Zeitschrift fur Physik A Hadrons and Nuclei* **88**, 161 (1935).
2. C.L. Cowan, F. Reines et al., *Science* **124**, 103 (1956).
3. F. Reines and C.L. Cowan, *Nature* **178**, 446 (1956).
4. L.M. Lederman, M. Schwartz et al., *Phys. Rev. Let.* **9,** 36 (1962).
5. K. Kodama et al., *Phys. Lett. B* **504**, 218 (2001).
6. LSND collaboration, *Phys. Rev. Lett*. **81,** 1774 (1998). LSND collaboration, *Phys. Rev. D* **64** 112007 (2001) (arXiv:hep-ex/0104049).
7. W. Hampel et al. (GALLEX collaboration), *Phys. Lett. B* **447**, 127 (1999).
8. J.N. Abdurashitov et al. (SAGE collaboration), *Phys. Rev* **D73**, 045805 (2006) (arXiv:nucl-ex/0512041).
9. Q.R. Ahmad et al. (SNO collaboration), *Phys. Rev*. Lett. **87**, 071301 (2001) (arXiv:nucl-ex/0106015).
10. J. Hosaka et al.(Super-Kamiokande collaboration), *Phys .Rev D* **73**, 112001 (2006) (arXiv:hep-ex/0508053).
11. Y. Gando et al. (Super-Kamiokande collaboration), Phys. Rev. Lett. **90**, 171302 (2003) (arXiv:hep-ex/0212067).
12. Q.R. Ahmad et al. (SNO collaboration), *Phys. Rev. Lett*. **89**, 071301 (2002) (arXiv:nucl-ex/0204008).
13. R. Wendell, et al.(Super-Kamiokande collaboration),airXiv:1002.3471.
14. M. Ambrosio et al. (MACRO collaboration), *Phys. Lett. B* **566**, 35 (2003) (arXiv:hep-ex/0304037).

15. K. Eguchi et al. (KamLAND Collaboration), *Phys. Rev. Lett.* **90**, 021802 (2003) (arXiv:hep-ex/0212021).
16. M. Apollonio et al. (CHOOZ collaboration), *Phys. Lett. B* **434**, 415 (1999) (arXiv:hep-ex/9907037).
17. M.H. Ahn et al. (K2K collaboration), *Phys. Rev. D* **74**, 072003 (2006) (arXiv: hep-ex/0606032).
18. P. Adamson et al. (MINOS collaboration) arXiv: 0711.0769.
19. E. Ferri, *PhD thesis* (2011) University of Milano-Bicocca.
20. B. Kayser, arXiv: 0804.1497.
21. J. Beringer et al, (Particle Data Group), *PR D* **86**, 010001(2012) (URL:http://pdg.lbl.gov).
22. J. Lesgourgues and S. Pastor, *Advances in High Energy Phys.* **2012**, 608515 (2o12) (doi:10.1155/2012/608515).
23. K.N. Abazajian et al., *Astroparticle Phys.* **35**, 4 (2011) (arXiv: 1103.5083).
24. M. Goeppert-Mayer, *Phys. Rev.* **48**, (1935).
25. S.R. Elliott et al., *Phys. Rev. Lett.* **59**, 512 (1987) 20202023.
26. W. Furry, *Phys. Rev.* **56**, 1184 (1939).
27. A. Sturmia and F. Vissani, arXiv: hep-ph/0606054 (2010).
28. W. Rodejohann, arXiv: 1106.1334v3 [hep-ph] (2011).
29. F. Gatti et al., *MARE proposal* (2006).
30. R. G. H. Robertson et al., *Phys. Rev. Lett.* **67**, 957 (1991).
31. E. Holzschuh, *Phys. Lett. B* **287**, 381 (1992).
32. W. Stoeffl et al., *Phys. Rev. Lett.* **75**, 3237 (1995).

33. V. Labashev, et al., *Nucl. Phys. B Proc. Suppl.,* **91**, 273 (2001)
34. KARTIN homepage, www.katrin.kit.edu.
35. R. Bottesch, *Diploma thesis* (2012) University of Munster.
36. J. Angrik et al., *KATRIN Design Report* (2004).
37. F. Gatti, et al., *Nature* **394**, (1999).
38. C. Arnaboldi et al., *Phys. Rev. Lett.* **91**, 161802 (2003).
39. H. Greaves and T. Thomas, arXiv: 1204.4674v1 [math-ph] (2012).
40. J.C. Mather, *Appl. Opt.* **21**, 1125 (1982).
41. S. H. Moseley, J.C. Mather, and D. McCammon, J. Appl. Phys. **56**, 1257 (1984).
42. D. F Bogorin, PhD thesis (2008), University of Miami.
43. D. H. Andrews et al., *Rev. Sci. Instrum.* **13**, 281 (1942) (doi: 10.1063/1.1770037).
44. W. Seidel et al., *Phys. Lett. B* **236**, 483 (1990).
45. www.lakeshore.com/products/cryogenic-temperature sensors.
46. C. Kittel, *Introduction of solid state physics*, (eighth edition).
47. M. Galeazzi and D. McCammon, *J. Appl. Phys.* **93** 4856 (2003).
48. E. Figueroa-Feliciano, *J. Appl. Phys.* **99** 114513 (2006).
49. D. McCammon, “Thermal Equilibrium Calorimeters - An Introduction”, in Cryogenic Particle Detection, Christian Enss (ed.), Topics in Applied Physics 99, (Springer; Berlin 2005) pp 1-34
50. E. Figueroa-Feliciano, *PhD thesis* (2006) Stanford University.
51. K.D. Irwin and G.C. Hilton, “Transition Edge Sensors”, in Cryogenic Particle Detection, Christian Enss (ed.), Topics in Applied Physics 99, (Springer; Berlin 2005) pp 63-142

52. J. Appel and M. Galeazzi, *Nucl. Instr. & Meth. Phys. Res. A,* **562,** 272 (2006)
53. J. Ullom et al., *Appl. Phys. Lett*. **84,** 4206 (2004).
54. M. Galeazzi, *Rev. Sci. Inatrum*. **69,** 2017 (1998).
55. M. Galeazzi, *IEEE TRANSACTIONS ON APPLIED SUPERCONDUCTIVITY* **21**, 267 (2011).
56. K. D. Irwin, *Nucl. Instr. & Meth. Phys. Res. A* ***559,*** 718 (2006).
57. M. Galeazzi et al., *Nucl. Instr. & Meth. Phys. Res. A* ***520,*** 344 (2004).
58. P. R. Solomon, *Phys. Rev. Lett.* **16**, 50 (1966)
59. J. R. Clem, *Phys. Rep*. **75**, 1 (1981).
60. A. De Rujula, *Nucl. Phys. B* **188**, 414 (1981).
61. C. L. Bennett et al., *Phys. Lett. B* **107***,* 19 (1981).
62. C. W. Reich and B. Singh, *Nuclear Data Sheets* **111**, 1211 (2010).
63. G. Audi and A. H. Wapstra, *Nucl. Phys. A* **595**, 409 (1995).
64. W. Bambynek et al., *Rev. Mod. Phys*. **49**, 77 (1977).
65. A. De Rujula and M. Lusignoli, *Phys. Lett. B* **118**, 429 (1982).
66. M.Galeazzi et al., *arXiv: 1202.4763v2 [physics.ins-det]* (2012).
67. M. Lusignoli and M. Vignati, *Phys. Lett. B* **697**, 11 (2011).
68. F. Gatti et al., *Phys. Lett. B* **398**, 415 (1997).
69. H. L. Ravn et al., *In La Plagne 1984, Proceedings, Massive Neutrino In Astrophysics and In Particle Physics*, 287-294.
70. F. X. Hartmann and R. A. Naumann, *Nucl. Instrum. Meth. A* **313**, 237 (1992).
71. J. D. Armstrong, *PhD thesis*, (2012) the University of Miami.
72. T. Saab et al., *J. Appl. Phys.***102**, 104502 (2007*);* doi: 10.1063/1.2811882.

73. E. Figueroa-Filiciano et al., *J. Appl. Phys.***151**, 424 (2008*);* doi: 10.1063/1.2811882.
74. A. D. Brown., *J. Low Temp. Phys.* **151**, 413 (2008); doi: 10.1007/s10909-007-9667-4.
75. K. Riisagar, *J. Phys. G* **14**, 1301(1988).
76. P.T. Springer, et al., *Phys. Rev. A* **31**, 1965 (1985).
77. A. Nucciotti., *Astropart. Phys.* 34, 80 (2010).
78. Cl. Chen, *PhD thesis* (2006) the University of Miami.
79. G. Batey and V. Mikheev, *J. Low Temp. Phys.* **113**, 933 (19988).
80. P. Debye, *Ann. Phys*.**81**, 1154 (1926).
81. W. F. Giauque, *J. Am. Chem. Soc*. **49**, 1864 (1927).
82. W. F. Giauque and D. P. Mac Dougall, *Phys. Rev.* **43**, 768 (1933).
83. W.J. De Haas et al., Physica **1,** 1 (1933).
84. C. Hagmann et al., Cryogenics **34**, 213 (1994).
85. D. V. Schroeder, *An Introduction to Thermal Physics*, Chapter 6, 221-256 (2000).
86. J.D. Armstrong et al., J Low Temp Phys 167, 664 (2012).
87. J.N Burney, *PhD thesis* (2006), Stanford University.
88. D. McCammon et.al, *Astrophysical J.* **576**, 188 (2002).
89. L. Gastaldo, A. Fleischmann, C. Enss Editors, "Low Temperature Detectors (LTD-14)", J. Low Temp. Phys. 167 (2012).
90. D. Denlinger et. al. "Thin film microcalorimeter for heat capacity measurements from 1.5 to 800K." *Rev. Sci. Instr. 64(4)*, 1994: 946.

91. M. Riberio Gomes et al., *IEEE Transactions on Applied Superconductivity* **23,** 3 (2013).
92. Handbook of Chemistry and Physics, 60th Edition, Edited by R.C. Weast (CRC, Boca Raton, Fl, USA) 1979.
93. F. Canepa et.al., *J. Magn. Magn. Mater.* **118** , 182-186 (1993).
94. M. Galeazzi et al., Phys. Rev. C63 (2001) 014302.
95. F. Gatti et al., *Nucl. Phys*. **B91**, 293 (2001).
96. P. C.-O. Ranitzsch et al. *J. Low Temp. Phys*., Online First (2012).
97. A. Nucciotti, arXiv:1012.2290 (2010).
98. B. L. Rhodes et al., *Phys. Rev* **109,** 5 (1958).
99. M. Galeazzi et al., *Rev. of Sci. Ins*.**81**, 076105-1 to 076105-3 (2010).
100. K.P. Neupane, *PhD thesis (2009)*, University of Miami.
101. B.D. Cullity, *Elements of X-ray Diffraction (2nd Edition),* Chapter 3, p-102.
102. D. McCammon et al., *Astrophys. J.* **576**, 188 (2002).
103. P.Wikus et al., *AIP Conf. Proc.***1185,** 434 (2009).
104. Sigma-Aldrich, 3050 Spruce St., St. Louis, MO 63103, USA.
105. L. Risegari et al., *Cryogenics* **44**, 875 (2004).
106. A.P. Murani, *J. Phys. C: Metal Phys. Suppl*., No. 2 (1970).
107. B. Bleaney, *Proc. R. Soc. Lond.* A**, 424**, 299-306 (1989).